FEDERAL UNIVERSITY OF SÃO CARLOS
EXACT SCIENCE AND TECHNOLOGY CENTER
GRADUATE PROGRAM IN MATERIALS SCIENCE AND ENGINEERING

FRICTION RIVETING OF TI-6AL-4V AND PULTRUDED GLASS FIBER REINFORCED THERMOSET POLYESTER HYBRID JOINTS

Natascha Zocoller Borba

São Carlos
2015

FEDERAL UNIVERSITY OF SÃO CARLOS
EXACT SCIENCE AND TECHNOLOGY CENTER
GRADUATE PROGRAM IN MATERIALS SCIENCE AND ENGINEERING

FRICTION RIVETING OF TI-6AL-4V AND PULTRUDED GLASS FIBER REINFORCED THERMOSET POLYESTER HYBRID JOINTS

Natascha Zocoller Borba

Thesis presented to Postgraduate Program in Materials Science and Engineering to achieve the MASTER DEGREE IN MATERIALS SCIENCE AND ENGINEERING.

Supervisor: Dr. Leonardo Bresciani Canto (DEMa/ UFSCar)
Co-supervisor: Dr. Ing.- Sergio de Traglia Amancio Filho (HZG/ Alemanha)
Funding Agency: São Paulo Research Foundation (FAPESP/ Brazil)

São Carlos
2015

Ficha catalográfica elaborada pelo DePT da Biblioteca Comunitária UFSCar
Processamento Técnico
com os dados fornecidos pelo(a) autor(a)

Borba, Natascha Zocoller
B726f Friction riveting of TI-6AL-4V and pultruded glass fiber reinforced thermoset polyester hybrid joints / Natascha Zocoller Borba. -- São Carlos : UFSCar, 2015.
165 p.

Dissertação (Mestrado) -- Universidade Federal de São Carlos, 2015.

1. Rebitagem por fricção. 2. Compósito termofixo de P-FV. 3. Ti-6Al-4V. 4. União de estruturas híbridas. I. Título.

VITAE OF THE CANDIDATE

Bachelor’s in Materials Science and Engineering at the Federal University of São Carlos (UFSCar, 2014) with emphasis on polymeric materials.

UNIVERSIDADE FEDERAL DE SÃO CARLOS

Centro de Ciências Exatas e de Tecnologia
Programa de Pós-Graduação em Ciência e Engenharia de Materiais

Folha de Aprovação

Assinaturas dos membros da comissão examinadora que avaliou e aprovou a Defesa de Dissertação de Mestrado da candidata Natascha Zocoller Borba, realizada em 18/12/2015:

Prof. Dr. Leonardo Bresciani Canto
UFSCar

Prof. Dr. Conrado Ramos Moreira Afonso
UFSCar

Profa. Dra. Cíntia Cristiane Petry Mazzaferro
UFRGS

Certifico que a sessão de Defesa realizou-se com a participação à distância do membro Cíntia Cristiane Petry Mazzaferro e, depois das arguições e deliberações realizadas, a participante à distância está de acordo com o conteúdo do Parecer da Comissão Julgadora redigido neste Relatório de Defesa.

Prof. Dr. Leonardo Bresciani Canto – Presidente de Comissão Julgadora

ACKNOWLEDGEMENTS

The development of this MSc thesis has valuable contributions of many people who I sincerely would like to gratefully thank:

- Prof. Dr. Leonardo Bresciani Canto and Prof. Dr. Sergio T. Amancio Filho for the patient guidance, inspiration, useful critiques and trust by giving me autonomy in my research. Foremost for the commitment with the success of the Brazilian-German binational cooperation program established between HZG and UFSCar.
- Dr. Jorge F. dos Santos and Prof. Dr. Sergio T. Amancio Filho for the opportunity to perform part of my experiments in Germany and access the know-how of their groups.
- Dr. Lucian Blaga for the friendship, encouragement and support, by giving me valuable advices. Foremost for sharing with me his expertise in FricRiveting.
- All members of DEMa/UFSCar and PPG-CEM for the professional support and opportunity to conclude this MSc project in such renowned institution.
- FAPESP for sponsoring me with MSc scholarship.
- All my contemporaries from HZG, Seyed, Wiebke, Marília, Letícia, Eduardo, Erick, Nicola, Gerbson, Guilherme and Helvia, for the friendship by sharing with my challenges and special moments. Special thanks to Menno and Torben for enabling me to perform my experiments,
- My dear friends, actual and ex-housemates, Witor, Chico, Vinicius, Brunos, Jú, Natália, Fer, Debby, De, Bianca and Cí, for the daily living, personal support, for doing my days softer and happier and for sharing experiences and knowledge.
- My lovely sisters, Maika and Raissa, for walking by my side and for decoding with me the power, wish and missing of being sisters, now and ever.
- My parents, for the inspiration, unconditional support and infinite advices, and for cultivate my dreams, hope and values. All my love and gratitude always.
- My beloved and best friend André for his comprehension, support, cares and love, even one ocean far; for the good and intense moments together, in Germany and here.

ABSTRACT

Friction Riveting is an innovative spot joining technology for metal-polymer hybrid structures. This MSc thesis provided for the first time in the literature, a fundamental understanding on the Friction Riveting process for metal-thermoset composites joints. Joints of Ti-6Al-4V rivet and pultruded glass fiber reinforced thermoset polyester part were produced under three joining conditions with different heat input. Thorough analytical techniques were used to understand the physics of the process and the effect of the energy input on the final microstructure of the joined parts, the physico-chemical changes in the composite and the local and global mechanical properties of the joints. The process temperature reached values up to 761 ± 2°C indicating intrinsic degradation of the composite, formation of a softened/molten glass interlayer between the rivet and the composite and complex metallurgical transformations in the metallic rivet. Through monitoring of the process temperature and torque, an unstable friction regime was observed for FricRiveting of pultruded thermoset composites leading to distinguished extents of composite degradation. The microstructure of the Ti-6Al-4V alloy changed across the length of the rivet, from the equiaxed morphology to acicular structures in the rivet tip, where plastic deformation occurred. Three microstructural zones were proposed for each joint part including two thermo-mechanically affected zones and a heat affected zone. Microhardness mapping was performed in the metallic rivet evidencing an increase from the center to the tip of the rivet, with a hardness increment of over 20% compared to the base material ($HV_{Ti6Al4V}$= 300-320 HV). The glass interphase consolidated in the metallic surface reached values of up to 974 HV followed by a drastic decrease to 24 HV in the polyester matrix located out of the joint area. The ultimate bearing strength ranged between 60 MPa and 166 MPa. Lesser composite degraded areas led to stronger joints. Two failure modes were observed combining initial composite bearing followed by final failure through shear of the rivet with partial rivet pull-out or by full rivet pull-out. Complex failure micro-mechanisms were observed including the combination of cohesive and adhesive failures through the glass layer and the damaged composite interface. Friction-riveted joints achieved an ultimate lap shear strength of up to 80% to that of a similar bolted joint. A case study for a presumptive truss bridge application of friction-riveted joints showed a necessary of 92 rivets per truss node, 43% less than previous studies and with potential for further optimization.

REBITAGEM POR FRICÇÃO DE JUNTAS HÍBRIDAS DE TI-6AL-4V E POLIÉSTER TERMOFIXO REFORÇADO COM FIBRA DE VIDRO

RESUMO

Rebitagem por Fricção é uma tecnologia de união pontual inovadora para estruturas híbridas metal-polímero. Esta tese de mestrado apresenta pela primeira vez na literatura um entendimento aprofundado do processo de Rebitagem por Fricção para juntas de metal e compósito termofixo. Juntas de rebite de Ti-6Al-4V e componente pultrudado de poliéster termofixo reforçado com fibra de vidro foram produzidas seguindo três condições de processo com diferentes aportes térmicos. Diversas técnicas analíticas foram utilizadas para entender a física do processo e o efeito do aporte térmico na microestrutura final dos componentes unidos, mudanças físico-químicas no compósito, formação de camada vítrea intermediária entre o compósito e o rebite metálico e transformações metalúrgicas. Através do monitoramento da temperatura processual e do torque, um regime friccional não estável foi observado para a Rebitagem por Fricção de compósito pultrudado termofixo resultando em distintas extensões da degradação do compósito. A microestrutura da liga de Ti-6Al-4V transforma-se ao longo da secção transversal do rebite, de uma morfologia equiaxial no centro do rebite para uma estrutura acicular em sua extremidade, onde ocorre deformação plástica. Três zonas microestruturais foram propostas para cada componente da junta incluindo duas zonas termo mecanicamente afetadas e uma termicamente afetada. Mapa de microdureza foi realizado no rebite metálico evidenciando um aumento do centro para a extremidade do mesmo, próximo a 20% comparado com o material de base ($HV_{Ti6Al4V}$= 300-320 HV). A interfase vítrea consolidada na superfície do rebite metálico apresentou dureza em torno de 974 HV seguido de um drástico decaimento para 24 HV na matriz de poliéster localizada fora da região de união. A tensão máxima de apoio variou entre 60 e 166 MPa. Juntas com menor área degradada apresentaram os melhores desempenhos mecânicos em ensaio quase estático de cisalhamento. Dois modos de falha foram observados combinando um modo de falha inicial por deformação plástica severa no compósito seguida de falha final por cisalhamento no rebite metálico com parcial remoção do mesmo ou por remoção completa do rebite. Complexos micro mecanismos de falha foram observados incluindo a combinação de falha adesiva e coesiva através da interface entre interfase vítrea e compósito degradado. Juntas rebitadas por fricção atingiram resistência ao cisalhamento de 80% da obtida para juntas parafusadas. O estudo de caso para uma ponte hipotética treliçada revelou um número necessário de rebites de até 92 rebites por nó da ponte, 43% a menos que o encontrado em trabalhos anteriores, com potencial para futuras optimizações.

PUBLICATIONS

BORBA, N.Z., BLAGA, L.A., DOS SANTOS, J.F., CANTO, L.B., AMANCIO-FILHO, S.T. Influência da Velocidade de Rotação do Rebite na Microestructura e no Desempenho Mecânico de Juntas de Compósito Termofixo Rebitadas por Fricção. Soldagem & Inspeção (SI-2015-0085). Accepted in January 2016

BORBA, N.Z., BLAGA, L.A., DOS SANTOS, J.F., CANTO, L.B., AMACIO-FILHO, S.T. The influence of the composite features on the mechanical performance of Hybrid Thermoset composite-metal friction riveted joints. In: PPS 2015 – Polymer Processing Society, Graz, Austria, 21-25 September, 2015.

BORBA, N.Z., BLAGA, L.A., DOS SANTOS, J.F., CANTO, L.B., AMACIO-FILHO, S.T. Influência da Velocidade de Rotação do Rebite na Microestrutura e no Desempenho Mecânico de Juntas de Compósito Termofixo Rebitadas por Fricção. In: XLI CONSOLDA- Congresso Nacional de Soldagem, Salvador, Brazil, 12-15 October, 2015.

BORBA, N.Z., BLAGA, L.A., DOS SANTOS, J.F., CANTO, L.B., AMACIO-FILHO, S.T. Caracterização de compósito termofixo aplicado em junta híbrida compósito/metal rebitada por fricção. In: 13° CBPol- Congresso Nacional de Polímeros, Natal, Brazil, 18-22 October, 2015.

x

SUMMARY

LIST OF TABLES

LIST OF FIGURES

LIST OF SYMBOLS AND ABBREVIATIONS

A	Thermo-Mechanically Affected Area
ATR	Attenuated Total Refraction
AZ	Anchoring Zone
B	Height of the Anchoring Zone
bcc	Body-centered Cubic Array
BM	Base Material
BO	Burn-off
BOR	Burn-off Rate
CCT	Continuous Cooling Transformation Diagram
CF-PEEK	Carbon Fiber Reinforced Poly(ether-ether-ketone)
CHAZ	Composite Heat Affected Zone
CI	Confidence Index
CTMAZ-HD	Composite Thermo-Mechanically Affected Zone-Highly Degraded
CTMAZ-PD	Composite Thermo-Mechanically Affected Zone-Partially Degraded
d	Crystal Lattice Spacing
D	Rivet Diameter
DRX	Dynamic Recrystallization
DSC	Differential Scanning Calorimetry
DTG	Derived Thermogravimetric Curve
e	Edge Distance
E_{ax}	Axial Force Energy
EBSD	Electron Backscatter Diffraction
EBW	Electron Beam Welding
EDS	Energy Dispersive Spectroscopy
E_{fr}	Frictional Energy
E_{total}	Total Energy
F	Axial Force
FOP	Forging Pressure
FOT	Forging Time

FP	Friction Pressure
FricRiveting	Friction Riveting
FSP	Friction Stir Processing
FSW	Friction Stir Welding
FT	Friction Time
FT-IR	Fourier Transformed Infrared Spectroscopy
GF	Glass Fiber
GF-P	Glass Fiber Reinforced Thermoset Polyester
GF-PA6	Glass Fiber Reinforced Polyamide 6
GF-PEI	Glass Fiber Reinforced Poly(ether imide)
GFRP	Glass Fiber Renforced Polymer
GTAW	Gas Tungsten Arc Welding
H	Rivet Penetration Depth
hcp	Close-packed Hexagonal Array
HT	Heating Time
HV	Vickers Microhardness
HZG	Helmholtz Zentrum Geesthacht
IPF	Inverse Pole Figure
JP	Joining Pressure
JT	Joining Time
L	Plate Length
LAB	Low Angle Boundary
LBW	Laser Beam Welding
LOM	Light Optical Microscopy
LSS	Lap Shear Testing
MHAZ	Metal Heat Affected Zone
M_S	Martesite Start Temperature
MTMAZ	Metal Thermo-Mechanically Affected Zone
M_z	Frictional Torque
OFAT	One-Factor-At-A-Time Method
PC	Polycarbonate
PEI	Poly(ether imide)

PEKEKK	Poly(ether-ketone-ether-ketone)
PHAZ	Polymer Heat Affected Zone
PTMAZ	Polymer Thermo-Machanically Affected Zone
RD	Rolling Direction
RS	Rotational Speed
SAED	Selected Area Electron Diffraction
SE	Secondary Electron Mode
SEM	Scanning Electron Microscopy
SIMT	Stress Induced Martensitic Transformation
t	Plate Thickness
TD	Transversal Direction
TEM	Transmission Electron Microscopy
T_g	Glass Transition Temperature
TGA	Thermogravimetric Analysis
TIMT	Temperature Induced Martensitic Transformation
T_m	Melting Temperature
T_p	Process Temperature
ULSF	Ultimate Lap Shear Force
UTS	Ultimate Tensile Strength
VR	Volumetric Ratio
w	Plate Width
W	Rivet-Tip Width
XRD	X-Ray Diffraction
α	Alpha Phase
α’	hcp Martensite
α”	Orthorhombic Martensite
β	Beta Phase
μ_e	Coefficient of Friction
σ_{br}	Bearing Strength
υ_0	Burn-Off Rate

1 INTRODUCTION

Glass fiber reinforced thermoset polymers (GFRP) have been applied in aerospace and marine industries for over fifty years due to the possibility to design complex structures along with their low density and high specific strength. Since 1982, there have been also bridges constructed fully with GFRP, which has been accepted as alternative material for structural profiles [1-2]. A recent proposal for the use of GFRP in civil engineering infrastructure is emergency bridges. These are applied in emergency situations, such as natural disasters, wars and terrorist attacks, due to the necessity of a fast reestablishing of people flux and traffic and for humanitarian missions.

The replacement of traditional materials such as steel, concrete, wood and aluminum for GFRP in those mentioned applications introduces advantages such as high specific strength under tension and good durability [3-5]. In comparison to other polymeric composites reinforced with Kevlar or carbon fibers, the lower fabrication costs of GFRP make them more attractive for civil engineering [6]. However, joining of GFRP structural profiles is a key issue in research [7].

Conventionally, adhesive bonding and mechanical fastening, as well as their combination, have been used for this purpose. Nevertheless, the need for pre- and/or post-treatment of the parts, multiple process steps and long-time production cycles lead to high assembling costs. In the case of emergency bridges, time is a crucial factor to save lives; this is strongly related to the production and assembling time. Facing these challenges and opportunities of improvement for joining technologies in GFRP of emergency bridges, Friction Riveting (FricRiveting) appears as an alternative and effective spot joining technology. The technology was developed and patented by the Helmholtz-Zentrum Geesthacht (HZG), Germany [8-9]. FricRiveting is based on the fundamentals of mechanical fastening and friction welding. FricRiveting requires short joining cycles, only a few joining steps and provides good mechanical performance in an environmental friendly way [8] proving to be a potential technology for GFRP emergency bridge construction.

The feasibility of FricRiveting has been already successfully demonstrated for hybrid friction-riveted joints of aluminum AA2024-T3 rivets with unreinforced thermoplastics such as polycarbonate (PC) [10] and polyetherimide (PEI) [11]. More recently, FricRiveting was also successfully applied for joints of lightweight metals with fiber reinforced thermoplastic composites, such as glass fiber reinforced polyetherimide laminate (GF-PEI) [12], short carbon fiber reinforced polyether-ether-ketone (CF-PEEK) [13] and glass fiber reinforced polyamide 6 (GF-PA6) [14]. Nevertheless, limited information on hybrid joints of thermosetting composites produced by friction-based technologies is available. Recently, Huang *et al.* [15] used the combination of adhesive bonding with plastic deformation to join aluminum A2017 and carbon fiber reinforced epoxy composite.

The present MSc thesis was devised to evaluate the feasibility, joining mechanisms and the physics of FricRiveting of fiber reinforced thermoset composite-metal hybrid joints. For this purpose a material's science approach was used to study the correlations between FricRiveting process parameters, joint microstructure and quasi-static mechanical behavior, from advanced microstructural (optical and laser-scanning microscopy, SEM-EBSD, TEM) and physical-chemical characterization (TGA, ATR-IR spectroscopy) to the local (micro- and nanohardness) and global mechanical performance of the joints (lap-shear). Finally, an attempt to establish basic design guidelines of FricRiveting for thermoset-GFRP emergency bridges was proposed.

2 MOTIVATION AND OBJECTIVES

Recently, Borba *et al*. [16] have demonstrated the basic principles of joining Ti-6Al-4V alloy rivets with pultruded glass fiber reinforced thermoset polyester composite (GF-P) by FricRiveting. Despite addressing the basic description of microstructure and mechanical properties, the author did not study deeply the effect of the joining parameters on the microstructure of composite and metal parts nor its relationship with joint mechanical behavior. Furthermore, the joining mechanisms and the physical phases of FricRiveting of this complex material system are still not fully understood.

Based on these knowledge gaps, the motivation of the present study is to provide for the first time in the literature, a fundamental understanding on the Friction Riveting process for thermoset composites-metal dissimilar joints. For this purpose, the materials combination of Ti-6Al-4V/thermosetting GF-P friction-riveted joints was evaluated.

Therefore the objectives of this MSc work were divided into scientific and engineering objectives as following:

Scientific

- Establish a thoroughly understanding of the feasibility and physics of Friction Riveting process of pultruded continuous-fiber-reinforced thermoset composites.
- Understand the relationships between process, microstructure and mechanical properties of Ti-6Al-4V/GF-P friction-riveted metallic-insert and overlap hybrid joints.

Engineering

- Determine basic Friction Riveting joining guidelines for future GFRP-emergency bridges by applying structural calculations and safety factor standards to evaluate joint lap-shear strength and compare to bolted joints.

3 LITERATURE REVIEW

3.1 Joining Technologies for Hybrid Structures

3.1.1 Mechanical Fastening

For multi-material structures, traditional mechanical fastening easily enables the assembly/disassembly independently of the joining components' properties [17]. These methods comprise many variants which, in general, the principles are based on pressing parts together, such as screwing, and joining by forming such as clinching, folding and riveting. Some well-known fasteners are press-in-fasteners where, by protruding the metallic device, an interference fit with the hole is created into the joining part [18]. The self-piercing rivets are also widely used, for instance in automotive industry, where no pre-hole is necessary. In this case, by pressing the rivet against the joining parts, the self-piercing rivet is introduced, creating an intimate contact between the components [7, 19]. Clinching consists in deforming dissimilar sheets through continuous action of a punch, which induces material flow to die edges leading to undercut formation [20]. Therefore, in general, mechanical fastening requires simple surface preparation, simple handling and machinery [21].

The major concern of applying state-of-the-art mechanical fastening techniques to join composites or polymers is the high susceptibility of these materials to hole stress concentration [22]. Additionally, the introduced through-holes can expose the fibers in the composite leading to material embrittlement, for instance by water absorption [21]. Therefore, the goal of current studies on composite bolted joints has been to provide strategies to design joints that avoid extended damages and catastrophic failure [23]. The basic failure modes in bolted fiber reinforced polymer (FRP) composites are bearing, net-tension and shear-out failures [21, 24]. Figure 3.1 schematically presents these failure modes. Only bearing damage causes progressive failure, which is easily detected and predicted and is therefore desired in load bearing structures. Bearing failure occurs in the surroundings of the contacting bolt surface,

primarily due to compressive stresses [25]. The net tension and shear-out failure modes are response of excessive tensile stress on the net area though the fastener hole and excessive shear stress on the hole edge parallel to the load, respectively [26].

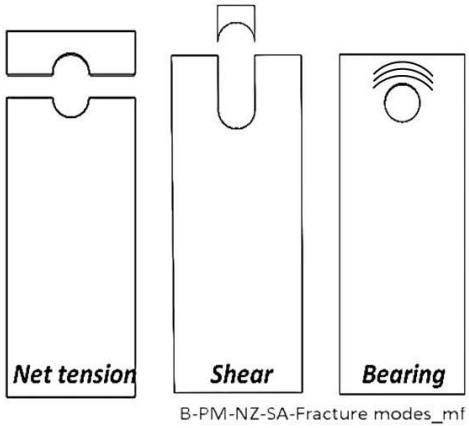

Figure 3.1 Main failure modes of bolted fiber reinforced polymer **(**FRP) composites (Adapted from [69]).

The design of bolted joints has been widely studied through bolting parameters since they dictate the joint strength and thus the predominance of certain failure mode. These parameters include: geometrical factors, such as the width-to-diameter ratio (*w/d*), edge distance (e) and clearance [27], bolt material [25], coefficient of friction [28], joint configuration [29], laminate lay-up and clamping torque [25, 30]. Some of the geometrical factors are detailed in Figure 3.2. According to Cooper and Turvey [31] larger *w/d* and sufficient edge distances favors the bearing failure, while small edge distances favor the shear-out or cleavage modes [32]. As demonstrated for carbon fiber reinforced epoxy laminates [30, 33], bearing strength is proportional to clamping pressure. On the other hand, high clamping torques induce out-of-plane (bending) stresses ; it may lead to premature failure of the joint [34], limiting the maximum value of clamping torque by standards. Facing this complexity, as reported by Olmedo *et al.* [35], it is essential that all the aspects of joint design are well understood, while the development of theoretical reliable models is required to optimize the prediction of bearing strength and failure mode in composite fastened joints.

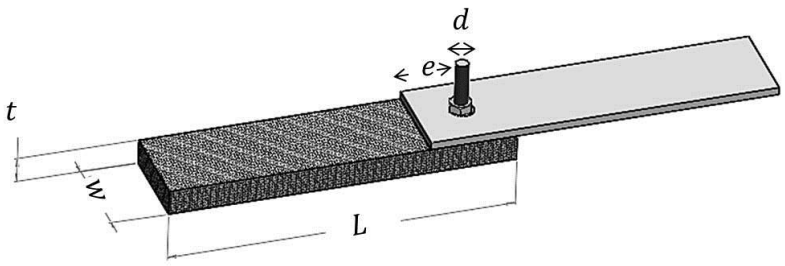

Figure 3. 2 Single lap bolted specimen showing the relevant joint dimensions.

Applications of mechanical fastening are numerous and well established in the market. In the automotive industry, the Audi TT and Audi A8 use approximately 2000 half-hollow self-piercing rivets in structural parts while fender and tail cover of Mercedes-Benz CLX are assembled using screws [36]. In aircraft, this technique is used to join spars in the wing box and fuselage [37]. In infrastructure, the main applications are in metallic decks, bridges, facade profiles, structural timber and interior finishing such as wiring accessories and sanitary ware [38].

3.1.2 Friction Riveting

General Process Principles, Parameters and Variables

Friction Riveting (FricRiveting) - a recent development in solid-state joining technologies for polymer-metal hybrid structures - was patented by Helmholtz-Zentrum Geesthacht, Germany [8-9]. FricRiveting is a friction-based joining process which relies on the principles of the mechanical fastening and friction welding. In general, the technique can overcome the limitations of the conventional assembly methods ensuring advantages, as follows: little or no surface preparation is needed; no obligatory through-holes are required; hermetically sealed joints can be achieved without the use of sealants; reduced number of process steps and short joining cycles, leading to potential cost savings [39]. Despite these benefits, the process presents intrinsic limitations such as the impossibility of disassembly, minimum substrate thickness required and only spot-like joints are enabled [40].

Up to now, the physical description of the process phases is based on the initial development of the technique for hybrid unreinforced thermoplastic-metal joints using the time-controlled variant. Rheological phenomena occurring in the polymer during the FricRiveting were the basis of the current technology knowledge and the mathematical modeling for the heat generation proposed by Amancio-Filho [39]. The effect of the continuous fiber reinforcements and thermoset matrix on the evolution of the process phases and the heat generation was not investigated yet. Therefore, the present work is the first contribution in joining thermosetting composites by Friction Riveting.

The basic configuration of the process (Figure 3.3) consists in rotating and inserting a cylindrical metallic rivet into a stationary polymeric base plate (metallic-insert joint geometry). In the early joining phase, after the positioning of the joining parts (Figure 3.3-a), the rivet is rotated, achieving the pre-set rotational speed, and pressed against / inserted into the surface of the polymeric component (Figure 3.3-b). Due to the friction between the rivet and the polymer and the low thermal conductivity of the polymer, the temperature rises locally, forming, in the case of thermoplastics, a thin softened/molten polymeric layer underneath and around the tip of the rotating rivet. As the rivet penetrates continuously into the thermoplastic plate, the softened/molten polymer is expelled outward of the joining area. At the end of the frictional phase, the generated heat favors the plasticizing of the rivet tip at temperatures below the metal melting point. As the rotation is decelerated, the axial force is increased - the so called forging phase (Figure 3.3-c). During forging the remaining softened/molten material is expelled towards the flash and the rivet tip encounters resistance of the colder thermoplastic volume. The plasticized rivet tip is thereby deformed into a parabolic pattern (Figure 3.3-c). Recent studies show that the forging phase may be skipped when process parameters are set up to induce enough amount of metal plasticizing at the rivet tip [14]. Finally, the joint consolidates under pressure (Figure 3.3-d). The joining mechanisms relies on mechanical anchoring and adhesive forces at the polymer-metal consolidated interface [41].

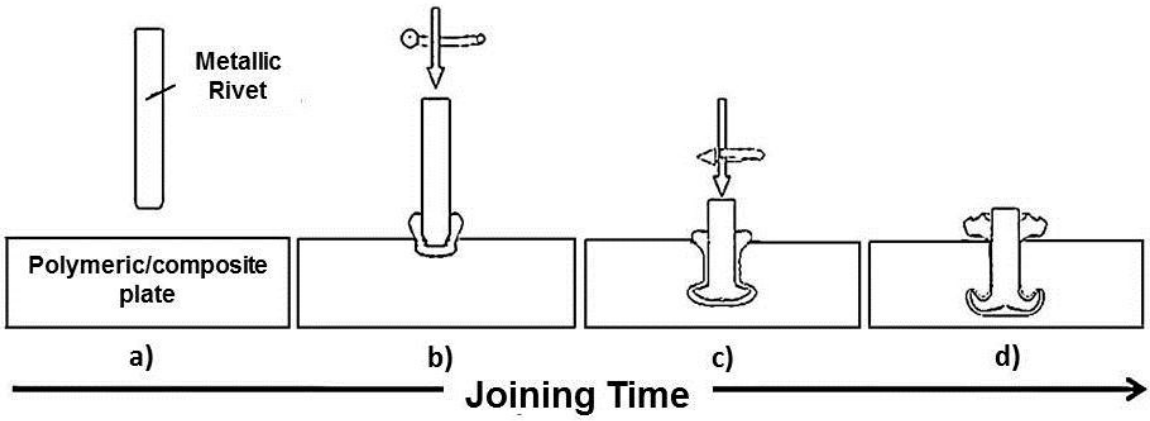

Figure 3. 3 Schematic of the Friction Riveting process for metallic-insert joints in thermoplastics. a) Positioning of the joining parts; b) insertion of the rivet into the polymer during the frictional phase; c) deceleration and rivet forging and d) consolidation of the joint (Adapted from [42]).

The joining process can be controlled either by time, force, displacement or the combination of these variants [14]. The time-controlled FricRiveting is a consolidated and well-known variant widely reported in the literature [10, 12-13, 42-43]. The main processing parameters of this process variant are the *rotational speed* (RS), *joining pressure* (JP) and *joining time* (JT). The *rotational speed* (RS) is the rivet angular velocity which influences directly the heat generation and, consequently, the process temperature. The *joining pressure* (JP) consists in a sum of *frictional pressure* (FP) and *forging pressur*e (FOP) and corresponds to a normal pressure distribution in the frictional area. The *joining time* (JT) comprises the *frictional time* (FT) and *forging time* (FOT). JT contributes to control the joining speed and frictional heating. Therefore, this parameter influences process-related phenomena such as thermal degradation, volatilization of additives and structural water and post-joining shrinkage in the polymeric component. Some of the major process variables are the *burn-off* (BO) which indicates the level of the rivet penetration and consumption length and *burn-off rate* (BOR) which is the quotient between BO and the heating time (HT) – the interval from the touchdown of the rivet up to the complete rivet deceleration.

Physical Description

According to Amancio-Filho [44], the physical description of the Friction Riveting for “metallic-insert” joints of thermoplastics comprises five phases involving different axial displacement and frictional torque evolutions over the joining time:

- *Phase I*: friction in solid state (Coulomb friction) at initial stage when the axial displacement is zero and the torque increases slightly. After a very short period, the torque decreases with the friction coefficient due to the shearing between polymer-polymer surfaces;
- *Phase II*: unsteady state viscous dissipation when the temperature exceeds the transition temperature of the polymer (glass transition temperature for amorphous and melting point for semi-crystalline polymers). The rivet penetration depth and torque gradually increase;
- *Phase III*: steady state viscous dissipation which is characterized by linear increase of axial displacement over time and constancy in torque measurement. In this phase there is a balance between polymer melting and molten material squeezing out (flash formation rate). At the end of this phase, the desired plasticizing level in the rivet tip is achieved;
- *Phase IV*: rotation is stopped and axial pressure applied. The plasticized rivet tip plastically deformed into a parabolic pattern;
- Phase V: consolidation of the joint by cooling under pressure. An interface is generated between the metal and the polymer which bonds them together. The frictional torque trends to zero and the axial displacement reaches its maximum becoming constant until the end of the process.

Microstructural Zones

According to Amancio-Filho [39], the temperature reached in FricRiveting and the heat dissipation are responsible for different thermal/thermo-mechanical phenomena in the joining components. Many possible hardening and annealing

processes can take place in the metallic rivet while phenomena such as physical ageing and physicochemical transformations can be evidenced in the polymeric/composite plate [45]. The author identified five typical microstructural zones affected by the heat and shear for “metallic-insert” joints of thermoplastics [41] (Figure 3.4).

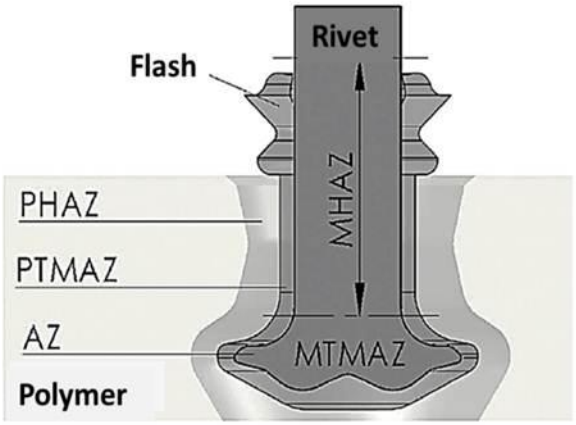

Figure 3. 4 Schematic of microstructural zones and geometry of a typical friction-riveted “metallic-insert” joints of thermoplastics (Adapted from [41]).

Usually, the extension of the *polymer heat affected zone* (PHAZ) cannot be visually identified since this polymeric volume did not reach the material transition temperatures - T_g and/or T_m - during joining. However, phenomena such as induced crystallization for semi-crystalline polymer and physical aging for amorphous polymer may occur. The *polymer thermo-mechanically affected zone* (PTMAZ) is formed by softened/molten polymeric layer attached to the rivet surface. This region is exposed to high shear rates which may cause chain reorientation and oxidative thermo-mechanical degradation as well. In short-fiber reinforced composites a stir zone - thin zone adjacent to the rivet shaft- has been identified [46], where fibers are re-oriented follow the induced flow by the rotation of the rivet.

The *metal heat affected zone* (MHAZ) is visually unchanged. However, annealing processes such as static recovering, recrystallization and overaging, as well as some hardening mechanisms such as ageing and re-precipitation, may occur. The metal *thermo-mechanically affected zone* (MTMAZ) is exposed

to high temperatures and considerable mechanical deformation leading to microstructural transformations such as: partial or complete grain refinement, grains and sub-grains formation attributed to dynamic recovering, dynamic recrystallization and re-precipitation. Recently, Altmeyer *et al.* [46] subdivided the MTMAZ into three substructures: MTMAZ-1, MTMAZ-2 and metal frictional zone (MFZ). In summary, they showed that MTMAZ-2 has a microstructure formed as result of larger amount of plastic deformation and temperature than MTMAZ-1. MFZ is characterized by very fine grains (0.7 μm) induced by dynamic recrystallization due to the high shear rates and temperatures at the lower interface of the rivet in the AZ; the authors claim that this is mainly due to the interaction of fibers with titanium rivet. However, a detailed explanation of the process-related phenomena which controls this zone was not provided. The *rivet anchoring zone* (AZ) is the region where the rivet tip assumes a parabolic pattern after the forging phase. Rodrigues *et al.* [10] addressed the AZ as a geometrical change of the rivet tip, being a volume including the MTMAZ.

Rivet Anchoring Efficiency through the Volumetric Ratio Concept

Blaga *et.al* [12] introduced a simplified geometric model to define the anchoring efficiency of metallic-insert joints by measuring the polymer interaction volume above the deformed rivet tip (Figure 3.5). The *volumetric ratio* (VR) was devised for GF-PEI and commercially pure titanium grade 2 (Ti gr. 2) riveted joints and validated for other combinations of materials such as aluminum AA2024-T3 rivet and unreinforced polycarbonate (PC) [10] and unreinforced polyether imide (PEI) [47]. VR can provide a good estimation of the tensile mechanical behavior. Analytically, it is expressed by Equation 3.1.

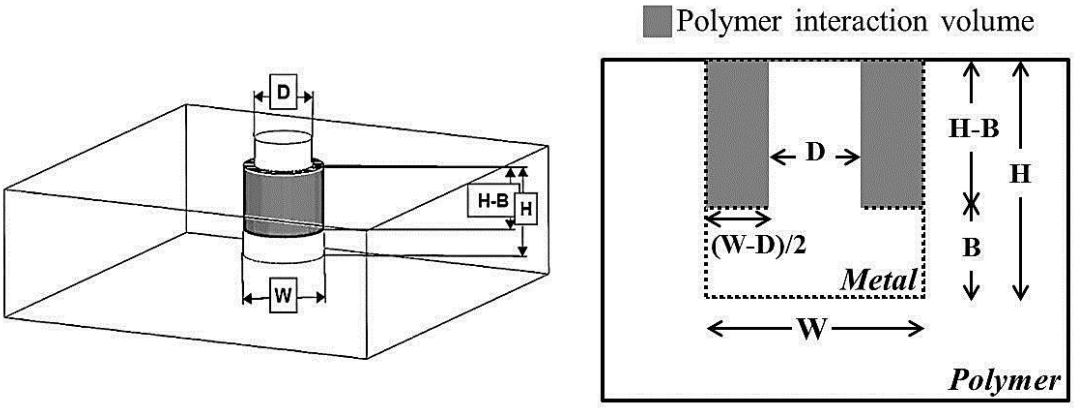

Figure 3. 5 Simplified geometry used to calculate the volumetric ratio emphasizing the interaction volume in gray (Adapted from [12]).

$$VR = \frac{(H-B)(W^2-D^2)}{W^2.H} \quad (3.1)$$

where W is the width of the deformed rivet tip; H is the rivet penetration depth; B is the height of the anchoring zone and D is the original rivet diameter.

Current Developments

The feasibility of FricRiveting was successfully demonstrated for metal-insert hybrid joints of aluminum AA2024-T3 with unreinforced thermoplastics such as polycarbonate (PC) [10] and polyetherimide (PEI) [11]. Furthermore, thermoplastic composites such as glass fiber reinforced polyamide 6 (GF-PA6), short carbon fiber reinforced poly(ether-ether-ketone) (CF-PEEK) [13] and glass fiber reinforced polyetherimide laminate (GF-PEI) [12] were also joined by this process using lightweight metallic rivets. Previous work on hybrid Ti gr.2/ GF-PEI friction-riveted joints addressed the comparison between the joint strength of friction-riveted joints and conventional bolted joints [43]. The ultimate lap shear forces were comparable reaching values around 5 kN [43]. Recently, Altmeyer [48] investigated woven carbon fiber reinforced poly(ether-ether-ketone) overlap friction-riveted joints joined with Ti gr.3 rivets. By applying a clamping torque of 5 Nm, ultimate lap shear forces of 8.1 ± 0.3 kN could be achieved

Similarly to mechanical fastening, the fibers exposure through the rivet drilling action can damage the composite and consequently compromising the joint properties. The presence of fibers also implies changes of the friction coefficient during the frictional phase, inhomogeneous heat distribution in the joining area and may results in uniformity in the stress distribution around the rivet shaft. Facing this complexity, the physical description of the processing phases for metal-insert joints of fiber reinforced polymers is still not fully understood.

General Joint Design Considerations on Joint Mechanical Performance

The development of better bearing strength of polymeric composite bolted joints has been widely investigated in the sense of establishing the key-design parameters and, consequently, optimized joint design [23, 25, 30, 35]. Considering the similarities between this traditional technique and FricRiveting, a similar approach can be assumed in order to enhance the mechanical performance of friction-riveted joint. Recent studies on FricRiveting have demonstrated that the potential key-design parameters for friction-riveted joints are: joint geometry including width-to-rivet diameter ratio (w/d) and edge-distance (e) and clamping torque [48]. As in mechanical fastening, similar effects of these factors on the joint mechanical performance are expected. By increasing the w/d and e, the bearing resistance is improved leading to a non-catastrophic failure mode [31]. Furthermore, the clamping torque can either increase the bearing resistance of joints or introduce damages in the composite joining area and, consequently, decrease the mechanical strength [25]. More details can be found in the work of Altmayer *et al.* [48].

Additional factors that should be considered are the rivet material to prevent galvanic corrosion and the rivet profile. It is expected that by introducing threads on the rivet surface, this provides a drilling effect during the friction phase of Fricriveting, resulting into higher insertion depths. Previous works have shown results consistent with these predictions [47, 49]. However, Blaga *et al.*

[47] observed that for the hollow-threaded riveted specimen of glass fiber reinforced polyetherimide (GF-PEI) and aluminum A 2024-T351, the amount of volumetric flaws and thermally degraded material were higher than for the plain rivet specimens, which was possibly explained by the higher heat input generated. An asymmetrical deformation of the rivet tip for hollow and hollow-threaded rivets was also observed [47]. Furthermore, threaded rivets can lead to rivet buckling during the process due to the reduced rivet cross-sectional area. However, the tensile testing results from Blaga [47] showed that, under the same joining parameters (same heat input), hollow-threaded rivets had a better mechanical performance than plain rivets, with up to 5 times higher ultimate tensile forces (1481 ± 230 N and 294 ± 80 N, respectively). The large deviation of the tensile force for hollow-threaded rivets was attributed to the presence of volumetric flaws and differential rivet tip deformation. Borges [49] reported the decrease of the strength under lap shear testing for the same combination of materials using hollow-thread rivet. The author partially explained this decrease by the inadequate application of excessive clamping torque, which was detrimental to joint integrity [49].

3.2 Titanium Alloy Ti-6Al-4V

3.2.1 General Features and Microstructure

Titanium grade 5, commonly called Ti-6Al-4V alloy, is a low-density material (approximately 60% of the density of the steel and superalloys) developed after the Second World War to attend material requirements of good corrosion resistance and high strength in aeronautical and aerospace applications [50-51]. Although those fields are still the most consuming of titanium and its alloys, they have been also applied in automotive, power generation, petrochemical and medical applications. [52] Currently, metallic fasteners used in aircrafts are typically made of Ti-6Al-4V alloy to reduce galvanic corrosion [51]. Moreover, the possible superplasticity of this material

enables its use in the fabrication of engine nacelle components through superplastic forming applied, for instance, in the Boeing 757 aircraft [53].

Microstructurally, the Ti-6Al-4V alloy comprises a mixture of low temperature alpha (α-Ti) phase and high temperature beta (β-Ti) phase, coexisting at room temperature. The crystal lattice of alpha phase (α-Ti) contains atoms arranged in a close-packed hexagonal array (hcp), which are responsible for the excellent strength of the alloy. The number of slip systems for the hcp crystal structure is limited to 12, hindering the homogeneous plastic deformation. The limited ductility of this phase is the result of additional deformation on secondary slip systems as well as possible mechanical twinning [54]. The hcp structure also presents a low stacking-fault energy which has strong influence on the recovery and recrystallization phenomena and hence on the resultant texture of the alloy [55]. The beta phase (β-Ti), has a crystal structure consisting of body-centered cubic (bcc) arrays, providing good ductility to the metal [56]. This occurs due to the 48 multiple independent slip systems presented in the bcc crystal structure. Therefore, Ti-6Al-4V alloy is classified as belonging to the α+β Ti alloys. The titanium phase diagram in Figure 3.6 summarizes the families of titanium and titanium alloys: α alloy, near α alloy, α+β alloy and β alloy. The families are classified according to the alloying element concentration and the start (M_s) and final (M_f) martensitic transformation lines.

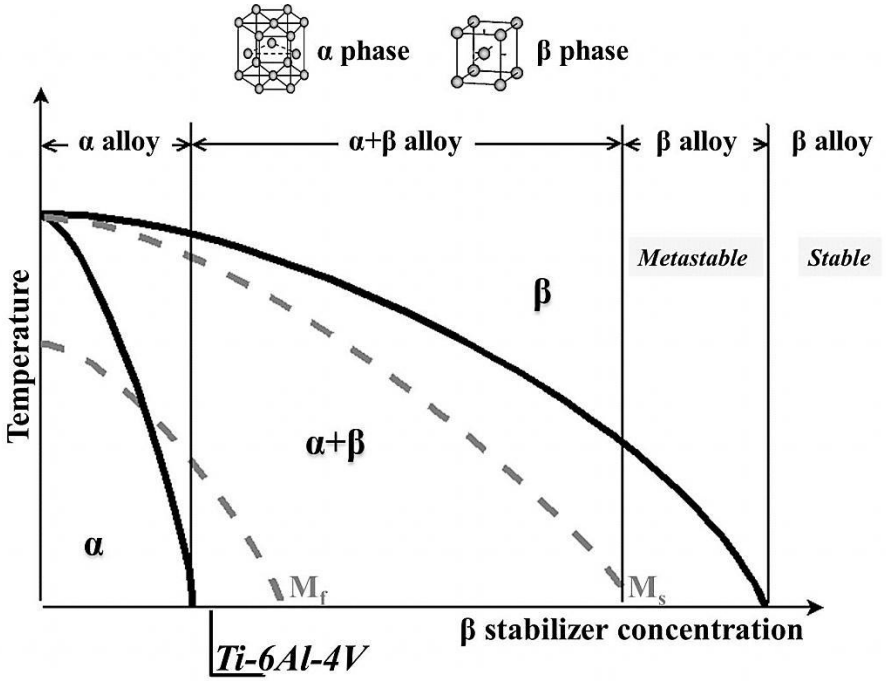

Figure 3. 6 Titanium alloy compositions and their classes relative to a pseudo-binary titanium phase diagram (Adapted from [56]).

The aluminum (Al) element stabilizes the α phase while oxygen, nitrogen and vanadium enable the development of β phase at low temperatures [56]. The Al content threshold is nearby 6 wt. %. Above this limit, harmful inclusions such as Ti_3Al can be formed leading to the alloy embrittlement. By increasing the oxygen content, more inclusions are formed [57]. Furthermore, a balance between the phase stabilizers is essential to provide an effective microstructure and consequently a better control of the chemical and mechanical properties [56].

The microstructure of the Ti-6Al-4V alloy is thermo-mechanical process-dependent. Figure 3.7 summarizes the main Ti-6Al-4V microstructures developed from three hypothetical cooling rates: I - fast cooling from β-field, II - slow cooling from β-field and III - slow cooling from α+β field. A qualitative phase diagram including temperature-, time- and chemical composition-dependences was added in the figure [58]. The ω-Ti phase and its transformations were included in the diagram. However, this metastable phase is not usually detected in Ti-6Al-4V microstructures remained from welding processes and therefore will be not discussed in this section.

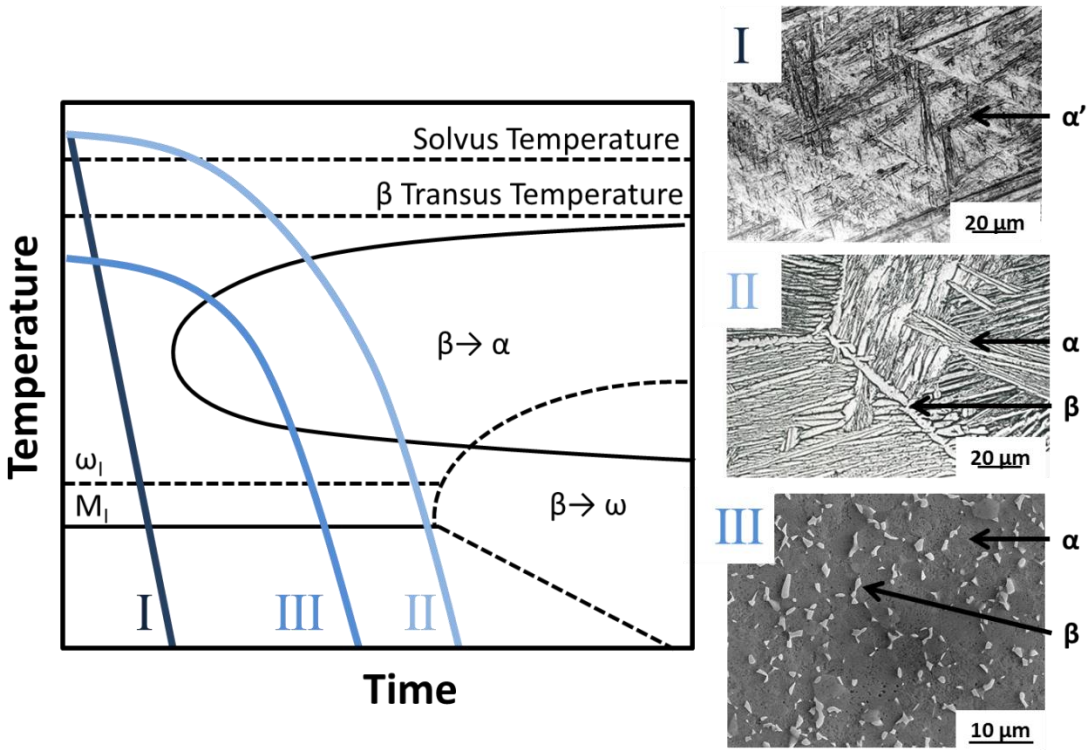

Figure 3. 7 Continuous cooling transformation (CCT) diagram of α+β titanium alloy. Characteristic microstructures when cooling starts from temperatures above β-*transus* temperature such as martensite (fast cooling rate) (I) and Widmanstätten α+β (moderate cooling rate) (II) and from temperatures below β-*transus* such as bi-modal microstructure consisting of globular β grains in transformed β matrix (III) (Adapted from [58]).

The acicular morphology resultant of fast cooling rate from β-Ti phase field - above Ti-6Al-4V *solvus* temperature - (curve I, Figure 3.7) represents β→α phase transformation in a non-thermodynamic equilibrium, occurring through a diffusionless process (martensitically). The martensite transformation involves the movement of atoms by shear-type process and does not lead to embrittlement; however, the strength is slightly increased compared to α-Ti phase [54]. The result is a homogeneous transformation of the bcc phase into hcp (α') or orthorhombic (α") crystal lattice lamellar packages over the given volume [59]. For low alloying element content and fast cooling rate, α' is formed preferentially. The martensite starting temperature (M_s) is a function of the impurity level (O, Fe).

Upon slow cooling in a thermodynamic equilibrium from the β-Ti phase field (curve II, Figure 3.7) the most densely packed planes of bcc structure, *i.e.* {110}, transform to the basal planes {0001} of the hcp structure with certain volume shrinkage [54]. There is a specific temperature range, called β-*transus* temperature, in which this takes place and depends on the titanium purity [60]. The corresponding transformation follows the Burgers relationship where parallel planes correspond to close-packed planes, $\{110\}_{\beta\text{-Ti}} \parallel \{0001\}_{\alpha\text{-Ti}}$, whereas the parallel directions relate to the nearest-neighbor directions, $<11\bar{1}>_{\beta\text{-Ti}} \parallel <11\bar{2}0>_{\alpha\text{-Ti}}$ [61]. The six slip planes and two slip directions of the α-Ti phase give maximum 12 variants of orientation to the α-Ti phase during β-Ti transformation. This variety of orientations reflects in the formation of lamellar microstructure, called Widmanstätten [54]. The Widmanstätten microstructure is characterized by the nucleation of individual α lamellar packets and growth from retained β grains [56].

Below the β-*transus* (curve III, Figure 3.7), time and temperature-dependent phase transformations are less intense due to high atomic packing attributed to hcp crystal structures [54]. Thus, slow cooling from α+β field at temperatures below β-*transus* leads to typical equiaxed morphology which is characterized as α matrix with β phase growing in α-grain boundaries [62]. However, when plastic deformation and temperature are simultaneously applied, dynamic metallurgical phenomena, such as dynamic recrystallization (DRX) can occur in Ti-6Al-4V. Liao *et al*. [63] reported that the critical temperature to initiate the DRX process for Ti-6Al-4V alloy range from 660 to 830°C, corresponding to 40-50% of the melting temperature of the alloy (1660°C). At this temperature range, recrystallized grains nucleated in the narrow of the adiabatic shear bands -zone of highly localized deformation usually formed in materials with low strain hardening rate and low thermal conductivity [64].

Table 3.1 compares the advantages of equiaxed and acicular morphologies of α+β alloys [60] which dictate the applicability of the material in the industries.

Table 3. 1 Comparison of advantages between equiaxial and acicular morphology of α-β alloys [60].

Equiaxial	Acicular
Good ductility	Better creep properties
Good formability	High fracture toughness
High strength	High corrosion resistance

3.2.2 Welding and Joining of Ti-6Al-4V

The microstructure evolution is a key issue in welding and joining processes since this fundamental knowledge allows controlling weld/joint mechanical properties. Facing the complexity discussed above, a particular challenge is to understand microstructural development in Ti-6Al-4V welds/joints.

Conventional welding processes such as *Gas Tungsten Arc Welding* (GTAW), *High Vacuum Electron Beam Welding* (EBW), *Laser Beam Welding* (LBW) and solid state welding processes such as *Ultrasonic Welding* and *Friction Stir Welding* (FSW) have been commercially used to join Ti-6Al-4V alloys. Recently, the influence of the process parameters on the final microstructure and its evolution in similar and dissimilar Ti-6Al-4V joints have been widely explored in the literature [52, 65–68].

In GTAW, increase in the arc current leads to high heat input and hence low cooling rate, favoring α-grain coarsening, formation of Widmanstätten structure and brittle intermetallic compound in similar Ti-6Al-4V welds [66-67]. The significant oxygen contamination in the welding surface resulted in a predominantly acicular morphology [68]. According to Balasubramanian *et al.* [66], the tensile strength, hardness and the impact resistance of GTAW welds were compromised by the grain growth and the presence of porosity in the coarse weld bead. For EBW, LBW and FSW, the refinement of the disoriented alpha acicular grains and the martensitic transformation owing to low rotational speed (low energy input) and the fast cooling rate improved the tensile strength

of the welds and increased the hardness of the process-related microstructural zones [66-67, 69]. Akman *et al.* [70] revealed that for LBW with the narrowest weld bead, the microstructure and the porosity dictated negatively the weld's mechanical performance. Zhu *et al.* [71] reported an increase in hardness of both matrices of dissimilar Ti-6Al-4V alloy and aluminum A6061 ultrasonic welds by improving the welding pressure and time. The authors attributed the increase to the apparent diffusion of Ti and Al elements across the welding interface [71].

Microstructure evolution and final microtexture of Ti-6Al-4V alloy friction stir welds have been investigated by Mironov *et al*. [72]. The predominant deformation during the FSW is expected to be simple shear which can be assessed by the planes/directions of the bcc structure [55]. During FSW, the material experiences phase transformation and plastic flow at high temperature β-field, which cannot be directly observed on the final microstructure of α+β alloy after the joint consolidation [73]. Although the retained β-Ti phase can provide insights into the material flow, the fraction of this phase is usually too low hindering the textural measurements. Thus, Mironov *et al.* [74] proposed to use textural information from the major α-Ti phase to assess the simple-shear texture of β-Ti phase by considering its (0001) and $(11\bar{2}0)$ pole figures. This is a rough approach based on the Burgers orientation relationship since the (110) and (111) pole figures in β-Ti phase are similar to the respective (0001) and $(11\bar{2}0)$ pole figures in the α-Ti phase [74]. This method has been successfully used for the texture analysis in the near-α titanium friction-stir welds as well [75].

Nevertheless, only few studies have addressed hybrid joints comprising Ti-6Al-4V and polymers/composites. Ramani *et al.* [76] assessed poly(ether-ketone-ether-ketone) (PEKEKK) as a hot melting adhesive for joining Ti-6Al-4V plates. The authors obtained high strength joints (average tensile strength of 137 MPa, exceeding by 16% the base polymeric material tensile strength of 118 MPa) using controlled soak time above the melting temperature of the PEKEKK; this strategy removed the residual spherulitic crystals in the polymeric adhesive [76]. The joints failed by cohesive failure in the adhesive. Recently, Blaga *et al.*

[12] proved the feasibility of Friction Riveting on hybrid joints comprising glass-fiber reinforced poly(ether-imide) laminate (GF-PEI) and commercially pure titanium grade 2. The anchoring efficiency of the metallic rivet into the composite was analyzed by the correlation between the rivet volumetric ratio (geometric model to define the anchoring efficiency of the metallic-insert joints through the polymeric interaction volume above the deformation of the rivet tip) and the mechanical performance of the joints, showing their direct dependence, for the studied material combination. Neither metallurgical transformations nor physicochemical changes in the composite were studied, as well as their influences. Using the same joining technology, Altmeyer *et al*. [13] joined short carbon-fiber reinforced polyether ether ketone (CF-PEEK) with a titanium grade 3 rivet, as a metallic insert. The authors investigated the influence of the process parameters on the mechanical behavior of the joints by means of design of experiments. They determined an optimized joining condition resulting in ultimate tensile strength of 10.7 kN, which corresponds to the base material strength of the titanium rivet [13].

3.3 Glass Fiber Reinforced Thermoset Polyester

3.3.1 General Characteristics and Microstructure

The Glass Fiber Reinforced Thermoset Polyester (GF-P) offers advantages such as low cost, low weight, high electric and chemical resistances and outstanding mechanical properties [77]. Due to these benefits, GF-P have been used in many fields including naval constructions, offshore applications, water piping, civil infrastructures, blades for wind turbines and automotive industry [38]. However, some limitations of the composite are the brittleness, thermal instability , hydrolytic susceptibility and high flammability [78-79].

The thermoset polyester matrix is obtained by the crosslinking of an unsaturated polyester resin with styrene monomer through free radical chain growth mechanism. The resultant chemical structure consists in a rigid, three-dimensional, network structure (Figure 3.8). Once the cross-links are formed,

the thermoset polymer cannot be melted and remolded by the application of heat or pressure [6].

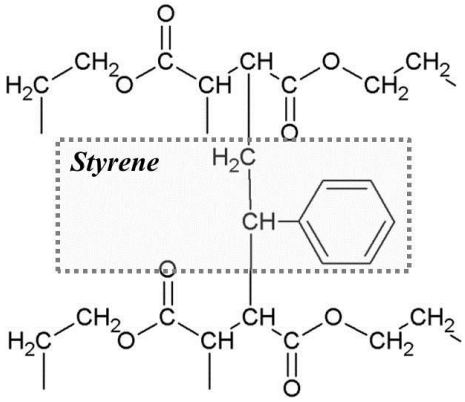

Figure 3. 8 Molecular structure of a thermoset polyester crosslinked with styrene monomer.

The unsaturated polyester molecule is synthesized through condensation polymerization of unsaturated poly-acids or acid anhydride and polyhydric alcohols, using peroxides as catalysts [80]. Mainly, three types of resin are commercially used: orthophthalic acid polyester, isophthalic acid polyester and vinylester, differing from the acids, alcohol and additives used in their preparation [81]. The thermo-physical and mechanical features of the resin depend on its formulation/composition and the processing temperature, which are specifically designed based on their application (final product). Isophthalic polyester is used in marine applications where its superior corrosion and temperature resistances are desirable [81].

Flame retardants are the most used polymer additives in this kind of composite. The most common are those based on halogens such as brominated and chlorinated organic compounds, antimony trioxide and aluminum trihydroxide [38].

GF-P structural profiles applied in civil engineering are manufactured mainly by pultrusion process [38]. This process is characterized by continual reinforced material being pulled through a guide where the fibers are placed in relation to the profile cross section; the fibers are then led though processing equipment where the fibers are impregnated with the matrix resin. This combination of resin and fiber is heated up curing in a final geometry [82]. In the composite body, the fibers are oriented in 0° (parallel) and 90° (transversal) in

relation to the pultrusion direction. Near the surfaces, a reoriented fiber layer in ± 45° is added. Finally, a cover layer of polyester resin protects the material against chemicals (Figure 3.9). The thermal and mechanical properties of the composite are anisotropic and dependent on the fiber content, through-the-thickness fiber orientation and the quality of the fiber/matrix interface. The static coefficient of friction increases according to: the fiber content (from μ_e = 0.5 to μ_e =0.7 for 20% and 50% of short glass fiber, respectively); the sliding speed and adding coupling agent (from μ_e = 0.6 to μ_e = 0.7 for composite without and with coupling agent, respectively) [83].

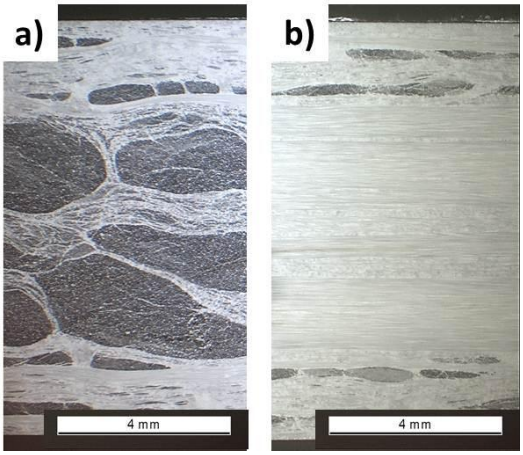

Figure 3. 9 Microstructure of pultruded GF-P plate with nominal 50 wt.% of glass-fiber content in the (a) cross- section and (b) longitudinal section.

Laoubi *et al*. [84] investigated the thermomechanical behavior of a similar GF-P composite (laminated instead of pultruded) though dynamic mechanical analysis (DMA). The peak of the loss modulus (E'') curve as a function of temperature yielded information of the glass transition temperature (T_g) and its changes between the polyester resin and the GF-P. The authors identified the T_g for the composite of approximately 82°C, 22% higher than the T_g for the pure resin (64°C) which suggested that the mechanical properties vary with the temperature, depending on the glass-fiber reinforcement [84].

3.3.2 Glass Fiber Reinforced Thermoset Polyester Degradation Mechanisms

The literature proposes several thermal degradation mechanisms for thermoset polyester [85-86]. Polyester resins from different poly-acids and poly-alcohol have significant differences in the degradation products, which in turn can be used to identify the resin composition [81]. According to Laoubi *et al.* [84] the degradation under nitrogen atmosphere and flowing air takes place in two steps between 180°C and 400°C. The first step starts just before 180°C and the maximum decomposition rate is 0.63%/min at 204°C. Substantial volatilization of low molecular weight gases occurs. In the second step, the maximum rate is 6.72%/min at 386°C. The resin decomposes rapidly through an endothermic reaction of random-chain scission of the polystyrene cross-links leading to free radicals formation. The presence of free radicals induces further decomposition. The residues, such as simple ester, can undergo pyrolysis during the heating up [87]. Other decomposition products are methane, ethylene, propylene, benzene and toluene [87]. Furthermore, Laoubi *et al.* [84] investigated by infrared spectroscopy the thermal degradation of the polyester resin heated at 280°C. The authors observed an increase in the intensity of the alcohol functional group vibration bands at 3400-3600 cm^{-1} and decrease of the alkoxy group stretching vibration band at 1150-1380 cm^{-1}, which confirmed the degradation of the resin [84].

Anderson and Freeman [86] assessed the thermo-oxidative degradation of orthophthalic based GF-P and concluded that oxygen attacks styryl groups forming hydroperoxide groups (Figure 3.10-a). Another mechanism proposed by the authors considered only the influence of the heat which contributed to the formation of either carbon dioxide and propylene or carboxylic acid (Figure 3.10-b) [86].

Bahadur *et al.* [83] showed that the photo-oxidation of GF-P generates hydroxyl/hydroperoxide groups, as detected by the broadening of the corresponding band of 3200-3500 cm^{-1} in the infrared spectra. The generation

of hydroperoxide group was also identified by Anderson and Freeman [86] during the thermo-oxidation of GF-P.

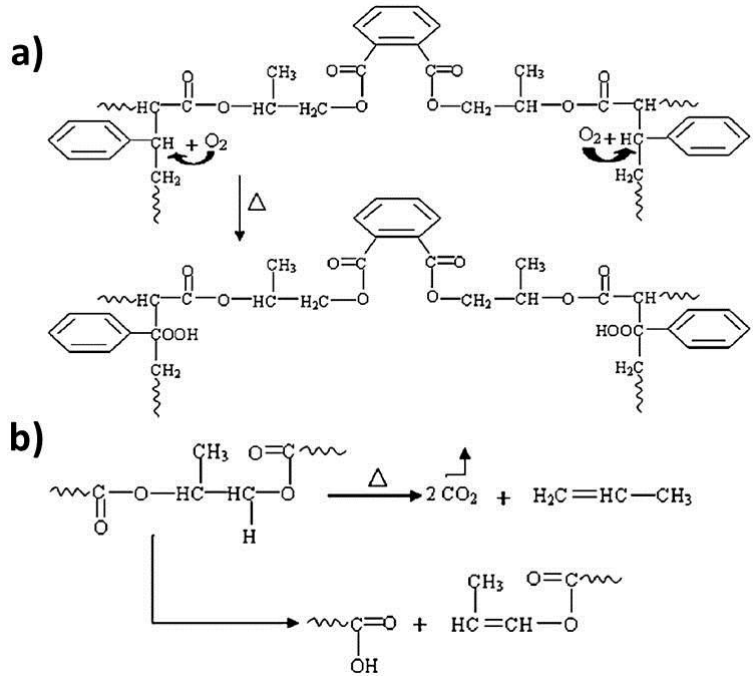

Figure 3. 10 a) Thermo-oxidative decomposition of orthophthalic based thermoset polyester and the formation of hydroperoxide group; b) thermal decomposition of the resin and volatilization of CO_2 (Adapted from [53]).

3.3.3 Joining of Glass Fiber Reinforced Thermoset Polyester

Typical joining methods for GF-P include mechanical fastening and adhesive bonding [88]. Recent studies [89–91] investigated the quasi-static and cyclic behavior of epoxy adhesively bonded joints of pultruded GF-P. These joints have been widely used in existing civil engineering structural applications of GF-P [92]. Keller and Tirelli [92] performed fatigue test using epoxy adhesively bonded GF-P double lap joints and observed that the fatigue limit withstood the fatigue stress amplitude usually observed in bonded connections of typical GFRP bridge structures. However, the failures occurred in a brittle way, *i.e.* catastrophically. Similar behavior was reported by Zhang *et al.* [89] for bonded joints under tensile loading. Kim *et al.* [93] showed that by varying the geometric configuration, the step length of stepped lap joints and the edge angle of adherends, the fatigue life and strength were increased.

Regarding mechanical fastened GF-P joints, recent studies are focused on the improvement mechanical performance of bolted joints [94-95]; emphasis has been set mainly in the optimization of joint geometry, composite fiber orientation and fiber stacking sequences. Abd-El-Naby and Hollaway [96] evaluated pultruded GF-P bolted connections in a double-lap configuration with different widths (w) and edge distances (e). The authors showed that by increasing *w* and *e,* the joint resistance was improved [96]. They also highlighted that specimens with increased thickness of continuous fiber mat layer allowed the composite plate to redistribute the stress more homogeneously, favoring non-catastrophic failure modes [96]. Popoaei *et al*. [95] compared the lap shear strength of adhesively bonded, bolted and hybrid GF-P joints. They showed that the best mechanical performance was achieved by hybrid joints which combined mechanical and adhesively bonded solutions. By comparing these three joint configurations, the ultimate lap shear strength of hybrid joints increased 5% and 31% in comparison with bolted and adhesively bonded joints, respectively. Additionally, the authors evidenced an increase of 23% in strength for clamping torque of 10 N-m in comparison to unclamped / hand tightened joints [95].

4 EXPERIMENTAL APPROACH

The experimental approach of this research work was divided into five main phases. In the first phase, the feasibility of FricRiveting for the selected materials combination, pultruded glass fiber reinforced thermoset polyester (GF-P) and Ti-6Al-4V alloy, was evaluated. Moreover, the process parameters screening was undertaken using the one-factor-at-a-time (OFAT) approach. The influence of individual process parameters (RS, FT, FOT, FP, FOP) on the tensile strength of the metallic-insert joints was evaluated through T-Pull tensile testing, minimizing and validating the range of variation for each parameter. Further, the mechanical performance of tensile specimens was correlated to the geometry of the deformed rivet (rivet penetration depth and width) by means of volumetric ratio – indirect measurement of the anchoring efficiency. The results of this phase are not included in the thesis.

In the second phase of the work, the characterization of the base materials was carried out. This involved a thorough investigation into their microstructure, thermal behavior and local and global mechanical properties. Mainly light optical microscopy (LOM), SEM, TEM, chemical microanalysis (SEM/EDS, TEM/EDS), crystallography (EBSD), thermal analysis (DSC, TGA), microhardness, nanohardness and tensile testing were used for this purpose. Further, the results obtained in this phase were compared to the above mentioned aspects of friction-riveted joints, which were obtained in phase four of the work.

Once the rage of process parameters was defined, three conditions whose joints achieved good rivet anchoring and sufficient mechanical performance were selected in the third phase of the work. At this phase, the physics of FricRiveting process for continuous fiber reinforced thermoset composites was investigated. For this purpose, the temperature evolution and the frictional torque were monitored during the joining process. The energy input of each joining condition was calculated based on the torque measurement and, further, correlated to the process temperature. The selected joining conditions were used from phase three to phase six of this work.

In the fourth phase, a detailed analysis of the joints was carried out. This involved a thorough investigation into the process-related physicochemical changes in the composite, the microstructural transformations in joining parts, investigation of local and global mechanical properties, fracture analysis and micro-mechanisms of fracture. A wide range of analytical techniques were used for these purposes. These included LOM, SEM, TEM, chemical microanalysis (SEM/EDS, TEM/EDS), crystallography (EBSD), X-ray diffraction, thermal analysis (DSC, TGA), infrared spectroscopy (ATR/FT-IR), microhardness and nanohardness. One joining condition was selected for the understanding of the microstructural transformations in the joining parts, which is mentioned later in the Results and Discussion Sections.

In the fifth phase of the work, basic Friction Riveting joining guidelines for future GFRP-emergency bridges were proposed by applying structural calculations and safety factor standards to evaluate joint lap-shear strength. The number of necessary rivets for a bridge structural model was calculated and compared to traditional bolted joints.

Based on the results and knowledge obtained from the various phases of this work, the fundamentals of FricRiveting for continuous fiber reinforced thermoset composite – metal hybrid joints can be set and understood. Figure 4.1 summarizes the main activities of the present work.

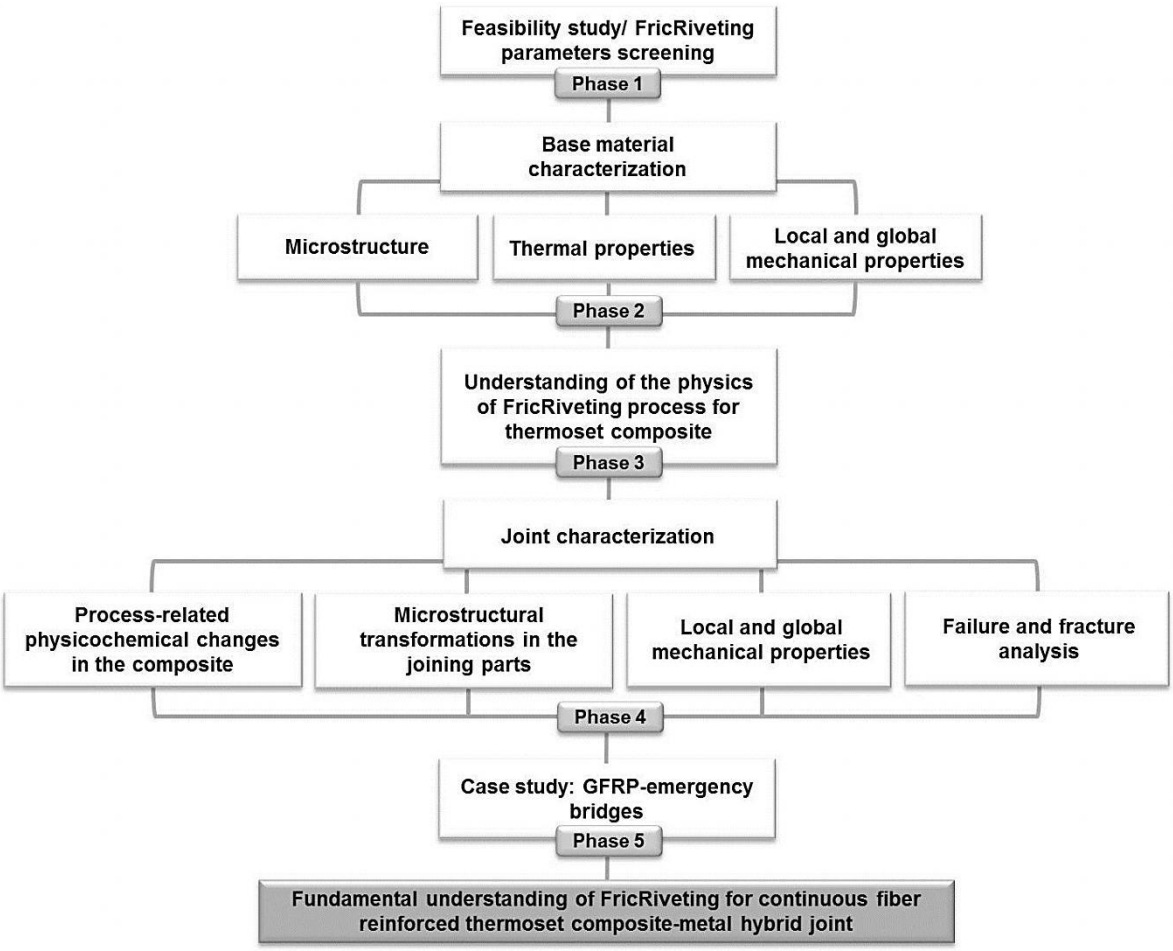

Figure 4. 1 Schematic illustration of the experimental approach.

5 MATERIALS AND METHODS

5.1 Titanium Alloy, Ti-6Al-4V

Extruded rods of Ti-6Al-4V alloy were used for manufacturing rivets of 5 mm in diameter and 60 mm in total length. The chemical composition of the rivets was experimentally determined by flame atomic absorption spectrometry and the result is presented in Table 5.1. This alloy has high specific strength and good corrosion and creep resistances leading to its widely use in bolts/screws for aircrafts and devices for the oil industry [54]. The main properties of this alloy are summarized in Table 5.2. Additional microstructural, thermal and mechanical investigations were performed following the procedures described in Section 5.3. These results were presented separately, in Section 7.

Table 5. 1 Experimental determined chemical composition of Ti-6Al-4V alloy rivets.

Weight (wt. %)	**N**	**H**	**O**	**Fe**	**Al**	**V**	**Ti**
	0.002	0.003	0.107	0.217	6.2	4.5	Bal.

Table 5. 2 Main physical and thermal properties of Ti-6Al-4V alloy [54, 57]**.**

Density (g cm^{-3})	**Hardness (HV)**	**β-*transus* temperature (°C)**	**Solidification temperature range (*Solidus*-*Liquidus*) (°C)**	**Thermal conductivity at about $T_m/2$ (W $m^{-1}K^{-1}$)**	**Thermal diffusivity at about $T_m/2$ (m^2 s^{-1})**	**Coefficient of thermal expansion within 20-650 °C (µm m^{-1} °C^{-1})**
4.43	305-399	995	1604-1660	17.5	6.49×10^{-6}	9.7

5.2 Pultruded Glass Fiber Reinforced Thermoset Polyester Composite

The composite joining part was a 10 mm- thick pultruded glass fiber reinforced thermoset polyester (GF-P) plates. The GF-P supplied by Fiberline Composites A/S, Denmark contains nominally 50 wt.% of E-glass fibers (chemical composition in Annex A) in the stacking sequence of (0º,90º)/(±45º)/(0°,90°). The inhomogeneous distribution of the glass fiber bundles through the plate's thickness leads to anisotropic mechanical behavior.

The polymer matrix of the GF-P is a thermoset polyester cross-linked by styrene monomer [38] with moderate service temperatures between 150°C and 180°C [97]. This composite has very high specific strength (approximately 130 kN.m kg^{-1} and 30 kN.m kg^{-1} at 0° and 90° fiber direction, respectively), easy manufacturing, good chemical resistance and low cost [38]. It contains flame retardants such as antimony trioxide and chlorinated compounds dispersed in the polyester matrix to ensure low inflammability of the composite [78]. Relevant physical, thermal and mechanical properties of GF-P are listed in Table 5.3. Additional mechanical, microstructural and physic-chemical information were investigated through the procedures described in Section 5.3. The results are presented and discussed in Section 7.

Table 5. 3 Main physical, thermal and mechanical properties of GF-P [38].

Density ($g\ cm^{-3}$)	**Tensile strength (MPa)**	**Elongation at rupture (%)**	**Glass transition temperature T_g (°C)**	**Onset decomposition temperature(°C)**	**Thermal conductivity ($W\ m^{-1}K^{-1}$)**	**Coefficient of thermal expansion within 20-650 °C ($\mu m\ m^{-1}°C^{-1}$)**
1.89	240 (0°)/ 50 (90°)	1-2	60-80	390	0.25-0.35	9.0

5.3 Base Material Characterization

The microstructures of the base materials (Ti-6Al-4V rivet and the GF-P composite plate) were assessed by optical microscopy (Leica DM IRM, Germany) and confocal laser microscopy (Keyence VK 9700, Japan). The cross-sections of the rivet and the composite plate were embedded in a low cure temperature epoxy resin and were prepared following standard metallographic procedures (grinding and polishing). Details of the Ti-6Al-4V microstructure and the local chemical composition of the metallic phases and the components of the composite were carried out using the same prepared samples by scanning electron microscopy (FEI Inspect S50, United States) equipped with an energy dispersive spectroscopy (EDS) detector at 25 kV. This device provides a semi-quantitative local chemical analysis in line or trough

map scans and enables the detection of dispersive additives in the composite matrix such as flame retardants in the case of composite and the secondary phase in the Ti-6Al-4V alloy. Complementary, X-ray diffraction was performed through a Siemens D5005 diffractometer to investigate the phase predominance in the metallic rivet. A small specimen (approximately 30 mg) was extracted by cutting the as-received Ti-6Al-4V rivet. The analysis was carried out using Cu Kα radiation at 40kV, 40 mA at rate of $2°min^{-1}$ and range of $30° < 2\theta < 90°$.

Differential scanning calorimetry (DSC), thermogravimetric analysis (TGA) and Fourier transform infrared spectroscopy (FT-IR) were applied to investigate the decomposition, thermal/thermo-mechanical and oxidative degradation of the polyester matrix. DSC was carried out using DSC Q2000 equipment (TA Instruments, United States) in a temperature range of 22-450°C, at heating rate of $10°C\ min^{-1}$ and constant nitrogen flow of 90 mL mm^{-1}. TGA was performed using TGA Q50 equipment (TA Instruments, United States). The analyses were carried out by heating the samples from 22°C to $960^{o}C$ at $10^{o}C$ min^{-1} under constant nitrogen flow of 90 mL mm^{-1}. Samples weighing 7 mg were extracted from three regions through the composite thickness with differences in fiber content and orientation. Figure 5.1-a displays the cross-section of the composite plate and Figure 5.1-b schematically presents the three regions of interest (BM_R1, BM_R2, BM_R3) for microstructural and thermal analyses and infrared spectroscopy.

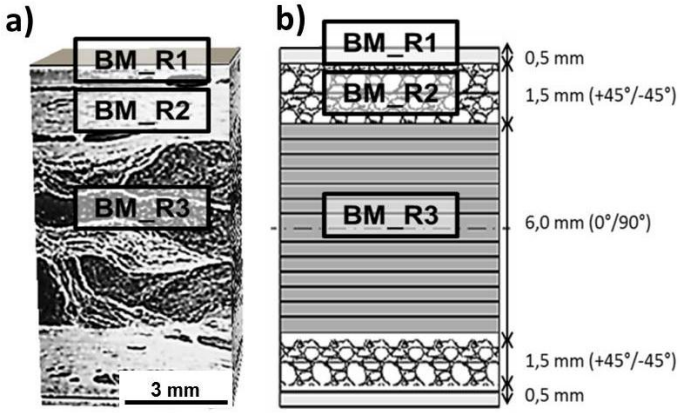

Figure 5. 1 a) Cross-sectional view of the GF-P composite; b) schematic distribution of the glass fiber network through the plate's thickness and the selected regions for material extraction for microstructural and thermal analyses and infrared spectroscopy.

Attenuated total reflection FT-IR (ATR/FT-IR) spectra were obtained using a Varian 640 Fourier transform spectrometer (Varian Inc., United States) with a germanium crystal. Powder samples were extracted by machining the composite from the regions described in Figure 5.1. All spectra were acquired with 256 scans, resolution of 4 cm^{-1} and spectral range of 4000 to 500 cm^{-1}. The glass fiber content over the GF-P plate's thickness was evaluated through the burn-off method, according to the ASTM D3171-99 standard [98]. This method comprises the physical removal of the matrix by ignition, leaving the reinforcement essentially unaffected and, thus, allowing the fiber content calculation. Powder samples (approximately 1 g) were burned-off in a microwave oven (CEM Airwave 7000, United States) at 700°C for 2 h.

DSC was also used to evaluate the onset temperature of β→α transformation - a typical phenomenon in Ti-6Al-4V alloy. Experiments were carried out using Netzsch DSC 404 equipment, heating up to 1100°C at 10°C min^{-1} and constant argon flow of 150 mL mm^{-1}. Samples of approximately 30 mg were extracted by cutting the as-received Ti-6Al-4V rivet. Crucibles of alumina (Al_2O_3) were used.

The global mechanical performance of the metallic rivet was assessed by means of tensile testing based on the ASTM D638 standard [99] using a 100 kN Zwick 1478 universal testing machine (Zwick Roell AG, Germany) with a

crosshead speed of 2 mm min^{-1} at room temperature (21°C). Microhardness maps were used to determine the local mechanical properties of the cross- and longitudinal sections of the metallic rivet. The analysis was carried out using a Zwick/Roell-ZHV machine with an indentation load of HV 0.5 (4.9 N) during holding time of 15 seconds with distance between the indentations of 300μm, following the ASTM E384-10 standard [100]. In the composite, the local mechanical property was assessed by nanohardness testing. For this purpose, a Nanovea nanotester equipped with a Berkowich indenter was used. Measurements were performed with a load of 10 mN, under a loading rate of 30 mN min^{-1} and a holding time of 20 s.

5.4 Friction Riveting Joining Equipment and Procedure

The joints were produced at the Helmholtz Zentrum Geesthacht (HZG), Germany, using a commercially available time-controlled friction-welding system (RSM 400, Harms & Wende GmbH, Germany). The equipment is equipped with a fully automatic and pneumatic operated chuck used to clamp the rivets, as presented in Figure 5.2. The welding system consists of a modular welding head RSM 400 fixed horizontally on aluminum frame, a torque measurement platform with a sample holder for clamping the polymer/composite substrates, along with a switch cabinet and a control panel.

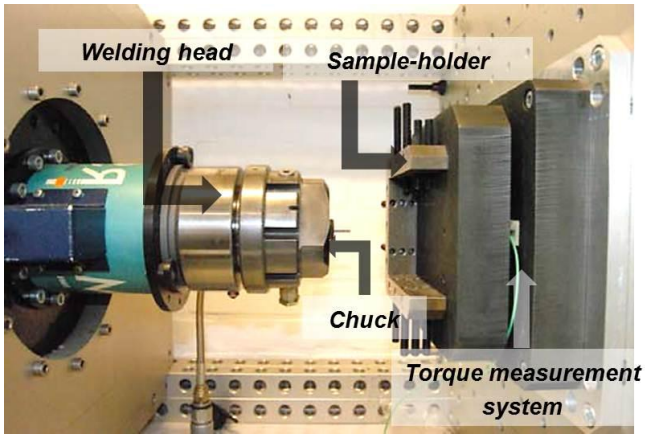

Figure 5. 2 RSM400 welding system used for FricRiveting.

The joining parameters were monitored by the RQ-Fuzzy software (Harms & Wende, Germany), which graphically recorded four analogue variables that could be exported as ASCII-files: rotational speed, joining time, pressure and axial displacement.

A preliminary parameter screening was carried out base in the work from Blaga *et al.* [12] on commercially pure titanium grade 2 (Ti gr. 2) and glass fiber reinforced polyetherimide (GF-PEI). An *one-factor-at-a-time* (OFAT) approach, where each parameter are individually varied while the others are kept constant was designed for this purpose. This feasibility study carried out within the scope of a technical project at HZG is not focus of this work. Therefore, it will not be included in this MSc thesis. The joining parameters range used during this screening phase are shown in Table 5.4.

Table 5. 4 Range of joining parameters used during the parameter screening phase for Ti-6Al-4V/GF-P friction-riveted joints.

Rotational Speed (RS) (rpm)	**Friction Time (FT) (s)**	**Forging Time(FOT) (s)**	**Friction Pressure (FP) (MPa)**	**Forging Pressure (FOP) (MPa)**
9000-1000	0.7-1.2	0.7-1.2	0.6	0.9-1.0

Three joining conditions were selected from the preliminary feasibility study. All joints which provided fairly good ultimate T-Pull tensile forces varying from 1.3 ± 0.3 kN to 4.0 ± 1.2 kN (results not included, not within the scope of this work) with reduced amount of volumetric defects were selected for this work. As previously discussed in [16], RS and FT and their interaction are responsible to control the heat input of Ti-6Al-4V/GF-P friction-riveted joints. Therefore, the joining parameters of the three selected joining conditions C1, C2 and C3 were set to allow different energy inputs during the process. For that, FT was increased from C1 to C2 and RS from C2 to C3, as summarized in Table 5.5. Therefore, energy input increases from C1 to C3.

Table 5. 5 Joining conditions of hybrid Ti-6Al-4V/GF-P joints.

	Rotational Speed (RS) (rpm)	Friction Time (FT) (s)	Forging Time(FOT) (s)	Friction Pressure (FP) (MPa)	Forging Pressure (FOP) (MPa)
C1	9000	1.0	1.2	0.6	1.0
C2	9000	1.2	1.2	0.6	1.0
C3	10000	1.2	1.2	0.6	1.0

5.5 Process Torque and Temperature Monitoring

A force measuring system composed by piezoelectric sensors (model no. 9366AB, Kistler Instruments AG, Germany) was coupled to the joining equipment to record the frictional torque during joining process. The software Dynoware (Kistler Instruments AG, Germany) was used to measure changes in torque signal, which can be directly converted to frictional torque (M_z) at the rivet tip. This measurement provides information regarding the thermomechanical damages in the glass fiber network and in the polymeric matrix of the composite as well as possible process anomalies and equipment malfunction. M_z contributes indirectly to the comprehension of changes in dynamic coefficient of friction during rivet insertion into composite plate. Furthermore, it is a key-issue to understand the physical phenomena involved in the joining phases for complex systems such as the thermosetting composite under investigation.

The frictional torque associated with the rivet rotation and insertion provided also data for the mechanical energy input calculation (see Section 8.1 for the discussion on the analytical energy input model used for Ti-6Al-4V/GF-P joints). Figure 5.3 shows a typical behavior of the time-dependent torque superposed with the rotational speed and joining force curves recorded during the FricRiveting. The area of interest used for the energy input calculation is marked in the figure. Assuming the simplification proposed by Amancio-Filho [39], who considered the frictional phase as the major contribution for the heat generation, the torque curves were integrated from the moment the rivet touches the composite surface (t_0 = 0 s) up to the complete deceleration of the rivet. Moreover, the product between the integrated data [N. m. s] and the

average rotational speed ($\overline{RS}$) [s^{-1}] of the frictional phase was considered the energy input in [J] (Equation 8.1, Section 8.1).

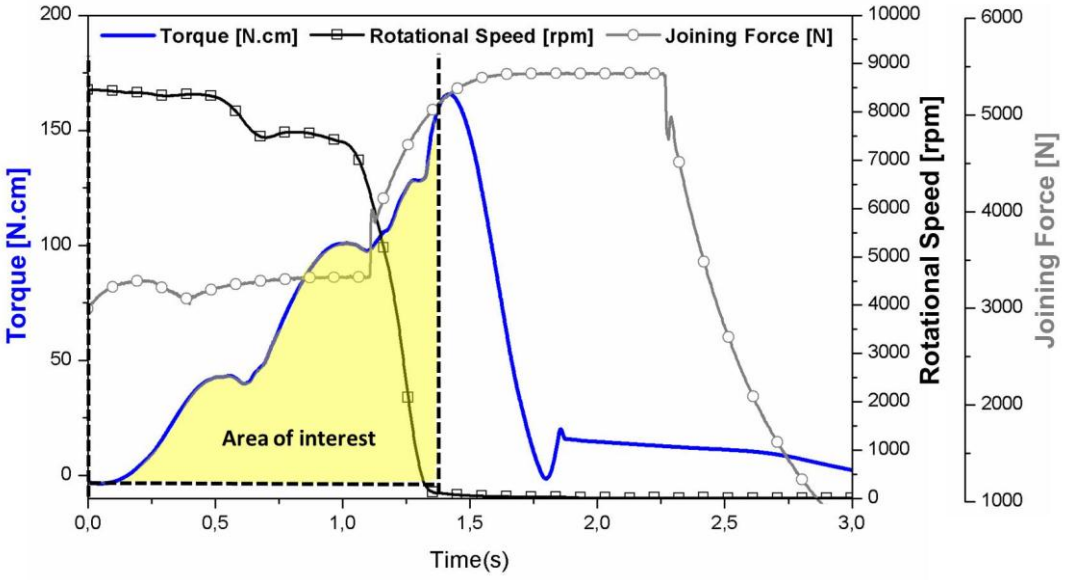

Figure 5. 3 Typical experimental control torque, rotational speed and joining force data for Ti-6Al-4V/GF-P friction-riveted joint including the area of interest for energy input calculation (specimen produced under condition C1: RS = 9000 rpm, FT = 1.0 s and FOT = 1.2 s).

To confirm the assumption that the axial force contribution on the heat generation could be neglected in this work, the axial force component of the energy input was calculated. Results can be founded in Appendix A.

Temperature evolution was recorded on the material expelled from the composite plate (flash) during the rivet drilling action and consolidated around the rivet. Since the composite has low thermal conductivity (Table 5.3), it is assumed that the temperature affecting the flash has almost the same average temperature as the material in contact with the plasticized rivet tip within the composite plate. Similar approach was adopted by Amancio-Filho [11] for AA2024-T3/PEI friction-riveted joints. An infrared thermo-camera system (InfraTec ImageIR®8800, Germany) was used. The camera positioning and measured area are schematically presented in Figure 5.4. The data acquisition rate was set to 20 Hz and the temperature range was calibrated between 300°C and 1300°C. Joining parts were black painted to increase the electromagnetic

radiation absorption of the base materials and, hence, the emissivity of the infrared radiation. The process temperature evolution was used to explain the process-related changes on the microstructure of the joining parts for each joining condition and enable the comparison among them.

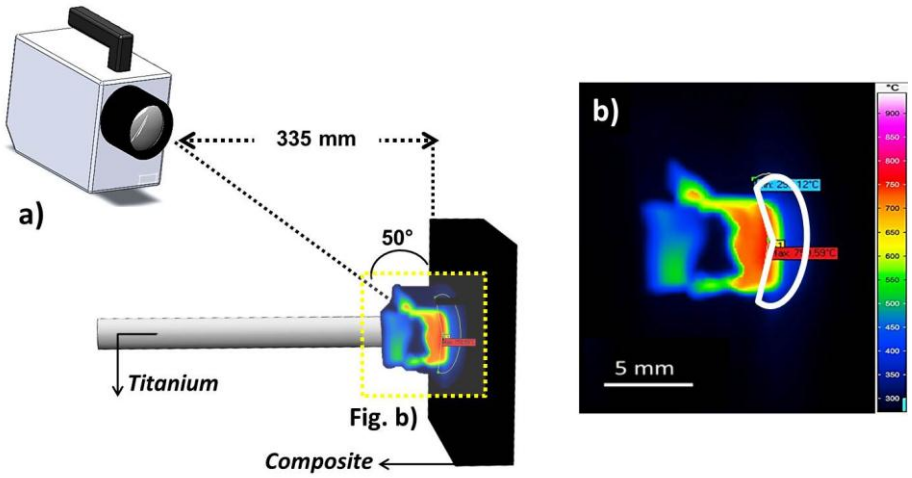

Figure 5. 4 a) IR-camera positioning relative to the sample setting; b) detail of expelled flash material and measured area using during thermography.

5.6 Joint Microstructural Analyses

5.6.1 Optical and Confocal Laser Microscopy

The anchoring zone features of the joints were firstly assessed through light optical microscopy (LOM) under reflective light (Leica DM IRM, Germany) and confocal laser microscopy (Keyence VK9700, Japan). Samples were prepared following the procedure established in Section 5.3. Additionally, chemical etching with Kroll´s reagent (100 mL distilled water, 2 mL hydrofluoric acid, 5 mL nitric acid) was performed at room temperature and exposure time of up to 15 s to reveal microstructural features including grain boundaries, inclusions, cracks, and secondary phases in the metallic rivet.

The optical images allowed the measurement of the rivet tip width (W), the rivet penetration depth (H) and the visual thermo-mechanically affected area (A) in the surroundings of the metallic rivet. For this purpose, the software

Adobe Acrobat 9 Standard was used. W and H provided additional information about the relationship between the joining condition, shape/size of the anchoring zone and the joint mechanical performance, *i.e.* the anchoring efficiency, while A provides an estimate of the process-related thermo-mechanical changes. Figure 5.5 shows a typical Ti-6Al-4V/GF-P friction-riveted joint highlighting the relevant dimensions that were measured.

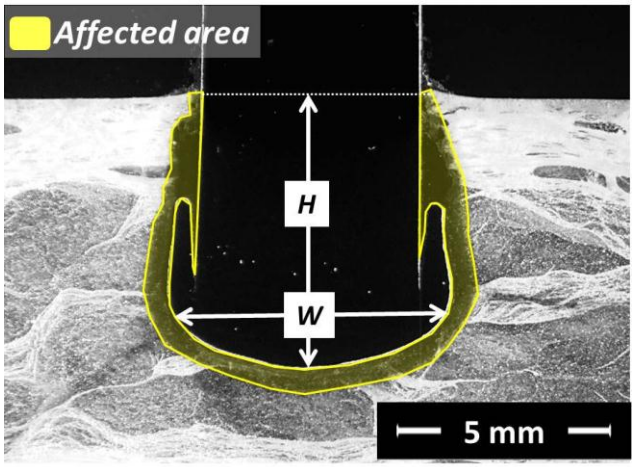

Figure 5. 5 Typical cross-section of Ti-6Al-4V/GF-P friction-riveted joints detailing the relevant dimensions for measurements (joint produced under condition C1: RS = 9000 rpm, FT = 1.0 s and FOT = 1.2 s).

5.6.2 Scanning Electron Microscopy

Scanning Electron Microscopy (SEM) was carried out using thermal emission gun FEI Inspect S50 microscope to investigate different morphologies through the metallic rivet, the quality of the interface between the metal and the composite and the extension of the damage of glass fiber network in the composite owing to the joining process. The cross-sectioned joints were prepared following the standard procedure described in Section 5.3. SEM analysis was performed at 25 kV without chemical etching. Secondary and back scattered electron imaging modes were applied. Furthermore, the local chemical composition of the zones of interest in the joint area was assessed through energy dispersive spectroscopy (EDS).

Additional information was provided by the grain size measurement from zones of interest in the joining area within the metallic part. Since Ti-6Al-4V alloy possibly contains different phase sizes, from prior α and β-grains to α and β-acicular structures, the quantitative investigation of the microstructure is quite complex. Therefore, a simplified approach was selected, based on the ASTM E112 standard [101]. This single-phase procedure measures the grain size and aspect ratio (length, l, as a function of width, w; w/l). The grains were measured from digital SEM images using Image J software.

5.6.3 Transmission Electron Microscopy

Details of α, β and martensitic phases in the rivet anchoring zone were investigated by Transmission Electron Microscopy (TEM) using FEI Tecnai^{TM} G^2 F20 microscope operating at 200 kV and using a double-tilt specimen stage. A sample from the deformed rivet tip was extracted through mechanical cutting, as schematically shown in Figure 5.6. Once the material was extracted, thin foil samples were prepared by grinding down to nearby 0.15 mm thickness and then submitted to twin-jet electro-polishing in a solution of 10 mL of sulphuric acid and 90 mL of methanol. The electro-polishing was carried out using Struers Tenupol-5 device operating at voltage of 15-20 V and temperature of 40°C, as suggested in [102].

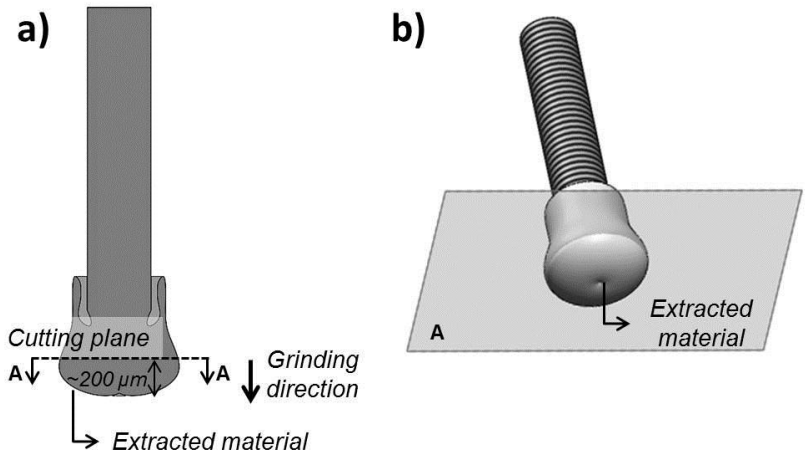

Figure 5. 6 a) Schematic cross-section view of the rivet detailing the grinding direction and the selected region of material extraction for TEM analysis, also represented in (b).

5.6.4 Electron Backscattered Diffraction

Electron Backscattered Diffraction (EBSD) was used to provide better understanding of the process-related microstructural changes in the metallic rivet such as phase transformation, annealing phenomena (dynamic recovery and recrystallization) and texture. The samples were prepared by following the same procedure adopted in Section 5.3 including additional polishing step using colloidal silica slurry. Samples were further electropolished with an electrolyte solution (940 mL acetic acid, 60 mL perchloric acid) using a voltage of 35 V, current of 0.5 A for 5 min at 10°C [103]. The analyses were carried out in a thermal emission gun scanning electron microscope (FEI Inspec S50, United States) operating at 25 kV. The instrument was equipped with a fully automated EBSD device. Data acquisition and post-processing were performed using the software OIM Analysis 6.1. Multiple EBSD maps were acquired using a spatial step size of 0.2 µm and 0.1 µm, depending on the microstructural refinement. The average confidence index (CI) varied between 0.2 and 0.46, depending on the step size and the microstructure. The CI indicates the quality and reliability of EBSD data by the agreement between measured and theoretical interplanar angles and family of planes, a typical fingerprint of a crystal structure [104].

5.7 Phase Identification by X-Ray Diffraction

The general phase identification on the Ti-6Al-4V deformed rivet tip was performed by X-Ray Diffraction (XRD) in Siemens D5005 diffractometer with Cu Kα radiation at 40kV and 40 mA at 2° min^{-1}. The analysis was carried out in a range of 30° < 2θ < 90°. The samples were extracted from the same region as for TEM specimens (Figure 5.6).

5.8 Local Mechanical Properties

Vickers microhardness measurements were carried out in the deformed rivet to support the microstructural characterization. The analytical technique allows precise delimitation of the boundaries between the heat affected zone and thermo-mechanically affected zone. The test provides a fast evaluation of changes in local mechanical properties affected by different processing conditions, heat treatment, and microstructural transformation. Microhardness maps were performed using a Zwick/Roell-ZHV hardness tester by following the same procedure adopted in Section 5.3. Half of the rivet cross-section was measured, assuming symmetry of the rivet.

The precise identification of the process-related physical-chemical changes in the polyester matrix of the composite was carried out by nanohardness analysis, thus eliminating any interference of glass fiber on the real matrix hardness data. Nanohardness analysis was performed using a Nanovea nanotester following the procedure established in Section 5.3. The presence of randomly distributed fibers through the composite plate and volumetric defects made the hardness mapping not possible. Therefore, selected regions of the composite in the joint area were analyzed and presented in Section 10.1.

5.9 Global Mechanical Properties

Global mechanical performance of the joints was assessed by lap shear testing. This was carried out using a Zwick 1478 universal testing machine (Zwick/Roell, Germany) equipped with a load cell of 100 kN at a crosshead speed of 2 mm min^{-1}, at room temperature (21°C). Five replicates for each processing condition described in Table 5.5 were tested and their maximum loads were recorded. Single overlap specimens were prepared based on ASTM D 5961 M-08 standard [105] (Figure 5.7–a). Each single overlap specimen consisted of a Ti-6Al-4V rivet (10 mm of the plain tip and full-threaded M5 length of 30 mm) as shown in Figure 5.7-b. These were pre-riveted into a GF-P plate (Figure 5.7-c). An aluminum plate (AA 2198 alloy) perforated with a through-hole diameter of 5 mm (Figure 5.7-d) was used as a gusset to transfer the load to the joint during the test; this procedure was adopted to simulate the real connections in future structural application, where metallic connectors may be applied to assemble butt joints of composite profiles [43]. The hole edges of the aluminum plate were chamfered at a 45° angle to reduce the stress concentration and provide space to accommodate the produced flash consolidated around the rivet at the composite surface. Finally, the two parts were tightened together using stainless steel nuts and washers. These components increase de compressive area nearby the rivet and provide a uniform load distribution, leading to an improvement in the clamping pressure [25]. Nuts and washers made of stainless steel were selected due to their higher static friction coefficient (μ_e) in contact with aluminum surfaces (gusset; μ_e = 0.35) [105] as well as with Ti-6Al-4V (rivet threads; μ_e = 0.50) [106] in comparison to the friction coefficients imposed by nuts and washers of Ti-6Al-4V(μ_e = 0.34 and μ_e = 0.38, respectively) [106–108]. A clamping torque of 5 N. m was applied using a torque key to tighten the joint with M5-nuts and washers following the procedure described in [48]. This pre-set value was based on previous works in FricRiveting where this parameter was determined by increasing the torque up to the break-loose torque - torque required to loosen the anchored rivet inside the composite base plate [47-48].

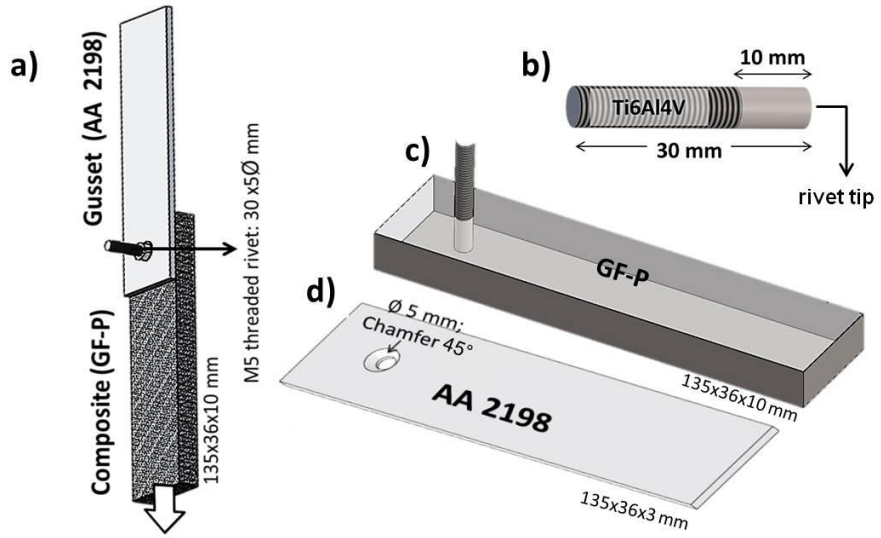

Figure 5. 7 a) Geometry of the single overlap specimen for lap shear testing; b) geometry of the metallic rivet (partially threaded with M5); c) Ti-6Al-4V/GF-P friction-riveted joint and d) gusset plate of aluminum alloy AA 2198.

The geometry of the rivet was chosen based on previous work [49, 109]. As reported, the drilling effect of the thread presented in the rivet tip provides a better insertion of the rivet [49]. However, threads are stress concentration sites in the joining area and can act as a notch for the composite, possibly compromising the mechanical behavior of the composites. Thus, the length of the threaded rivet-section was kept out of the joint area, enabling only the screwing of the rivet nut.

5.10 Fracture Analysis

The fracture surfaces of joints submitted to lap shear testing were preliminary examined by stereo-microscopy (Olympus SZ51/SZ61, Japan). Details of the metallic fracture surface and damage in the composite were evaluated by SEM. A FEI Inspect S50 microscopy was used under secondary electrons operating mode. The correlation between the microstructure of the involved materials and the failure micro-mechanisms was addressed.

5.11 Thermal and Physicochemical Characterization of the Thermoset Polyester Composite

Thermogravimetric analysis (TGA) was performed using TGA Q50 equipment (TA Instruments, United States) to investigate the severity of process-related thermal/thermo-mechanical decomposition of the thermoset polyester matrix in the joined volume of the GF-P composite. Samples of approximately 13 mg were extracted from the flash material expelled during the rivet drilling action. The analyses were carried out by heating the samples from 22°C to 960^{o}C at 10^{o}C min^{-1} under constant nitrogen flow of 90 mL mm^{-1}. The residual mass over temperature was obtained for each run. Differential scanning calorimetry (DSC) was carried out in a DSC Q2000 equipment (TA Instruments, United States). By the analysis of DSC curves, information regarding the polyester degradation as well as the presence and type of flame retardants were obtained based on the measurement of onset temperatures of endothermic phenomena. Due to high volatilization of additives presented in the composite, aluminum hermetic pans and lids were used avoiding the opening of the pans and damages in the furnace. Samples weighing approximately 7 mg were extracted from the flash material deposited in the composite surface and consolidated around the rivet. A temperature range of 22-450°C at a heating rate of 10°C min^{-1} and constant nitrogen flow of 90 mL mm^{-1} were used.

Attenuated total reflection Fourier transformed infrared spectroscopy (ATR/FT-IR) was carried out on a Varian 640 FT-IR spectrometer (Varian Inc., United States) to evaluate the degradation of the GF-P composite by changes of the polyester characteristic absorption bands after the joining process. Extracted powder-like specimens from the flash expelled during the joining was used in a volume that could cover the germanium crystal surface of the ATR device. All spectra were acquired with 256 scans, resolution of 4 cm^{-1} and spectral range of 4000 to 500 cm^{-1}.

6 RESULTS AND DISCUSSION

The results of this MSc work and their respective discussion are divided into five chapters to provide a logical structure and contribute to the understanding of the discussion. Chapter 7 covers the characterization of the base materials. The fundamental understanding of FricRiveting of metal-thermoset composite through energy input, process temperature and torque evolution is discussed in Chapter 8. Chapter 9 deals with the process-related microstructural changes in the joint parts and the physicochemical changes of the composite. The quasi-static mechanical properties of the joints, failure analysis and micro-mechanisms of fracture are discussed in Chapter 10. Finally, in Chapter 11, a case-study of friction-riveted GF-P emergency bridge is presented comparing FricRiveting technology with conventional mechanical fastening.

7 BASE MATERIAL CHARACTERIZATION

The base materials were characterized in terms of microstructure, local and global mechanical properties and thermal behavior. The understanding of these main properties provides a basis for further discussions regarding the mechanical and thermal behaviors of friction-riveted hybrid joints.

7.1 Microstructure

Figure 7.1-a displays the typical microstructure of the longitudinal section of Ti-6Al-4V rivet used in this work. Figure 7.1-b is a TEM bright-field (BF) image showing into details α-Ti and β-Ti phases presented in Ti-6Al-4V along with the indexed selected area electron diffraction (SAED) pattern of α-Ti phase oriented in the $[0001]_{\alpha\text{-Ti}}$ zone axis and β-Ti phase oriented in the $[001]_{\beta\text{-Ti}}$. Figure 7.1-c and d show an inverse pole figure (IPF) map and the phase distribution and content, respectively.

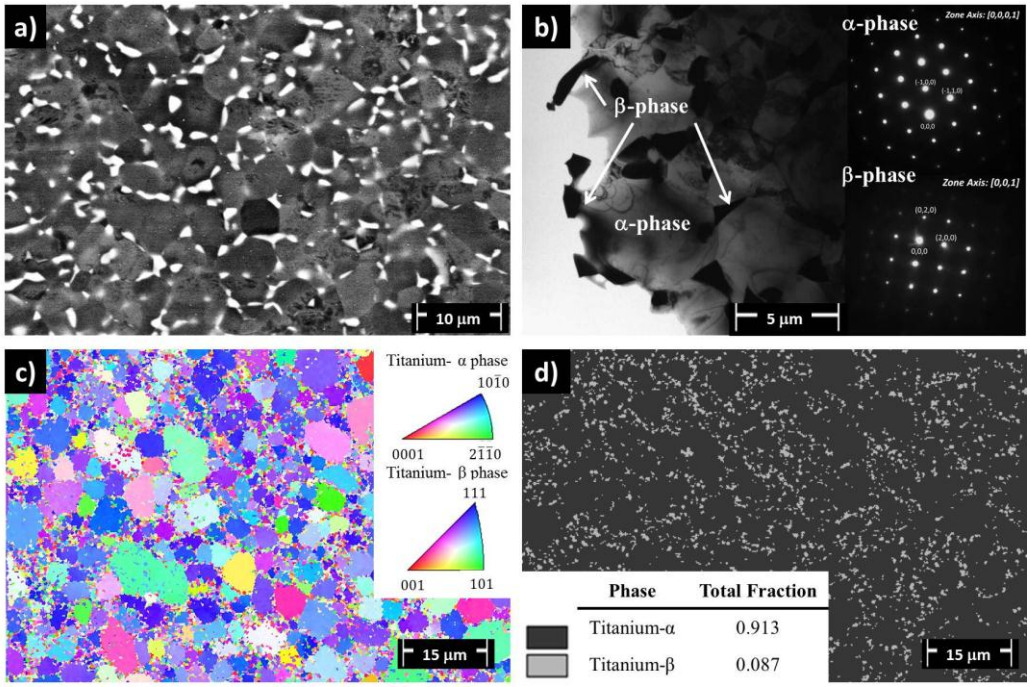

Figure 7.1 a) General overview of the Ti-6Al-4V base material microstructure parallel to the extrusion direction; b) TEM bright field image detailing the α and

β phases with their respective SAED oriented in the $[0001]_{\alpha\text{-}Ti}$ zone axis and $[001]_{\beta\text{-}Ti}$; c) EBSD map showing the crystallographic orientation of the Ti-6Al-4V grains and d) the phases fraction and distribution over Ti-6Al-4V base material.

The microstructure of Ti-6Al-4Valloy comprises two phases with β-Ti (bcc) phase (average width of 0.6 ± 0.1 μm; aspect ratio of 0.4 ± 0.06) distributed in the grain boundaries of equiaxed α-Ti (hcp) phase (average grain size of 4.35 ± 0.75 μm; aspect ratio of 0.94 ± 0.02). The semi-quantitative chemical composition of each phase (α-Ti and β-Ti phases, respectively), determined by energy dispersive X-ray spectroscopy (EDS), can be found in Appendix B. As indicated in Figure 7.1-d, the predominant microstructure is composed by α-phase (91.3%) responsible for the material high strength, while 8.7% is β-phase, which provides good ductility and metal formability. Although the grains are not visually elongated to any preferential direction (Figure 7.1-a), the α-grains seem to be oriented preferentially to the $[10\bar{1}0]$ direction. This observed texture can be attributed to the extrusion process of the rivets [110].

Figure 7.2 presents the microstructure of the pultruded glass-fiber reinforced thermoset polyester (GF-P). As evident in Figure 7.2-a, based on the fiber mat and wave distribution, three regions were identified through the cross-sectional view of the GF-P. These are a cover layer (Region 1) followed by an intermediate zone (Region 2) with glass-fiber (GF) following preferential orientation and Region 3, where the GF are randomly distributed. This inhomogeneous architecture is related to the pultrusion process of the composite, which leads to anisotropic properties as shown in Table 5.3. The presence of scattered small bright particles (black rectangle in Figure 7.2-a and dashed rectangle in magnified picture Figure 7.2-b) was identified by the semi-quantitative chemical analysis (Figure 7.2-c) as antimony presented in an antimony trioxide (Sb_2O_3) flame retardant. Due to the intrinsic high inflammability of polyester matrix, Sb_2O_3 is usually combined with chlorinated compounds to ensure high thermal resistance for this composite [38]; they were detected by the presence of Cl-peak in low concentration in the EDS

spectrogram (Figure 7.2-c), which helps to confirm the presence of Sb_2O_3 in the composite.

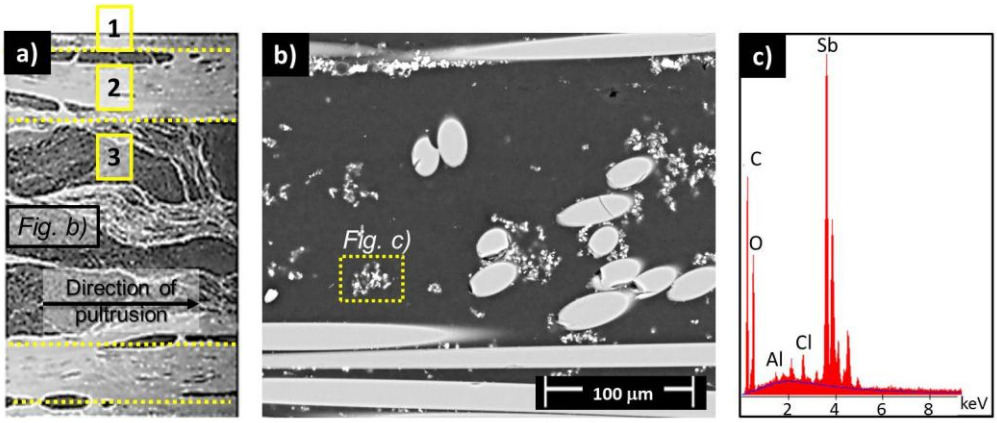

Figure 7.2 a) Cross section of GF-P part, indicating three regions of interest; b) microstructure of composite central part evidencing the inhomogeneous glass fiber distribution and the presence of Sb_2O_3 flame retardant particles and c) the spectrum of semi-quantitative chemical composition of the flame retardant compounds highlighted in (b).

7.2 Thermal Properties

Figure 7.3-a shows typical DSC curve of Ti-6Al-4V alloy while Figure 7.3-b shows the GF-P thermogram. The temperature range at which the base materials were exposed was selected based on the friction-riveting temperatures shown in Section 8.2. Two endothermic peaks at around 870°C and 930°C were observed in the thermogram of Ti-6Al-4V alloy (Figure 7.3-a). These peaks correspond to α-Ti into β-Ti transformation [111]. During the continuous heating of the material, α-Ti dissolved at this temperature range due to the range of grain size and possible different residual phases (secondary α-Ti phase and α-Ti laths) from the rivet manufacturing process or sample preparation (although the cutting of the samples was performed using cutting blade with low rotational speed to avoid temperature increase, the cooling down system could be insufficient and inhomogeneous, favoring phase transformation in the metal). There is no exothermic peak which proves the absence of martensitic structures in the Ti-6Al-4V base material [111].

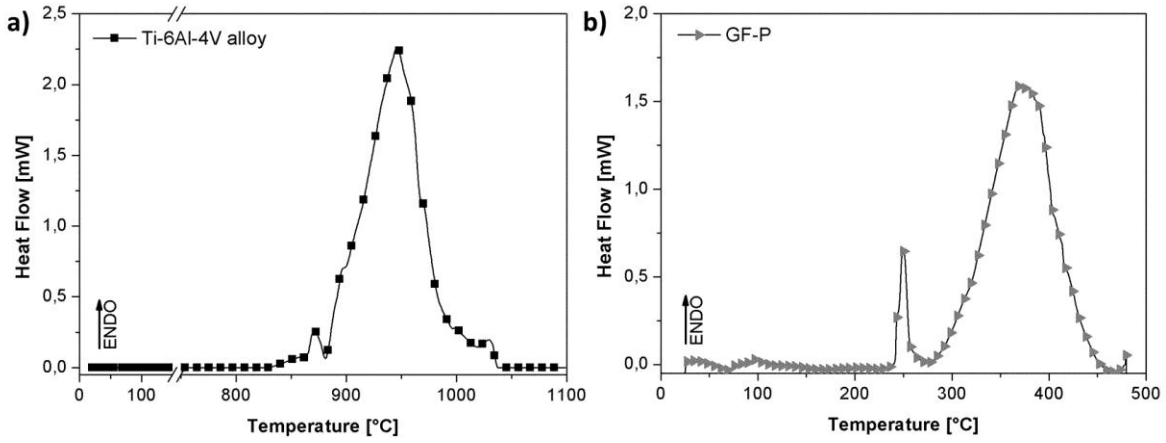

Figure 7.3 Typical DSC curves of a) Ti-6Al-4V and b) GF-P base materials.

The DSC curve of the composite (Figure 7.3-b) presented two endothermic peaks, at around 250°C and 380-390°C. The endothermic peak around 250°C is attributed to the reaction of the Sb_2O_3 with the HCl generated by the decomposition of the chlorinated flame retardant compound [112]. The main product of this chemical reaction is the active specie SbOCl, which initiates a sequence of endothermic reactions generating $SbCl_3$ species, which in turn scavenge hydrogen and hydroxyl chain branching radicals formed from polymer decomposition [112]. Thus, the composite is stabilized against flame propagation. Equation 7.1 shows the physical mechanism of active specie formation and Equation 7.2 the chemical flame retardant reaction between the active specie and the product of halogenate decomposition. The second endothermic peak (380-390ºC) observed in Figure 7.3-b is related to the thermal decomposition of the polyester matrix. The thermo-oxidation of GF-P was not evaluated since the test was performed in a nitrogen atmosphere.

$$
\begin{aligned}
Sb_2O_3 + 2HCl &\xrightarrow{250°C} 2\,SbOCl + H_2O \\
5\,SbOCl &\xrightarrow{245-280°C} Sb_4O_5Cl_2 + SbCl_3 \uparrow \\
4\,Sb_4O_5Cl_2 &\xrightarrow{410-475°C} 5\,Sb_3O_4Cl + SbCl_3 \uparrow \\
3\,Sb_3O_4Cl &\xrightarrow{475-565°C} 4\,Sb_2O_3 + SbCl_3 \uparrow \\
3\,Sb_3O_4Cl &\xrightarrow{475-565°C} 4\,Sb_2O_3 + SbCl_3 \uparrow
\end{aligned}
\qquad (7.1)
$$

$$SbCl_3 + \cdot H \rightarrow HCl + SbCl_2 \quad (7.2)$$

The inhomogeneity of the fiber distribution throughout the thickness of the GF-P composite can affect the dynamic coefficient of friction during the rivet drilling action and, consequently, the heat generation [83]. Similar effect is attributed to the high elastic mechanical response (low viscous response) of the thermoset polyester matrix below its glass transition temperature [83]. Once the composite rheology and the fiber content are related to the heat input, they can be seen as important factors influencing rivet plasticizing and composite thermo-mechanical degradation in FricRiveting. The burn-off method and the thermogravimetric analysis (TGA) were carried out to quantify the GF content in the composite and decomposition behavior. Samples were extracted from the three regions of the GF-P part (BM_R1, BM_R2 and BM_R3, Figure 5.1). Figure 7.4-a and -b show the burn-off data and the thermal decomposition behaviors by TG/DTG curves, respectively.

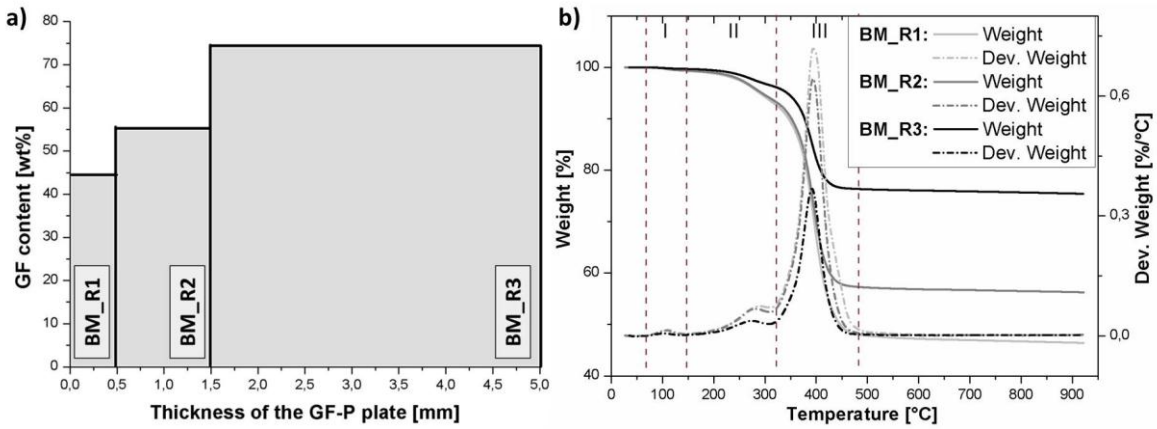

Figure 7.4 a) Fiber content for tree regions of interest (Figure 5.1) in the GF-P base material obtained by burn-off testing; b) TG and DTG curves of GF-P base materials extracted from the three regions of interest in the composite.

Good agreement between burn-off and TGA data was shown in Figure 7.4 for glass fiber content in GF-P part. In the center, region BM_R3, where higher amount of GF (74 wt. %) is presented (Figure 7.4-a), the residual mass at 800°C was 73 ± 1.8 wt. %. Regions R1 and R2, with lower fiber content (43%

and 55%, respectively), presented a residual mass of 43 ± 5 wt. % and 56 ± 0.5 wt. %, respectively. Therefore, the comparison between the burn-off and TGA responses revealed that almost all of the residual mass in TGA is composed of GF. Additionally, as observed in Figure 7.4-b, the material from R3 had better thermal resistance, shifting the curve to higher decomposition temperatures. The good thermal stability of the GF at evaluated temperature and the increase of the physical barrier – which restrains the polymeric molecular diffusion – imposed by the high fiber content in R3 possibly led to a general better composite thermal resistance in this region [6].

Three thermal decomposition steps were identified for GF-P according to DTG curves in Figure 7.4-b and consistent with the literature [84]. The first Step (I), at 103-110°C, with residual mass of 99 wt. %, is assign to the evolution of structural water [113]. The second Step (II), at 275-295°C, with residual mass varying between 95 wt. % and 97 wt. %, for the surface (R1) and the central regions (R3), respectively, is attributed to the random chain scission which is the primary degradation mechanism of the polyester [86]. The decomposition leads to the generation of free radicals and volatilization of CO, CO_2 and styrene [86]. These gases can be entrapped in the fiber/matrix interface damaging the composite by crack initiation/propagation. The third decomposition Step (III) at 390-394^{o}C exhibited mass losses varying between 62 wt. % for R1 and 30 wt. % for R3. This final stage corresponds to the decomposition of the remaining products from the second step [84]. In order to improve the accuracy of these results, further analysis such as pyrolysis-gas chromatography should be performed. Moreover, the chemical structure of GF-P analyzed by Fourier-transform infrared spectrometry can provide additional information to the discussion and was already investigated by Borba *et al*. However, deeper investigations on the topic are not in the scope of the present work and were not included.

7.3 Local and Global Mechanical Properties

The local mechanical performance of the Ti-6Al-4V rivet was determined using microhardness analysis while the nanohardness analysis was used for the composite investigation. Figure 7.5 presents Vickers-microhardness distribution through the rivet cross-sectional (a) and longitudinal (b) views. The calculated average microhardness was 321 ± 12 HV with hardeness increasing from the center to the surface of the rivet. This profile is typical for extruded rod due to the higher strain rates experienced by the surface in contact with the die.

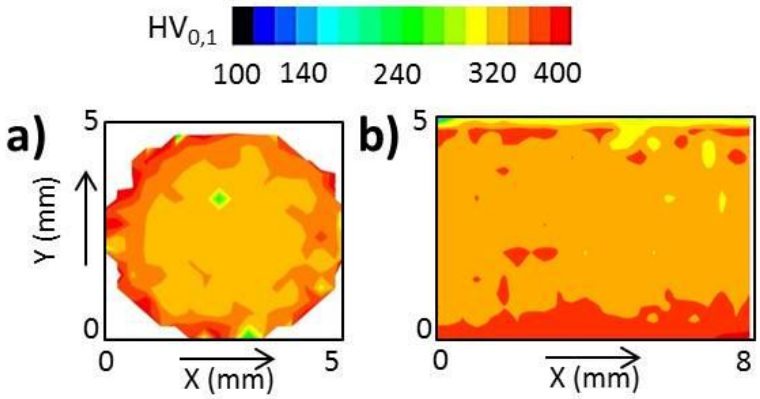

Figure 7.5 Vickers microhardness map of the Ti-6Al-4V rivet; a) cross section and b) longitudinal section.

Figure 7.6 shows hardness values of each component of GF-P composite determined by nanohardness analysis. The average hardness for the polyester matrix was 23 ± 2 HV while for the GF was 479.0 ± 7.2 HV.

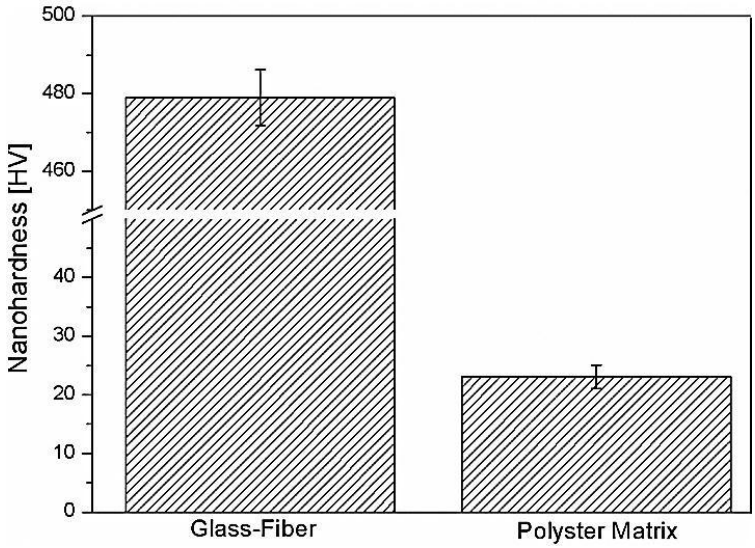

Figure 7.6 Average nanohardness of the glass fiber and the polyester matrix of GF-P base material.

In order to determine the global mechanical property of the Ti-6Al-4V, three rivet replicates were tested under tension following the procedure described in Section 5.3. Figure 7.7-a shows the experimental force-displacement data for the replicates along with the average force-displacement curve for Ti-6Al-4V rivet. The average ultimate tensile strength (UTS) was 910 ± 1 MPa, corresponding to an ultimate tensile force of 36 ± 0.05 kN and strain at rupture of 17 ± 0.4 %. The failure was predominant ductile with the typical “cup-and-cone” plastic deformation pattern (Figure 7.7-b). Matthew and Donachie [56] discussed the dependence of the mechanical properties of this titanium alloy to its microstructural features. Comparing to the fully lamellar microstructure where the UTS is 1145 MPa and the strain at rupture is 5% [54], the tensile ductility of this alloy with fully equiaxed microstructure was very high. In this case, the slipping length is larger than the alpha grain size, due to strong crystallographic textures generally experienced by processed/deformed titanium in (α+β) phase field [54].

GF-P base material tensile properties were provided by the supplier and not tested within the scope of this work, due to the complex machining preparation of tensile specimens.

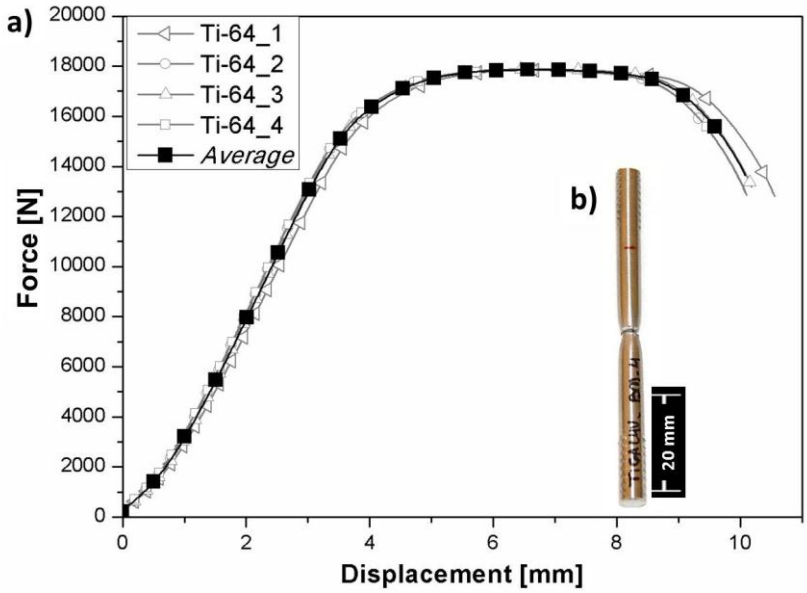

Figure 7.7 a) Mechanical performance of the Ti-6Al-4V base material under tensile testing; b) typical “cup-and-cone” fracture of Ti-6Al-4V tensile test specimen.

8 FUNDAMENTAL UNDERSTANDING OF FRICRIVETING PHYSICS FOR METAL-THERMOSET COMPOSITE

Figure 8. 1 depicts the surface view of three selected joining conditions and their respective frictional energy (E_{fr}) calculated based on the integration of the torque measurement, as described in Section 5.5. This energy is usually considered analogous to the energy input in friction-based welding and joining processes [114]. As it can be seen in the figure, by increasing the energy input, the amount of powder-like and agglomerated flash material, displaced to the surface of the joints and attached to the rivet (marked with dashed circles in Figure 8. 1), were considerable higher. Details of the heat input evaluation will be presented in the followed Section 8.1.

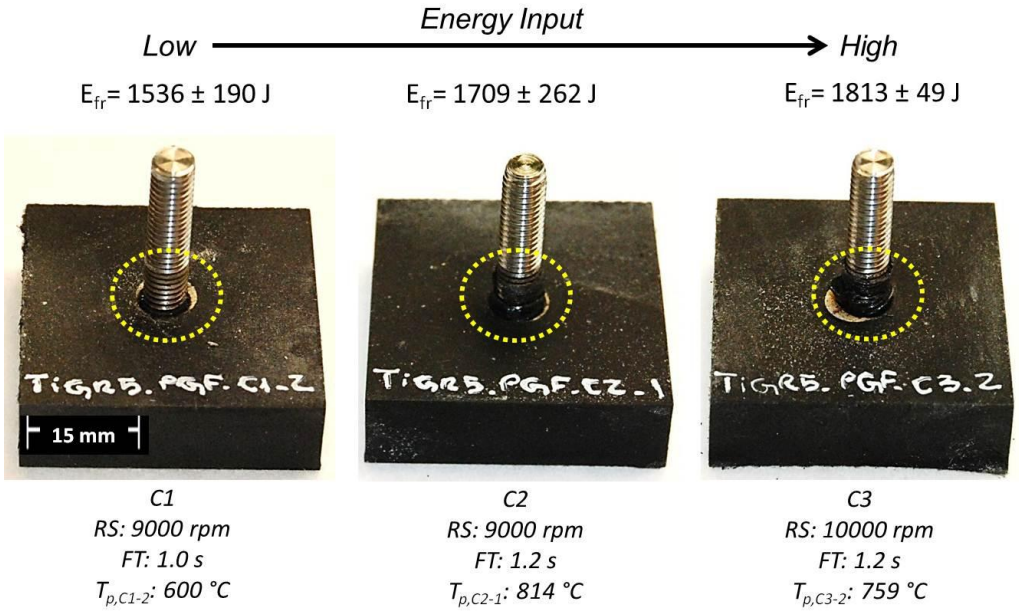

Figure 8. 1 Surface photographs of the Ti-6Al-4V/GF-P case-study joints along with their calculated average energy input values.

8.1 Heat Input Evaluation

It is well known that the low viscous regime of thermosetting polymers above the glass transition temperature compromises the features of the material by severe thermal/thermo-mechanical degradation [112]. Therefore, for friction-based joining processes of GF-P, the effect of the heat and plastic deformation

must be investigated. For this purpose, a simple model of energy input (Equation 8.1) proposed by Neumann [114] for friction welding of metals was selected for this work. This approach well describes, for instance, the effect of parameters such as rotational speed on the heat generation in friction welding/joining of metals, unreinforced and fiber-reinforced thermoplastics [42-43, 115–118].

$$E_{total} = E_{fr} + E_{ax} = \int M_z \times \omega \, dt + \int F \times \upsilon_0 \, dt \; [J] \quad (8.1)$$

E_{total} is the energy generated by the mechanical work of the tool or, for the case of FricRiveting, the rivet and has two contributions. The frictional contribution (E_{fr}) is dependent on the frictional torque, M_z (N m) and angular velocity / rotational speed, ω (rad s^{-1}). The axial force contribution (E_{ax}) is the integration of the product between the axial force, F (N) and burn-off rate, υ_0 (m s^{-1}).

Based on this method, Amancio-Filho *et.al* [11] proposed an analytical model for heat generation during the FricRiveting of hybrid thermoplastic-metal joints. His calculation considers the axial and frictional contributions as well as the viscous and solid (Coulomb) heating. The feasibility of this model was demonstrated for joints of AA2024T3/PEI and detailed in [39]. The authors have demonstrated that the axial contribution plays a minor hole on the heat input [39]. However, this mathematical heat input modeling is not directly applicable for hybrid thermosetting composite-metal joints since no changes in the composite viscosity are observed over the material heating phase. It is expected that the major contribution during the heating phase may be related to the solid state friction between the metal, the glass fibers and the thermoset matrix.

Currently there are no models available for thermoset composites. The energy input calculated by Equation 8.1 provides a good estimation of heat generation and was applied in this investigation (see results in Appendix A). The axial force contribution to the energy input of Ti-6Al-4V/GF-P C1 joints was 207 ± 23 J while of C2 and C3 joints were 191 ± 49 J and 224 ± 22 J,

respectively, laying in average between 11 to 13% of the total energy input. In comparison to previous work in FricRiveting of fiber reinforced thermoplastic where this contribution to the mechanical energy input was about twenty times lower than the frictional contribution [13], in the case of fiber reinforced thermoset, the second component of Equation 8.1 is significant and could not be disregarded for simplification, as suggested in the literature [39]. Therefore, the average of total energy input for the case-study joints included E_{fr} and E_{ax} and the results were: $E_{total,C1}$= 1743 J, $E_{total,C2}$= 1900 J and $E_{total,C3}$= 2067 J.

8.2 Process Temperature Evolution

The process temperature was measured by infrared thermography on the flash material expelled from the joining area during the rivet insertion (Section 5.5). Figure 8. 2 displays the typical temperature data over time for examples from one replicate joint of each joining condition along with important transformation temperatures of the base materials. The average peak temperature achieved for each joining condition and joint heating and cooling rates are summarized in Table 8.1.

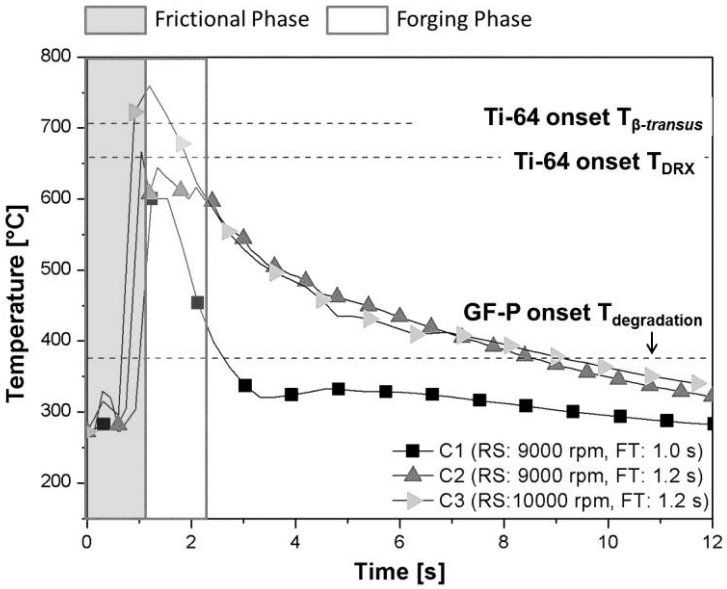

Figure 8. 2 Process temperature evolution measured by infrared thermography and the comparison with important transformation temperatures of the base materials.

The curves in Figure 8. 2 show that peak temperature is achieved at around one second in the frictional phase (light-gray rectangle). By reaching this temperature, the cooling initiated under pressure, during the forging phase (white square). Furthermore, the figure indicates that by increasing frictional contributions of the energy input equation (Equation 8.1), *i.e.* RS and FT, the peak temperature raised, from 460 ± 130°C (C1, E_{total} = 1743 J) to 761 ± 2°C (C3, E_{total} = 2067 J). The visual quantification of the amount of flash formed during the process is in accordance to the variation of the temperature. The higher the temperature, the larger the amount of flash generated (see Figure 8. 1) and easier was the measurement of the temperature with the IR-camera. This can explain the decreasing in the standard deviation for the average maximum temperature from C1 to C3.

It was shown that Ti-6Al-4V alloy and GF-P presented low thermal conductivity (Table 5.2 and Table 5.3, respectively) favoring slower cooling rates. However, the inhomogeneity of the fiber content and distribution through the composite thickness, owing to the pultrusion manufacturing process of the GF-P, causes an inhomogeneous heat distribution though the joints, increasing the complexity of the results analyses. The temperatures increased through similar heating rates (Table 8.1) confirmed by the parallelism among the onset of the curves while decreased over different cooling rates exhibiting noticeable distinct cooling paths. Joints from condition C1 revealed a sharp cooling (178 ± 15 °C s^{-1}) while from C2 (59 ± 15 °C s^{-1}) and C3 (45 ± 4 °C s^{-1}) cooled slower (smaller curve slopes). This is because lower heat generation yields faster cooling rates.

Table 8. 1 Process temperatures and cooling rates of Ti-6Al-4V/GF-P specimens, correlated with FricRiveting joining conditions.

	C1	**C2**	**C3**
Average Peak Temperature (°C)	460 ± 130	758 ± 56	761 ± 2
Heating Rate (°C s^{-1})	376 ± 116	473 ± 104	403 ± 21
Cooling Rate (°C s^{-1})	178 ± 15	59 ± 15	45 ± 4

Invariably, the recorded temperatures were well above the experimentally determined- onset decomposition temperature of GF-P (390°C). Thereby, the thermo-mechanical degradation of the composite took place in the joining area introducing volumetric defects to the surrounds and underneath the deformed rivet as will be shown in details in Section 9.4. The extension of the degradation varied depending on the joining condition and will be reported in Section 9.1. Besides, due to large deviation related to the difficulty of measuring temperature in the expelled, powder-like flash material, the real process temperatures may have achieved the glass fiber softening (830-920°C) [77] and melting (1065-1200°C) [77] temperatures. This hypothesis was confirmed through microstructural evidences, reported into details in Section 9.4, which showed the consolidation of softened/molten glass layer in the interface between metal and composite. The effects of the fiber reinforcement physical changes on the joint formation are still unexplored and will be deeply discussed in Section 9.3.

The temperatures raised up to 28-46% of the Ti-6Al-4V alloy melting point (1665°C) and ranged nearby its hot-rolling temperature (860-980°C), dynamic recrystallization (660-825°C) and the β-*transus* temperature [119]. As reported by Kitamura *et. al* [50], in friction-based processes of Ti-6Al-4V alloy characterized by severe conditions of deformation, such as *Friction Stir Welding* (FSW), a non-equilibrium β-*transus* temperature is established at values lower than 949°C. Other authors reported temperature range even lower, in which the end of the β-to-α transformation is found to lie between 670-690°C for cooling rates of 50-10 °C/min [120-121]. In FricRiveting a similar decrement in the onset β-*transus* temperature is expected. Facing the process-related large deformation and the heat generation, the required energy to reach the necessary enthalpy to transform β-Ti phase into α-Ti phase is expected reduced favoring decrease of the onset β-*transus* temperature [50]. Evidence confirmed by microstructural analysis to be discussed in Section 9.2 helps to support this assumption. However, this hypothesis should be confirmed by a complementary analytical method such as differential scanning calorimetry (DSC); this investigation was out of the scope of this work.

In α + β titanium alloys, the effects of process temperature and cooling rate on the microstructure are significant, providing different phases morphologies such as lamellar and equiaxed [54]. According to Ahmed and Rack [102], a Continuous Cooling Transformation (CCT) diagram provides a valuable information into the probability of different phases morphologies formation in Ti-6Al-4V alloy. The authors have shown that in order to attain a range of microstructures, the material has to experience different values of cooling rates [102]. Thereby, the cooling rates calculated for friction-riveted joints were compared to the literature, as shown in Figure 8. 3.

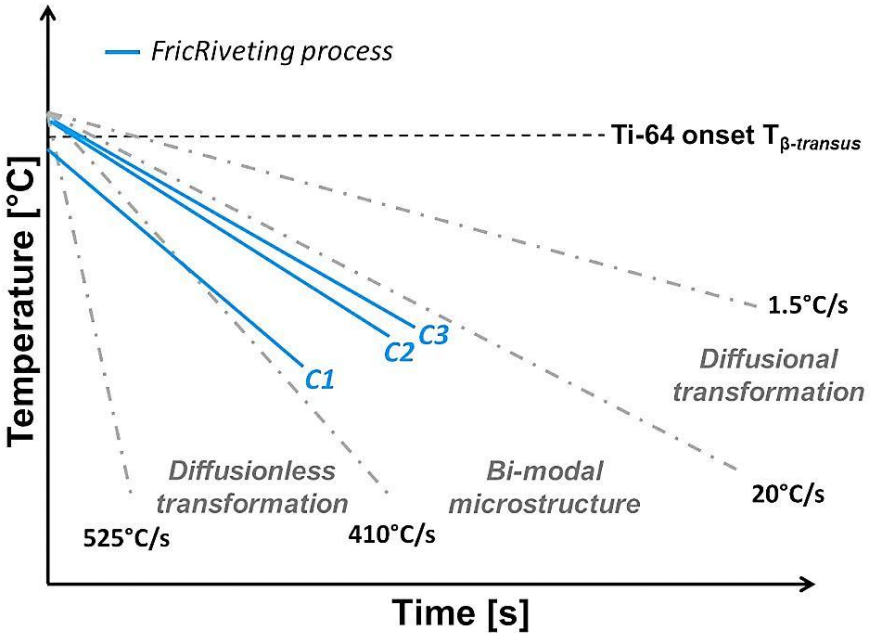

Figure 8. 3 Schematic continuous cooling diagram for Ti-6Al-4V alloy. The measured cooling rates associated with the FricRiveting process are indicated (Adapted from [67]).

Considering the peak temperatures below the β-*transus* temperature for C1 and nearby for C2 and C3, the calculated cooling rates lied in a bi-modal microstructure field suggesting the presence of equiaxed grains combined with acicular structures. These acicular structures can be resultant of either diffusionless transformation (metastable α' martensitic structure) or/and diffusion transformation (Widmanstätten structure) [122]. Therefore, one may

expect changes in the microstructure of the rivet. The detailed metallurgical transformations will be discussed in Section 9.2.

8.3 Frictional Torque Evolution

Regarding friction-based joining process of thermoplastic and its composites, the torque (Mz) provides information of the material viscosity and, therefore, its capacity to flow into cavities and promote mechanical anchoring [41]. However, for thermosetting composites which, in principle, do not have viscous regime above the polyester glass transition temperature (T_g ~80°C), this parameter contributes to the understanding of the joint formation through the influence of the fiber reinforcement and the damage of the matrix. A typical average curve of frictional torque is presented in Figure 8. 4. In general, during the insertion of the metallic rivet, M_z increased up to a maximum in the forging phase, followed by a sharp decay, tending to zero when rotation speed is completely stopped. From the figure one may observed that an unstable torque regime was established over frictional phase, characterized by sequential slopes in the curve.

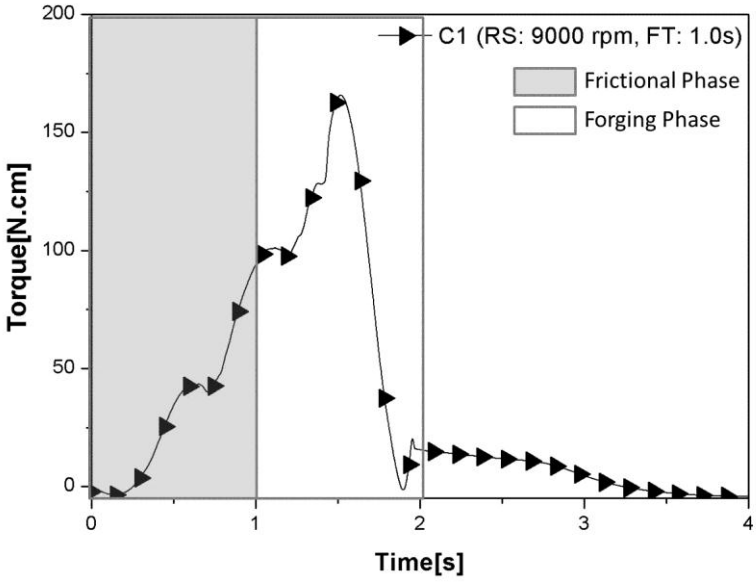

Figure 8. 4 Example of frictional torque-time curve for a typical Ti-6Al-4V/GF-P joint (condition C1: RS = 9000 rpm, FT = 1.0 s and FOT = 1.2 s).

The pultrusion process-related fiber architecture of the GF-P part seems to play an important role in the torque evolution. Each fiber bundle appears to work as a physical barrier for the rivet drilling action, causing drastic damage through breaking fibers; it may explain the step-wise increase in torque. Moreover, the abrasive particles (mainly glass broken fiber) generated from this process contributes to increase dynamic friction coefficient and consequently, the frictional torque (Figure 8. 4) [83].

Once the dynamic friction coefficient increases, heat is also generated, increasing the temperature and thermally/thermo-mechanically affecting the matrix and the GF reinforcement. For such high reached temperatures, as already shown in Figure 8. 2, the matrix is degraded and most of the products of this reaction are volatilized, while the glass fibers and broken-down glass fibers are softened or molten. In this case, the decrease in viscosity associated to the glass fiber material may explain the slight drop after each peak observed in Figure 8. 4. Additionally, it is believed that this molten glass quickly cools down and consolidates on the rivet surface acting as a lubricant, up to the moment when the rivet encounters another fiber bundle and the M_z increases again. Microstructural characterization indicates the presence of a glass interphase between the metal and the composite and cracks in this region resultant of differential thermal shrinkage between colder and hotter glass fronts, which support this assumption. These results will be addressed into details in Section 9.2. Therefore, the heat generation regime in FricRiveting of metal-thermosetting composite may be interpreted as a combination of abrasive (which increases the torque) and adhesive (which decreases the torque) wear mechanisms, as described for fiber reinforced thermosets under frictional regime in [123].

The torque-process temperature dependence of Ti-6Al-4V/GF-P friction-riveted joints is shown in Figure 8.5. By increasing the energy input and consequently, the temperature, the contribution of the glass melt viscosity as well as the lubricant effect of the glass interphase became relevant to the torque decrement. The same behavior was evidenced for FricRiveting of metal-

thermoplastic in which increasing the shear rate led to the reduction of melt viscosity of the polymer and, consequently, frictional torque [39].

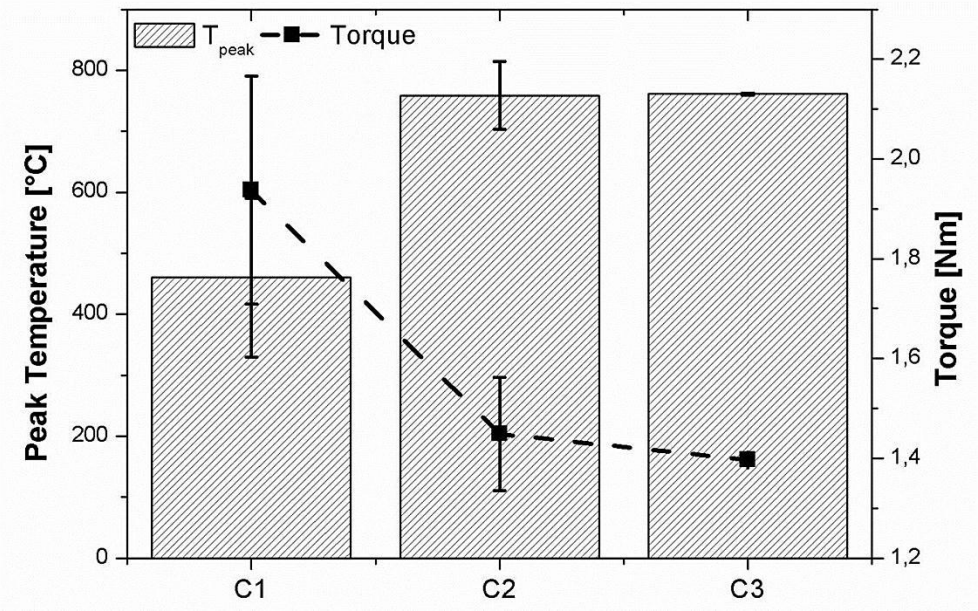

Figure 8. 5 Torque-process temperature dependence of the Ti-6Al-4V/GF-P case-study joints.

9 MICROSTRUCTURAL CHARACTERIZATION OF THE JOINTS

9.1 General Characteristics of the Joints

The process-related transformations in the metal and composite were investigated through optical and electron microscopy. The macro and microscopic thermo-mechanical phenomena occurring in both materials are essential to understand the anchoring of the rivet into the composite, the adhesion established in the metal-composite interface and the extent of the microstructural changes. The extension of the defects in the joining area was also assessed by qualitative (broken fibers, volumetric flaws and metallic splitters) and quantitative (visual thermo-mechanically affected area (A) in the composite) analyses. Figure 9.1 shows typical cross-sectional views of the samples studied in this work. The process temperature (T_p) achieved for each replicate was addressed as well. The rivet 'leg' formation, rivet penetration depth (H) and tip width (W) were indicated in each macrograph.

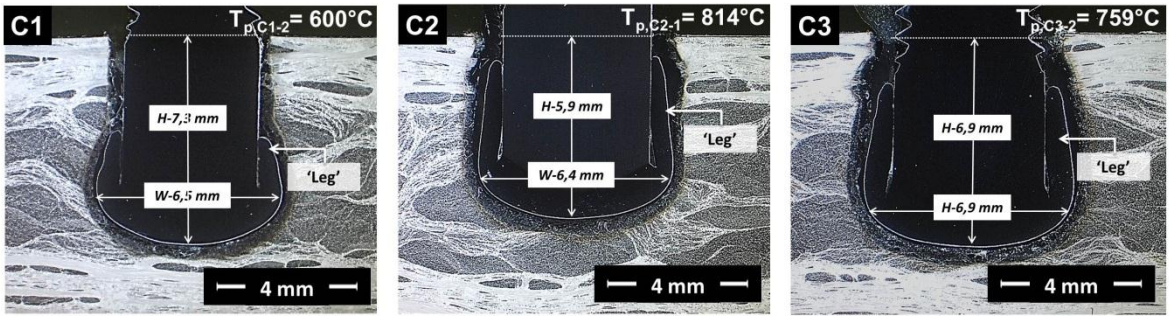

Figure 9. 1 LOM-micrographs of joint cross sections from the joining conditions investigated. H-values are related to the rivet penetration depth and W-values to the tip widening. The rivet plastic-deformation patterns are indicated as 'legs'.

Firstly, macro features of these cross-sectional views were measured in terms of: rivet-tip widening (W), rivet penetration depth (H) and visual composite thermo-mechanically affected area (A). As outlined by Amancio-Filho *et al.* [116], the deformed rivet tip plays an important role in the mechanical anchoring of the rivet and hence the tensile strength of the friction-riveted joints.

Therefore, these dimensions must be studied. Table 9.1 summarizes W, H and A data for the case-study joints.

Table 9. 1 Dimensions of the joint geometry and the visual thermo-mechanically affect area of the composite of Ti-6Al-4V/GF-P friction-riveted joints.

	C1	**C2**	**C3**
H (mm)	8.2 ± 0.7	6.3 ± 0.3	7.1 ± 0.4
W (mm)	6.8 ± 0.2	6.5 ± 0.2	6.5 ± 0.8
A (mm^2)	14.0 ± 3.3	9.5 ± 1.0	13.9 ± 0.5

From the table, at low energy input (C1), joints achieved the highest penetration depth (8.16 ± 0.7 mm), deformation width (6.83 ± 0.7 mm) and highest extension of the visual affected area (14.01 ± 3.3 mm^2). In this case, as presented in Figure 8.2, the process temperature (460 ± 130°C) was significantly below the range of the metal hot-rolling temperature (860-980°C). Thus, the metal formability was less pronounced, forming short 'legs' around the rivet in comparison to C2 and C3 joints (Figure 9.1). Additionally, the process temperature was superior to the composite decomposition range (approximately 390°C) but bellow the glass fiber softening/melting range (830-1200°C) (Figure 8.2). Therefore, besides the expected decomposition of the composite matrix, the friction between the metal-composite surfaces probably mechanically damaged the fibers in a more intense manner, as fibers were probably not able to soften/melt. This favored the rivet drilling action, increase in A and highest frictional torque of C1 in Figure 8.5.

By increasing the energy input (C2 and C3), the visual decomposition and mechanical damage of the composite also occurred but less intense, as presented in Table 9.1. Moreover, smaller H and W values were observed. In these cases, due to high process-temperatures (T_{C2}= 758 ± 56°C, T_{C3}= 761 ± 2°C), the decrease of glass reinforcement viscosity followed by its re-consolidation at the metallic surface is expected to have occurred, evidenced by the decrease in frictional torque for C2 and C3 (Figure 8.5). Thus, the glass interphase formed between the metal and composite seems to facilitate heat dissipation, helping to release the frictional heat by increasing the heat outflow

rate to the rivet. This may happen since the thermal conductivity of the glass material increases with temperature [124]. Thus, smaller area (or volume) of composite matrix was visually affected in C2 (9.5 ± 1.0 mm^2) while in C3 with higher energy input (1813 ± 49 J) and temperature (761 ± 2°C), the affected area were larger (13.9 ± 0.5 mm^2). Furthermore, the lubricant effect of the softened glass layer also appears to reduce the fibers brakeage, visually reducing the damaged area and frictional torque (Figure 8.5).

Additionally, the process temperatures for C2 and C3 were close to plasticizing temperature range of Ti-6Al-4V alloy (Section 8.2). Therefore, during the forging phase, higher ductility, *i.e.* higher formability of the rivet tip will be achieved; the plasticized rivet tip will encounter unaffected composite base material, supporting the upward material flow of the plasticized metal, in the direction of the composite surface. The visual result is the pronounced 'leg' shaping observed in the cross-sectional view of the C2 and C3 joints (Figure 9. 1-b and -c).

In this way, high level of energy input provides changes in the rheological behavior of the glass fiber and an increase of the plasticized-metal volume. The visual composite decomposition extension is not dependent on the energy input at high process-temperatures. Although the macro-analysis evidenced these trends, the microstructures of the joint components can reveal additional information regarding metallurgical and physical-chemical transformations. Thus, the following sub-sections involve all the microanalyses of the materials in the joining area.

9.2 Metallurgical Transformations

One replicate of Ti-6Al-4V/GF-P joints produced by C2 joining condition, with intermediate energy input, was investigated and discussed in this section. The typical microstructures of the regions of interest (1-4) over the cross-section of the joint were detailed by SEM analysis and shown in Figure 9.2-a. Average grain size measurement is presented in Table 9.2. The Region 1, which is located distant from the metallic anchoring zone (Figure 9.2-b) is fully

composed of equiaxed primary alpha phase (α-Ti phase) with average grain size of 5.4 ± 1.2 µm. Elongated beta phase (β-Ti phase) is located in the α-grain boundaries (examples marked with black arrows) with the grain width of 0.8 ± 0.2 µm and an aspect ratio of 0.4 ± 0.1 (Table 9.2). This phase morphology was similar to the morphologies presented in the as-received metallic rivet (Figure 7.1). However, the larger average grain size in Region 1 in comparison to base material (α-grain: 4.5 ± 0.95 µm, β-grain: 0.6 ± 0.1 µm) indicates that this region was thermally affected. The grain growth is a diffusional process, *i.e.* dependent of temperature and time, which happens through solute portioning in the α-Ti and β-Ti phases [125]. Therefore, additional energy added through the process temperature and exposure times is the driving force for the observed grain growth.

Region 2 (Figure 9.2-c) is a transition area, where the rivet experienced less severe thermal processing- probably below the β-*transus* temperature-, cooling and shear rates in comparison to the rivet tip (Regions 3 and 4). The microstructure there comprised a mixture of imminent acicular structures and prior β-grains (protruding structures indicated by white arrows in Figure 9.2-c in the boundary of α-grains). In Regions 3 and 4 (Figure 9.2-d and -e), the grain morphology was transformed into a new microstructure dominated by acicular grains. Grain refinement was evidenced from Region 3 (0.5 ± 0.1 µm) to Region 4 (0.3 ± 0.06 µm) where the acicular structures presented narrower α-grains in comparison to the equiaxed α-grains o base material (4.5 ± 0.9 µm). Region 3 presented higher aspect ratios (0.09 ± 0.02) than Region 4 (0.04 ± 0.01) (Table 9.2). These regions are located in the metallic anchoring zone, which experienced high strain rates and temperatures. As above-mentioned, the temperatures, in this case, probably exceeded the non-equilibrium β-*transus* temperature. The cooling rates appeared to be inhomogeneous, whereas the cooling regime affects considerably the lamellar α-β size, as reported in [67]. For instance, in *Friction Stir Welding* (FSW) of Ti-6Al-4V, a smaller lamellar structure was produced at higher cooling rates, which reduces the grain growth time [50].

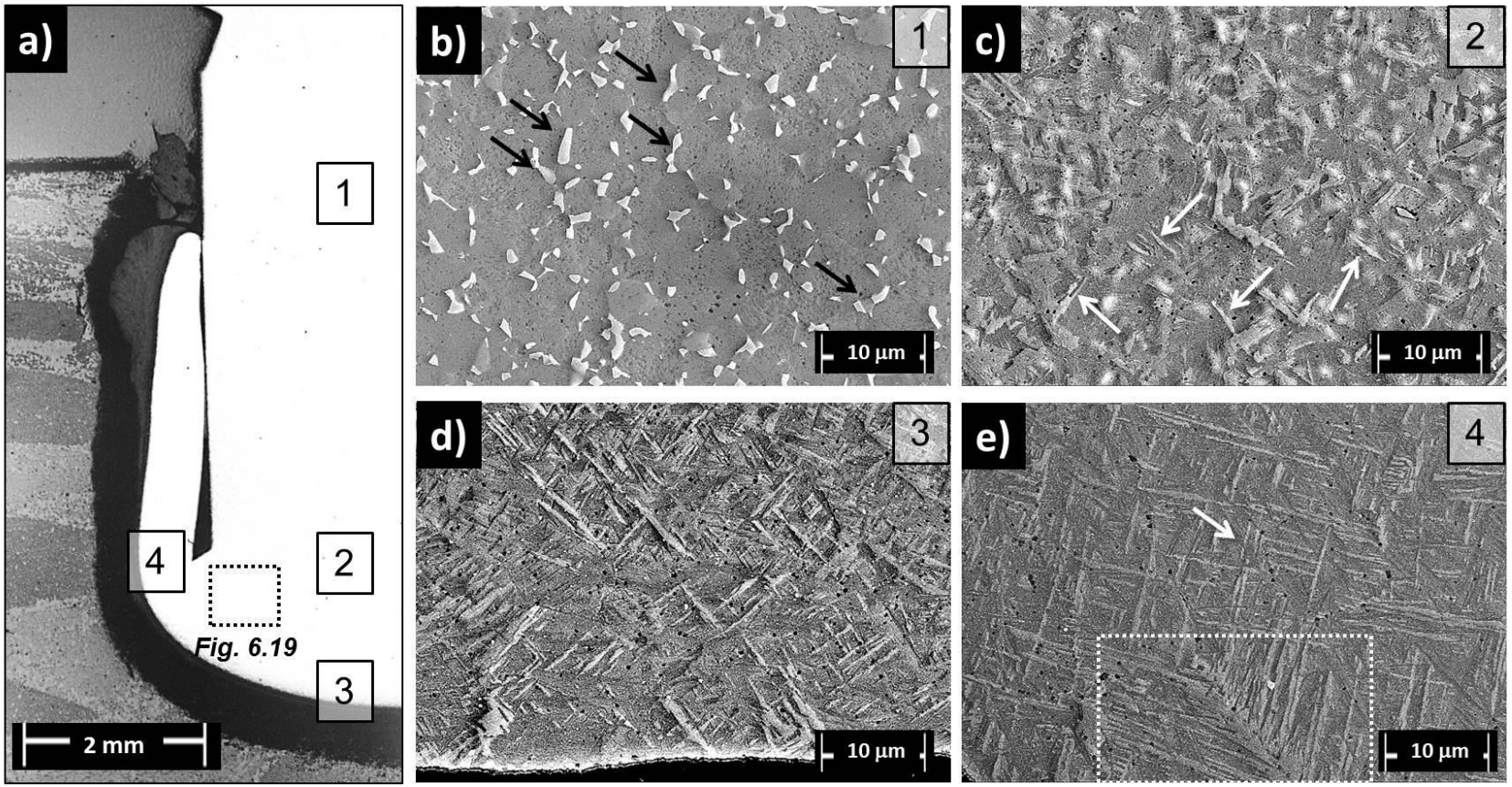

Figure 9.2 SEM images. a) General overview of a typical Ti-6Al-4V/GF-P joint with four regions of interest. Regions 1 to 4 are detailed in figures b to e (C2: RS = 9000 rpm, FT = 1.2 s and FOT = 1.2 s; $T_{p,\,C2\text{-}1}$= 814 °C).

Table 9.2 Summary of the grain sizes and aspect ratios of different microstructures developed through rivet resulting from FricRiveting.

	Base Material	**Region 1**	**Region 2**	**Region 3**	**Region 4**
	equiaxed structure		***transition***	***acicular structure***	
α-Grain Width (μm)	4.5 ± 0.9	5.4 ± 1.8	4.9 ± 1.0	0.5 ± 0.1	0.3 ± 0.06
α-Aspect Ratio, w/l	0.9 ± 0.02	0.9 ± 0.1	0.8 ± 0.1	0.09 ± 0.02	0.04 ± 0.01
β-Grain Width (μm)	0.6 ± 0.1	0.9 ± 0.2	0.8 ± 0.2		
β-Aspect Ratio, w/l	0.4 ± 0.06	0.4 ± 0.1	0.3 ± 0.1		

TEM analysis was performed to explore the phenomena occurring in the transition of equiaxed and acicular microstructures. In Regions 3 and 4, two types of acicular structures were apparently formed. In Region 4, the arrow in Figure 9.2-e evidences acicular phases oriented in rectangular patterns; this is a typical martensitic (α') structure, as defined in [122, 126]. In general, they form by diffusionless transformation. Additionally, the dashed lines-square in Figure 9.2-e outlines a string phase (boundary) with bundles of acicular lamellae growing from this boundary. According to Baufeld *et al.* [127], this is a typical Widmanstätten structure formed by diffusional process. TEM bright field (BF) image of the lamellae from the Widmanstätten structure is shown in Figure 9. 3. The indexed selected area electron diffraction (SAED) pattern resultant in hexagonal symmetry attributed to the transformed α-Ti phase oriented in the $[0001]_{\alpha\text{-Ti}}$ zone axis.

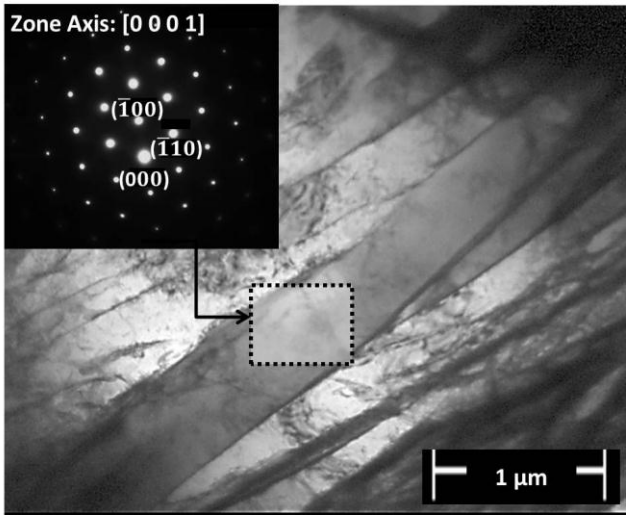

Figure 9. 3 TEM bright field image of Widmanstätten microstructure in Region 4 of Ti-6Al-4V rivet, with its SAED oriented in the $[0001]_{\alpha\text{-}Ti}$ zone axis (joining condition of C2: RS = 9000 rpm, FT = 1.2 s and FOT = 1.2 s; $T_{p,\ C2\text{-}1}$= 814 °C).

A comparison between the X-ray diffraction (XRD) patterns from the base material and thermo-mechanically affected sample from Region 3 is well in accordance with the later statement about the martensitic formation, also presented in Region 4. The results are presented in Figure 9.4. The Bragg's peaks of the as-received material (Figure 9.4-a) showed a simple XRD pattern of hexagonal close packed (hcp) α-Ti phase and body-centered cubic (bcc) β-Ti phase. However, in the diffractogram of the FricRiveting sample (Figure 9.4-b) - material was extracted from the representative Region 3-, the presence of a weak peak of β-Ti phase (at around 2θ = 40°) evidenced the fact that some of this phase could be converted into the hexagonal martensitic α' phase. The XRD data also provided a first impression about the absence of peaks for orthorhombic martensite (α''). In this case, the spectra should present a more pronounced central peak at the same 2θ rage surrounded by two additional peaks attributed to the distinct lattice parameters of orthorhombic crystal structure (a≠ b ≠ c) [128]. Similar results were reported by Esmaily *et al.* [67] for *Friction Stir welded* (FSW) and *Gas Tungsten Arc welded* (GTAW) Ti-6Al-4V alloy. Therefore, depending on the heat input and cooling conditions, either plate-like Widmanstätten or martensitic structure was formed, creating a

complex microstructure in the anchoring region of the metallic rivet. The diffractogram of material from Region 4 is depicted in Appendix C.

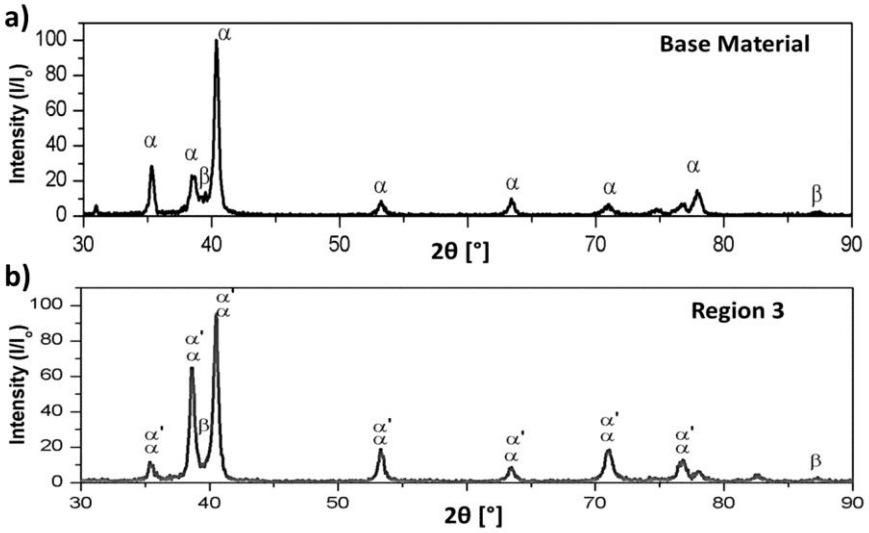

Figure 9. 4 X-ray diffraction patterns of a) the Ti-6Al-4V base material and the b) Ti-6Al-4V from the anchoring zone (Region3) of the Ti-6Al-4V/GF-P friction-riveted joint (joint from joining condition C2: 9000 rpm, 1.2 s and 1.2 s; $T_{p,C2-1}$= 814 °C).

TEM bright (BF) and dark field (DF) images from the transition area (Region 2) are presented Figure 9.5-a and -b, respectively. The equiaxed microstructure of Figure 9.2-c, typical for the base material, can be observed in higher magnification. In contrast to the base material microstructure (Figure 7.1-b), the chemical composition of α-Ti (Figure 9.5-c) and β-Ti (Figure 9.5-d) phases varied (EDS spectrum of the Ti-6Al-4V base material can be seen in Appendix B). The aluminum (Al) and vanadium (V) content of each phase revealed that the Al content changed slightly in Region 2, which, in comparison to the base material, was exposed to temperature and shear rate. Additionally, the V content, particularly from the β-Ti phase, changed significantly in comparison to α-Ti (see Figure 9.5-c and -d). The same behavior was identified by Elmer *et al.* [129] for heat treated Ti-6Al-4V alloy by synchrotron radiation to directly observe the α→β phase transformation. From TEM-EDS analysis of the base material, the content of vanadium in the β-Ti phase was identified as greater than 90% of the V content in the α-Ti phase (see Appendix B) while in

the selected region, this increment was of around 50%. Therefore, V seems to be more homogeneously distributed through α-Ti and β-Ti phases in Region 2 of the rivet than in the base material. Figure 9.6 schematically represents the V content distribution through the phases in the Ti-6Al-4V base material and in the thermo-mechanically affected sample of Region 2.

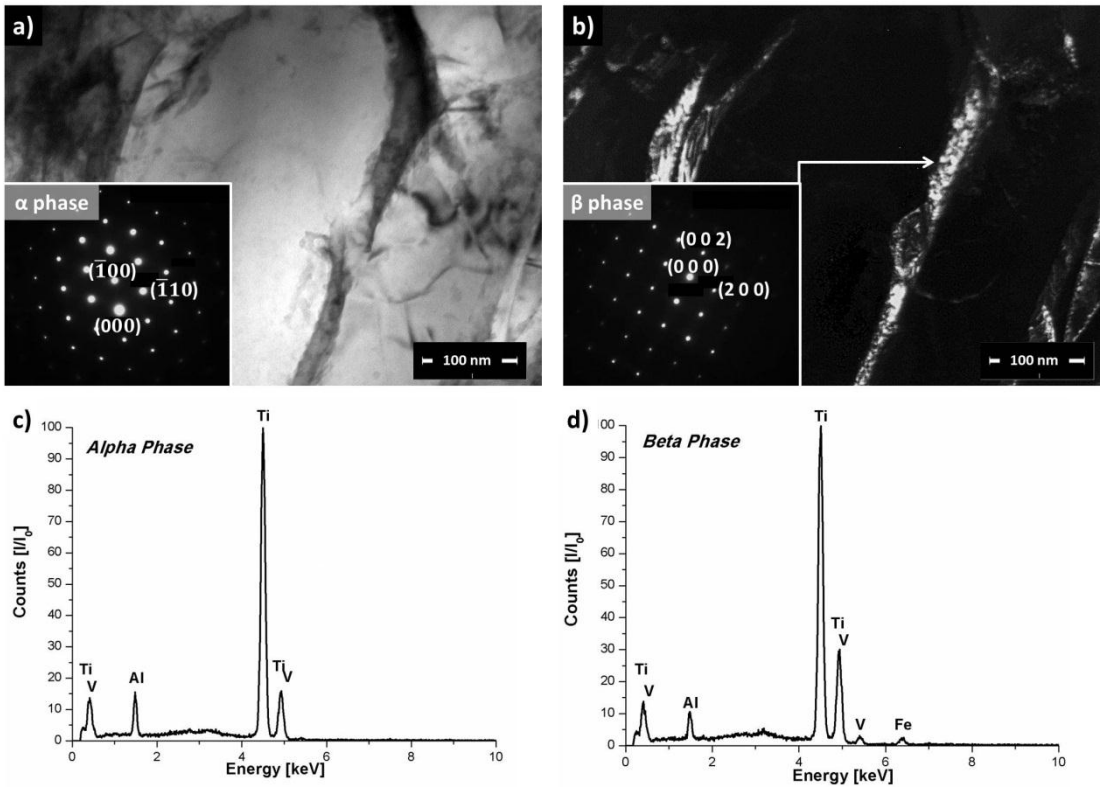

Figure 9. 5 a) TEM bright field image of Region 2 with SAED oriented in the $[0001]_{\alpha\text{-}Ti}$ zone axis; b) TEM dark field image of Region 2 detailing the β phase with SAED oriented in the $[001]_{\beta\text{-}Ti}$ zone axis. Semi-quantitative chemical compositions of c) α phase and d) β phase in Region 2 of post-processed rivet (joint from joining condition C2: 9000 rpm, 1.2 s and 1.2 s; $T_{p,C2\text{-}1}$= 814 °C).

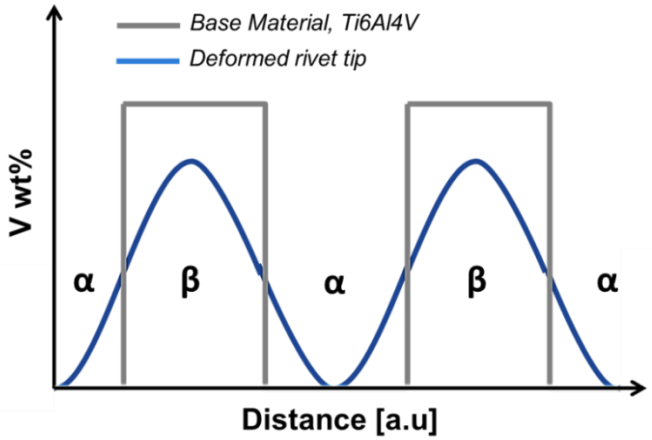

Figure 9. 6 Schematic representation of the vanadium distribution through the Ti-6Al-4V phases in the base material and Region 2- deformed rivet tip.

These results indicated that, in this transition area (Region 2), during the cooling of the joint under pressure, the β→α phase transformation was partially governed by diffusion. The vanadium diffused from β-Ti phase to α-Ti phase, due to the high temperature experienced by the material during the joining process. Nevertheless, the diffusion could be considered incomplete, with remaining saturated regions of V, represented by white spots in Figure 9.7. In the literature, the V saturated regions are called β flecks [103]. These regions were deformed and realigned in the direction of the material flow during the forging phase of the joining process. The dashed arrows in Figure 9.7 indicate the material flow outwards, forming the “legs” in the metallic rivet. Generally, β-fleck regions form at temperatures above the β-*transus* temperature and they are more common for titanium alloys with a greater β-stabilizer amount, such as near-β alloys [103].

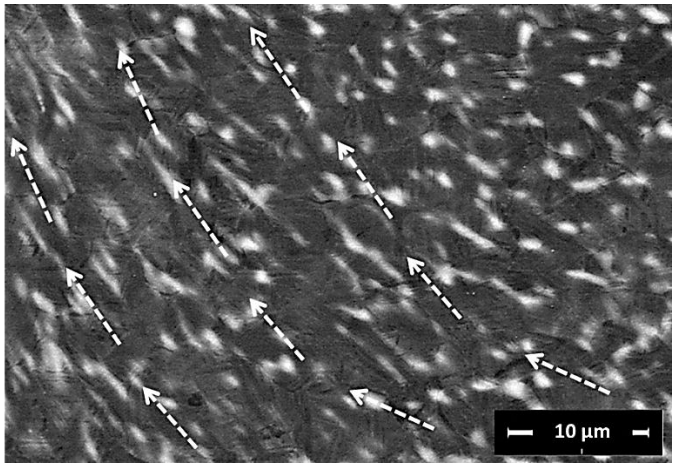

Figure 9. 7 SEM image of the anchoring zone (transition between Regions 2, 3 and 4, depicted in Figure 6.14-a), showing the metallic material flow through dashed arrows and elongated β fleck regions (joint from joining condition C2: 9000 rpm, 1.2 s and 1.2 s; $T_{p,C2\text{-}1}$= 814 °C).

EBSD analysis was performed to evaluate the metallurgical phenomena, such as dynamic recovery and recrystallization, associated with the plastic shear deformation imposed by the rotating metallic rivet and process temperature. Considering that Region 1 was only influenced by heat, no dynamic metallurgical phenomena are expected; therefore it is not addressed in the following paragraphs. Figure 9.8 shows the inverse pole figures (IPF) for Regions 2 (Figure 9.8-b) to Region 4 (Figure 9.8-d) in the metallic rivet. The grains are colored according to their crystallographic orientation which triangle code is evidenced in the right side of the maps. Additionally, the fractions of low angle boundary (LAB) and β-Ti phase for each region are presented in Table 9.3 with the correspondent area covered by the maps. The grain boundaries and the phase distribution/content maps are displayed in Appendix D. Although this additional information indicate trends among the regions, no quantitative analysis can be done since the EBSD maps were performed in different magnitudes for each region, and, consequently, covered different total areas. Due to the grain refinement from Region 2 to 4, the precise acquirement with a constant step size was hindered.

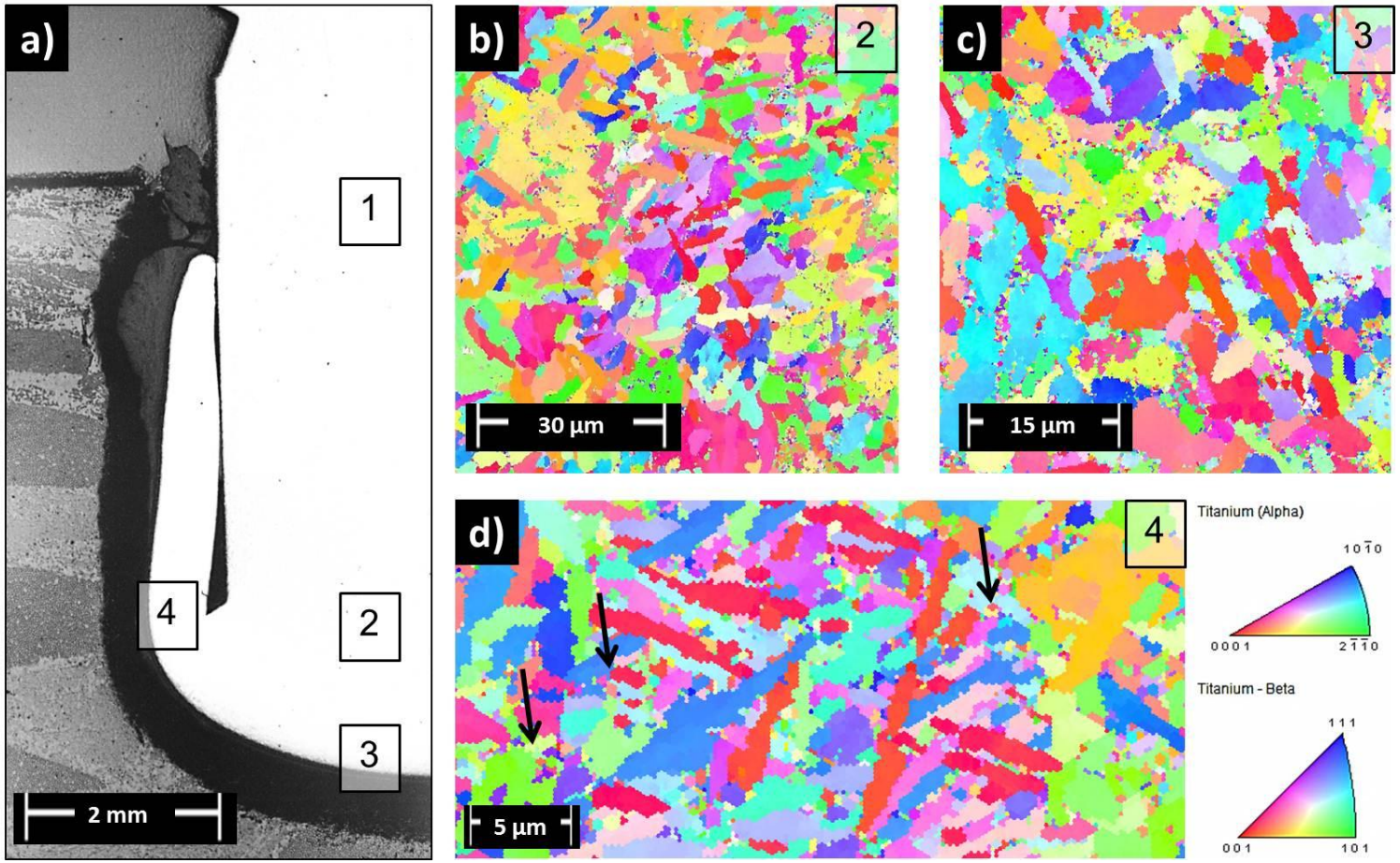

Figure 9. 8 a) SEM image of a typical cross section of Ti-6Al-4V/GF-P joint pointing out four regions of interesting. The crystallographic orientations of Regions 2 to 4 are detailed in figures b to d, respectively, through EBSD maps (joint from joining condition C2: 9000 rpm, 1.2 s and 1.2 s; $T_{p,C2\text{-}1}$= 814 °C).

Table 9. 3 Summary of β-Ti phase fraction and low-angle boundaries of T-6Al-4V in regions shown in Figure 6.20.

	Base Material	Region 2	Region 3	Region 4
Fraction of β-phase (%)	8.7	1.7	3.7	2.7
LABs (2-15°) (%)	7.2	9.2	15.5	18.4
Covered area (μm^2)	4197.1	7183.2	2516.5	1142.7

By the IP figures, no preliminary conclusions can be done regarding the recrystallization phenomenon. From Region 2 to 4, an apparent visual increase in the needle content could be noticed, as well as a preferential orientation of some of these structures. In general, all the regions had a decrease in β-Ti phase fraction in comparison to the base material (8.7%). Additionally, the LAB increased from Region 2 to 4. This indicates that possibly a dynamic recrystallization took place in regions where a higher shear rate and temperature were imposed, *i.e*. in Region 4. When the processing temperatures are above the β- *transus*, probably the case of Region 4, no second-phase is present to pin the β-Ti grain boundaries and recrystallization proceeds without any constrain through dynamic recrystallization (DRX) [125]. Although sub-micron domains were present in Region 4 (marked with black arrows in Figure 9.8-d) – an indication of the DRX occurrence [130]- the phase transformation was more intense and partially hid the DRX phenomenon. The formed acicular grains seem to be in stable orientations after the joining process. In general, this effect is common in titanium alloys, due to the low symmetry and plastic anisotropy of the α-Ti phase [125].

Although the metallic flow during the Friction Riveting appears to be complicated, the predominant deformation is expected to be simple-shear texture, as described for *Friction Stir Welding* [55]. In order to evaluate the simple-shear texture imposed by this joining process, the $(0001)_{\alpha\text{-}Ti}$ and $(11\bar{2}0)_{\alpha\text{-}Ti}$ pole figures were analyzed for each region of interest in the metallic rivet (Regions 2 to 4, Figure 9.8-a), as presented in Figure 9.9. Once the fractions of the retained β-Ti phase were too low through the investigated regions (Table 9.3) and the β→α phase transformation follows the Burges orientation relationship - $(101)_{\beta\text{-}Ti} \parallel (0001)_{\alpha\text{-}Ti}$ and $[11\bar{1}]_{\beta\text{-}Ti} \parallel [11\bar{2}0]_{\alpha\text{-}Ti}$ –, the β-Ti phase

texture measurement can be done by using only the α-Ti phase texture monitoring. The $(0001)_{\alpha\text{-}Ti}$ and $(11\bar{2}0)_{\alpha\text{-}Ti}$ pole figures are a rough approach for texture analysis of Ti-6Al-4V alloy, as proposed by Mironov *et al.*[72] and described in Section 3.2.2.

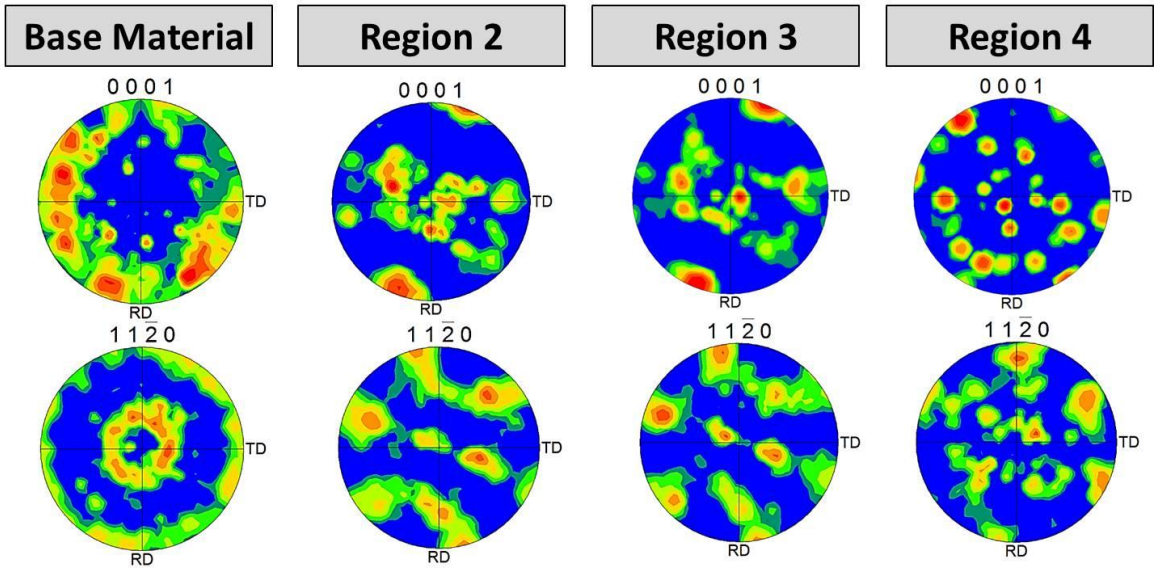

Figure 9. 9 Experimental pole figures derived from α-Ti phase for joint presented in Figure 6.20. RD and TD are rolling direction, analogous to the axial force direction applied during FricRiveting, and transversal direction, respectively.

The results show a decrease in microtexture from the base material to Region 4. The basal planes in Regions 2 and 3 suitably re-oriented for slip rotate to an orientation with possibly higher shear stress, approximately at 45° to the rolling direction, RD (direction analogous to the axial force direction applied in the rivet during the forging phase). In Region 4, the microstructure has apparently an absence of microtexture which is contradictory to what is commonly observed in continuous recrystallization reaction in Ti-6Al-4V alloy. Normally in this case, colonies of lamella are easily recrystallized since they are in non-ideal orientation, storing energy faster to spherodize [130]. This suggests that additional factors must be considered under high strain rate and temperatures, such as the β→α phase transformation. This lack of deformation

texture can be attributed to the number of possible orientations, which the β-Ti grains can potentially transform into α-Ti phase. A single bcc grain can transform theoretically to 12 possible orientations/variants during the β→α phase transformation due to the possible slipping systems of α-Ti phase [61]. Therefore, this partially may explain the random final texture, if all these 12 variants have the same statistical probability to be formed.

Finally, by detailing of the morphologies and possible phenomena taking place in the metallic rivet, the variation of microstructures through Regions 1 to 4 suggested differential heat distribution and mechanical loading over the metal during the joining process. The differential heat and cooling rates were imposed by the variation of coefficient of friction. This happens mainly due to two factors: the inhomogeneity in the fiber distribution and concentration in the joint area, usually found in pultruded GF-P parts [131]; and differential angular speed throughout the rivet radius. The radial (angular) speed is zero at the rotational axis of the rivet, and increases from the center to the circumference of maximum diameter. Considering that, it is expected that the frictional heat generation also increases in this manner [46, 116], resulting in a high process-affected material volume in the deformed anchoring region. Suhuddin *et al.* [132] reported similar behavior in friction surfacing of dissimilar aluminum alloys welding processes. Additionally, in the anchoring zone where the rivet tip widening occurred and the acicular morphology of the grains was predominant (Figure 9.2), the increase in contact (rubbing) area of the rivet contributed to the high heat generation and temperature/friction exposure of the metallic material enabling phase transformations by different processes. Figure 9.10 schematically represents the main contributions to the microstructure evolution through the Ti-6Al-4V rivet.

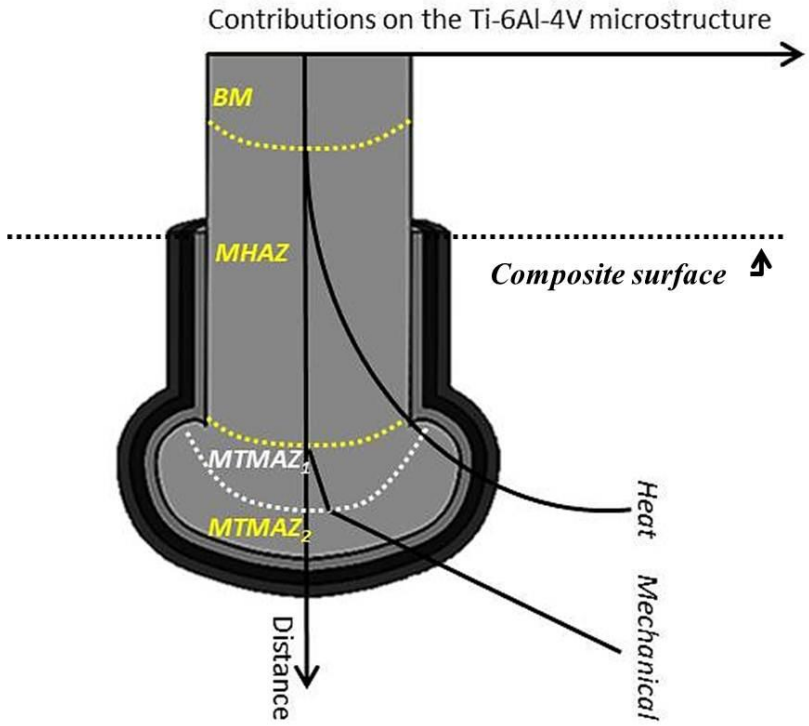

Figure 9. 10 Schematic illustration of microstructural transformations in the rivet of Ti-6Al-4V/GF-P joints.

As described in Figure 9.2, Region 1, where the equiaxed morphology was maintained similarly to the base material but with slight grain coarsening, can be defined as a metal-heat affected zone (MHAZ). No plastic deformation was evidenced in this region. A macro indication of plastic deformation may be associated to the barreling phenomenon (increase in rivet diameter) [41]. Another indication of occurrence of plastic deformation in the micro-scale could be the formation of twinning as shown by Altmeyer *et al.* [46] for friction riveted joints of α-commercially pure Ti grade 3/CF-PEEK. In general, some types of twinning in hcp structures (α-Ti phase), which has lack of slip systems, is a way to accommodate plastic deformations [133]. However, the presence of the bcc structure in Ti-6Al-4V alloy can relieve deformations through the numerous slipping systems of this structure. Facing these considerations, only thermal phenomenon such as grain coarsening could have occurred in Region 1. Region 2 is a transition zone where mechanical work was evidenced in the micro-scale through the increase of low angle boundaries (LABs) (9.2%) in

comparison to base material (7.2%) as shown in Table 9.3. Therefore, this zone is thermo-mechanically affected (metal-thermo-mechanically affected zone 1, $MTMAZ_1$). Regions 3 and 4, where a dynamic recrystallization probably took place (Figure 9.2-d and -e), are considered a second metal-thermo-mechanically affected zone ($MTMAZ_2$). These observations are in agreement with Altmeyer *et al*. [46]. The $MTMAZ_2$ was more severe affected by the process leading to the characteristic presence of acicular structures (Widmanstätten and martensite). Altmeyer *et al.* [46] observed also a metal friction zone (MFZ) described as a region close to the surface of the rivet tip dominated by fine dynamically recrystallized grains (average grain size of about 0.7μm). MZF was not observed Ti-6Al-4V/GF-P friction-riveted joints since the DRX phenomenon may be partially hidden by the phase transformations occurred in the anchoring zone of the α+β alloy, as described in this Section 9.2.

The influence of the joining conditions (*i.e.* energy input) on the evolution of the microstructure over the rivet was analyzed as well. Figure 9.11 displays the typical back scattered images from Region 1 (Figure 9.2) - for each evaluated joining conditions. All the joints presented the main metallurgical zones described above, but with differences in their extent (see hardness investigation to be presented in Section 10.1).

Another difference was noticed in Figure 9.11. In Figure 9.11-c, the high energy input experienced by C3 (Section 8.1) – the joint with higher RS and FT- along with the low thermal conductivity of Ti-6Al-4V alloy (6.7 M $m^{-1}K^{-1}$) [57] yielded fully lamellar structure even in Region 1. The Widmanstätten structure was predominant, confirming the exposure of this volume of material to high temperatures during a considerable time. These are sufficient requirements to promote diffusional processes [110].

The understanding of the energy input-related metallurgical changes mechanisms for the case-study friction-riveted joints is very complex and out of the scope of this work. Nonetheless, it is assumed that, the microstructure transformation from equiaxed to acicular morphology may happen majority in the $MTMAZ_1$ and $MTMAZ_2$ mainly in the anchoring zone. For C1 joints, which achieved process-temperatures well below the β-*transus* temperature, the

presence of acicular structure, perhaps metastable martensite, can be formed from different mechanism in comparison to C2 and C3 joints, which undergo higher process-temperatures. Ti-6Al-4V alloy is prone to martensitic transformation induced by either temperature (Temperature-Induced Martensitic Transformation- TIMT) or stress (Stress-Induced Martensitic Transformation-SIMT), whose mechanisms progress in different manners [134]. In SIMT, transformations over loading proceed under an almost constant stress and the amount of stress-induced martensite is a function of strain level [134]. In C1 probably SIMT occurred while in C2 and C3 the major transformation came from TIMT. Further studies must be carried out to confirm these assumptions.

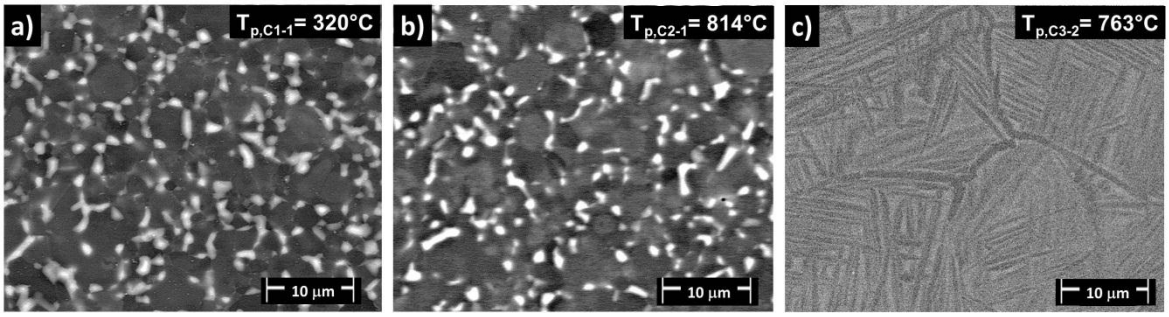

Figure 9. 11 SEM images of Ti-6Al-4V from Region 1 (MHAZ) for case-study joining conditions a) C1; b) C2 and c) C3.

The predominance of one morphology over others dictates the mechanical properties of the heat/thermo-mechanically affected regions through the rivet and will be discussed in Section 10.1.

9.3 Interphase Analysis at the Interface between the Rivet and Thermo-Mechanically-Changed Composite

Figure 9.12 presents the details of three regions showing the interphase formed between the metallic rivet and the GF-P: outside the anchoring zone in the formed rivet “leg” (Figure 9.12-b), at the anchoring zone (Figure 9.12-c) and underneath the rivet central portion (Figure 9.12-d). In the earlier stage of the frictional phase, the rivet drilling action was responsible for the fiber network

breakage and its displacement from the composite matrix; similar phenomenon was observed under wear testing between a metal and a polymeric composite and described by Friedrich [123]. Moreover, the temperature overcame the onset decomposition of the polyester matrix and softened/melted the damage fibers as previously discussed. As discussed in Section 8.3, the molten glass was subsequently deposited on the rivet surface. Each region of this consolidated continuous glass interphase presents a particular stress field induced by differences throughout the material flow.

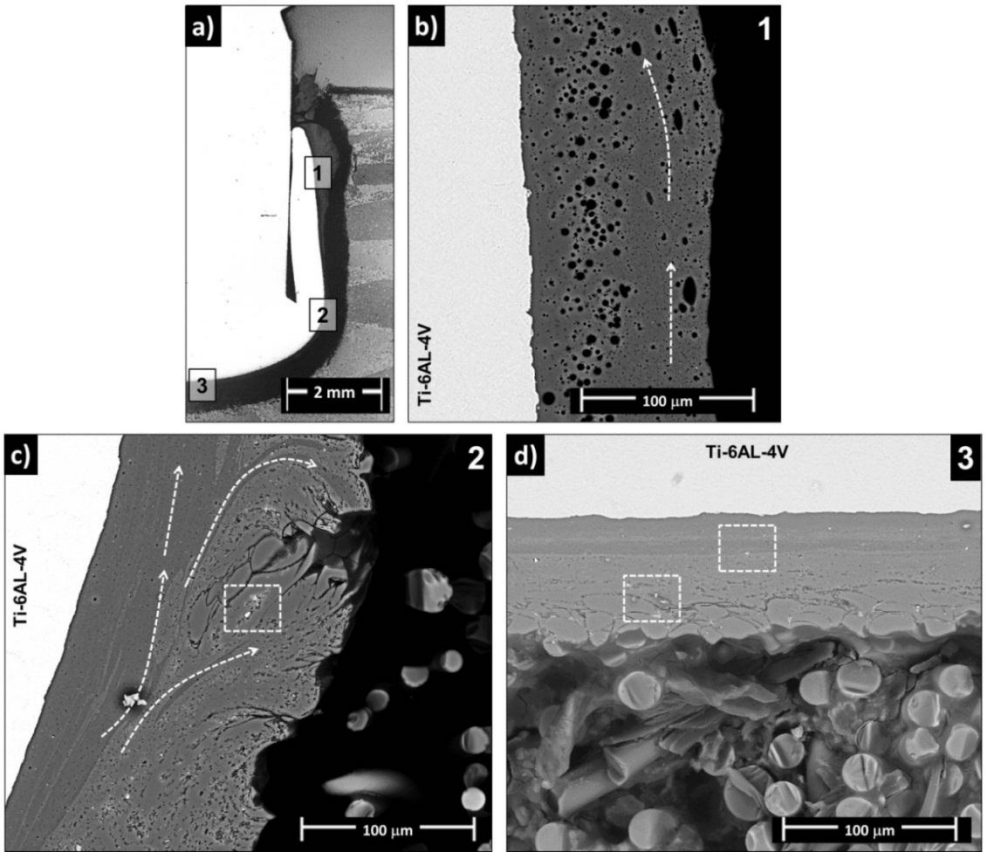

Figure 9. 12 SEM images. a) Overview of a typical Ti-6Al-4V/GF-P joint, where three regions of interest at the metal-composite interface are indicated. Regions 1 to 3 are detailed, respectively, in b-d figures (joint produced under condition C2: RS = 9000 rpm, FT = 1.2 s and FOT = 1.2 s; $T_{p,C2\text{-}1}$= 814 °C).

Region 1 is characterized by the presence of a significant amount of volumetric flaws in the formed interphase material. The inner voids (close to the rivet) are spherical while the outer voids are elongated in the flow direction marked with arrows in Figure 9.12-b (parallel to the rivet insertion direction).

The voids are thought to be responses of either entrapment of volatilized products remained from the matrix degradation or air entrapment due to the high viscosity of the molten glass layer, as reported by [135]. The inner glass layer consolidated quickly, retaining the spherical shape of the voids while the outer were submitted to the outward glass flow.

The centrifugal force generated by the rivet rotation combined with the high axial force after the rivet deceleration during the forging phase, led to the final flow pattern of glass material, highlighted by white arrows in Region 2 (Figure 9.12-c). The concentration of voids was reduced, probably due to the high compression field in this region, where the rivet tip widening occurred. The same evidence was observed in Region 3 (Figure 9.12-d). The intense compression field allowed close attachment between the metal and the interphase material, resulting in the absence of voids.

In Regions 2 and 3, the white dashed squares (Figure 9.12-c and -d) point out the presence of bright particles/agglomerates. These particles can be seen into detail in Figure 9.13-a. The semi-quantitative chemical composition of the particles was measured by EDS and the result is shown in Figure 9.13-b. The particles are majority composed by titanium (Ti), silicon (Si) and oxygen (O) atoms. Therefore, these agglomerates include metallic fragments originated from the severe solid-friction between the rivet tip and the thermoset composite, and probably a crystal phase formed from the glass fiber. The visual difference among the particles forming these agglomerates demonstrated changes in the refractive index, which can be response of the glass crystallization in some special phases such as cristobalite (α- SiO_2) [136]. According to Imanaka *et al.* [137], this structure is precipitated when alumina content is low and temperatures ranged between 800°C and 1100°C. The cristobalite precipitation modifies the microstructure of the glass layer, leading to more viscous material in comparison to the single-phase and affecting the thermal properties as well as increasing the hardness of the material [136]. Furthermore, cristobalite has a transformation from α- to β- cristobalite around 200°C. This transformation results in large volumetric change and provides high thermal expansion which in turn can originate voids and microcrack formation after cooling [136]. Deeper

investigation on these particles could be performed using an electron micro-diffraction. However, this analysis is beyond the scope of this work.

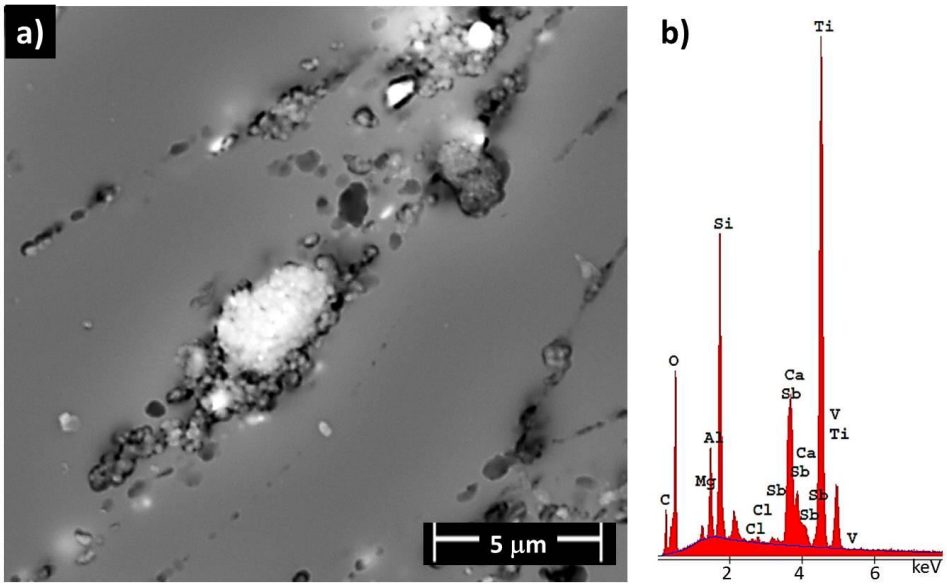

Figure 9.13 a) SEM image of agglomerates in the interphase material formed between T-6Al-4V rivet and GF-P composite in Regions 2 and 3, from Figure 6.24; b) semi-quantitative chemical composition of the particles presented in a).

Figure 9.14 shows the semi-quantitative chemical composition EDS maps of this process-related interphase formed between the metal and the composite. As expected, the composition of this layer includes the main elements presented in the glass-fiber. They are: aluminum (Al), silicon (Si), calcium (Ca) and oxygen (O). The small presence of carbon element indicates substantial ejection of the degraded polyester matrix (char) as a flash during the rivet penetration and forging. This EDS results provided additional information to support the hypothesis of a glass layer formation at the interface metal-composite.

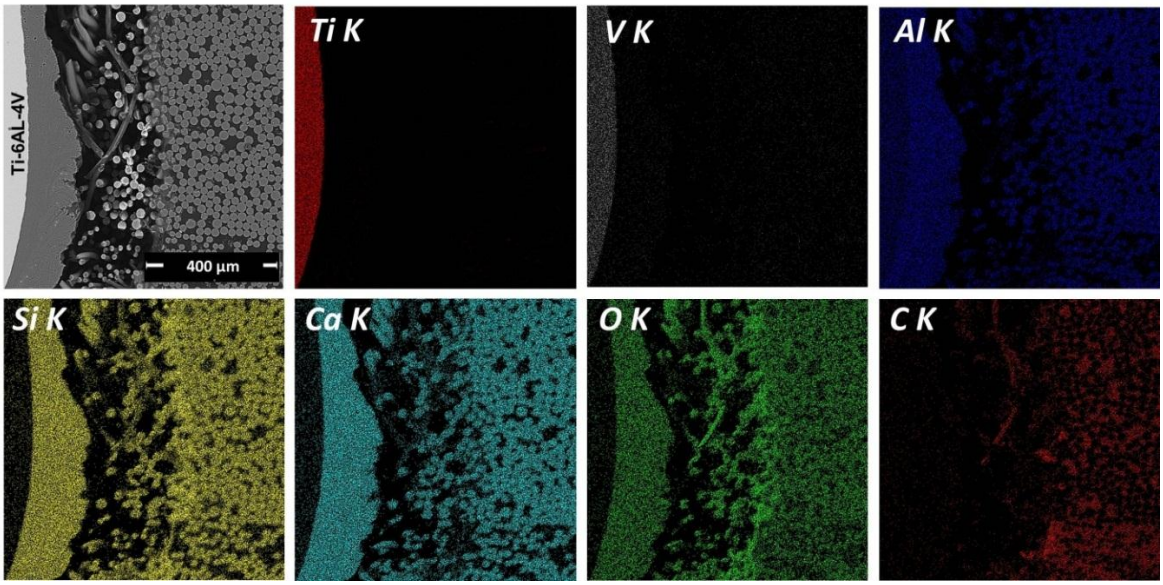

Figure 9. 14 Semi-quantitative chemical composition EDS maps of the interphase material between the Ti-6Al-4V and GF-P composite. Ti and V are elements exclusively presented in the metallic rivet. Small amounts Ti (not visible in this magnification) may be presented in the interphase material (see Figure 9.13).

In comparison to the original GF, the glass interphase is much harder, as measured by nanohardness analysis presented in Figure 9.15. The nanohardness increased approximately 100% from the GF (HV_{GF} = 479 ± 7 HV) to the glass interphase (HV_{R2} = 906 ± 46 HV; HV_{R3} = 963 ± 67 HV). This may be due to the formation of cristobalite as previously discussed. Another hypothesis, but less probable, is the densification of the glass due to the compression field in Regions 2 and 3 [138]. Between these two regions, Region 2 compacted to a lesser extent than Region 3, presented slightly 6% lower HV (HV_{I2} = 906 ± 46 HV; HV_{I3} = 963 ±67 HV), which might evidence the effect of the stress field on the local mechanical property. However, the presence of cristobalite can lead to more difficult densification due to the high viscosity of the bi-phase glass [136], which would contradict this later assumption.

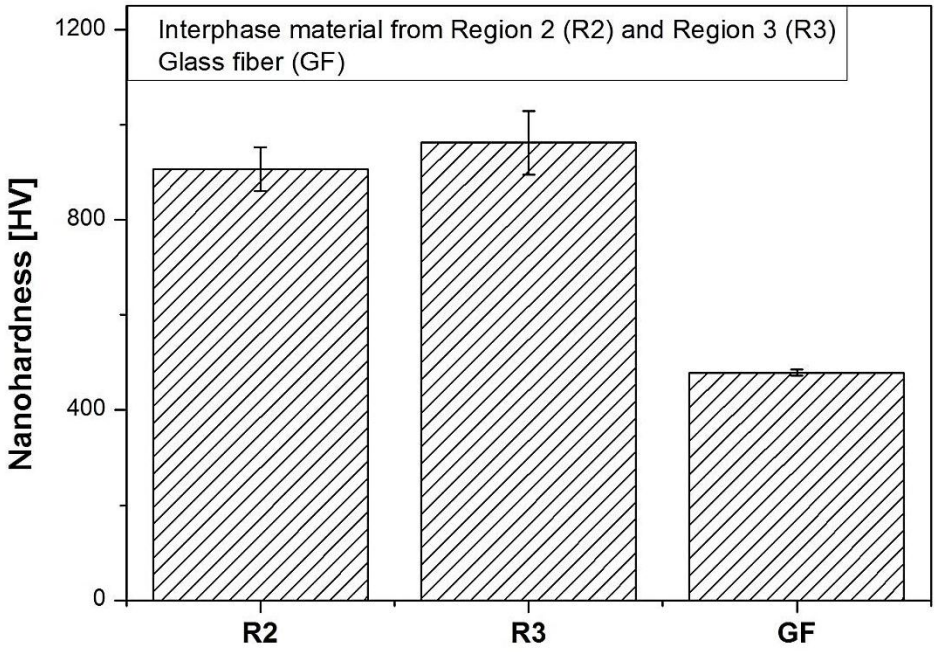

Figure 9. 15 Average nanohardness of two compacted regions in the interphase material between Ti-6Al-4V and GF-P (Region 2, R2 and Region 3, R3) and of original glass fiber (GF) from the GF-P base material.

9.4 Microstructural Analyses of Glass Fiber Reinforced Thermoset Polyester

The process-related transformations in the composite were studied through the microscopic analysis of a typical cross-section of Ti-6Al-4V/ GF-P joint, as presented in Figure 9.16. Three regions (1-3, Figure 9.16-a) were characterized and divided into three zones each (CTMAZ-HD, CTMAZ-PD and BM), regarding the observed differences in microstructures - in terms of type and amount of volumetric flaws and fiber orientation. Due to the low thermal conductivity of the composite (Table 5.3) and of titanium alloy (Table 5.2) there is a local temperature increase in the joining area. Thereby, zones with thermally/thermo-mechanically modified composite material were formed around the deformed rivet tip.

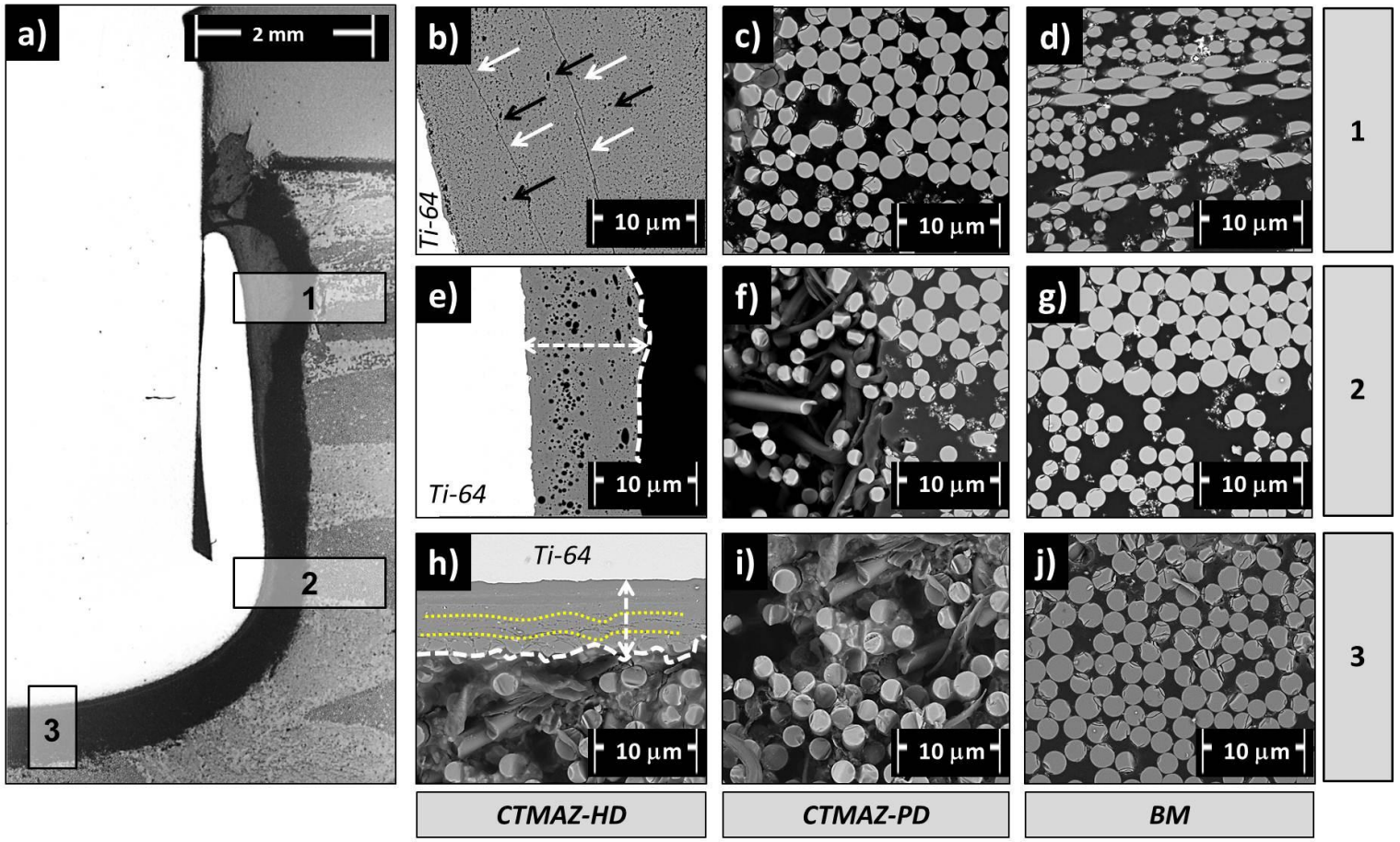

Figure 9. 16 SEM images of process-modified GF-P composite for three different regions at the composite part. The identified microstructural zones are indicated: CTMAZ-HD, CTMAZ-PD and BM (joint produced under condition C2: RS = 9000 rpm, FT = 1.2 s and FOT = 1.2 s; $T_{p,C2\text{-}1}$= 814°C).

The composite thermo-mechanically affected zone (CTMAZ) is the region immediately close to the rotating rivet which was longer exposed to high temperatures and shear rates, following the statement proposed by Amancio-Filho [139]. Furthermore, Altmeyer *et al.* [46], identified some geometrical singularities of the CTMAZ for short-fiber reinforced thermoplastics based on the process-modified fiber orientation after consolidation. Although their description may be used to allow the understanding of different material flow and shear rates, it can not be used to describe the CTMAZ characteristic in this work.

The CTMAZ of Ti-6Al-4V/GF-P joints comprises two distinct subzones addressed for the first time in this work: a highly-degraded composite thermo-mechanically affected zone (CTMAZ-HD) (Figure 9.16-b, -e and -h) and a partially degraded composite thermo-mechanically affected zone (CTMAZ-PD) (Figure 9.16-c, -f and -i). The CTMAZ-HD can be described as the continuous interphase consolidated on the rivet surface and already characterized as a glass layer (see Section 9.3). The adhesion between this layer and the metallic rivet – one of the main joining mechanisms of friction-riveted joints - presented differential behavior through Regions 1-3. In the regions where a high compressive stress level was established during the consolidation under forging phase (e.g. Regions 2, Figure 9.16-e and 3, Figure 9.16-h), intimate contact between the metal and the glass was observed. In this case bonding between rivet and consolidated interphase material may happen by the typical adhesion mechanisms observed in metal-polymer adhesively- bonded joints: mechanical interlocking, chemical and electrostatic bonding [140]. The analysis of the adhesion mechanisms is not within the scope of this work and will not be addressed in this thesis.

Additionally, the axial pressure imposed by the rivet on the glass layer appears to have formed hydrostatic-pressure lines perpendicular to the direction of the applied force, as highlighted in Region 3 by yellow dotted lines (Figure 9.16-h). In Region 1 (Figure 9.16-b) located above the deformed rivet tip, and experienced only limited compression imposed in the interaction volume, tiny voids nearby the metallic rivet were observed (marked with black arrow in

Figure 9.16-b). Besides the flaws already described, micro-cracks were formed inside the CTMAZ-HD (indicated by white arrows in Figure 9.16-b) which might be a result of differential thermal contraction between colder and hotter glass front.

CTMAZ-PD (Figure 9.16-c, -f and -i) was identified as a discontinuous zone with an extensively fiber network breakage. Broken and reoriented fibers as well as the absence of matrix were observed. The large volumetric flaws were resultant of expelled degraded polyester matrix during the joining and the displacement of broken and softened glass fibers from the composite to the CTMAZ-HD. Therefore, a poor interface was generated between CTMAZ-HD and CTMAZ-PD, thus weakening the joint; this interface will probably act as crack nucleation sites and preferential path during mechanical testing. Figure 9.17 illustrates the CTMAZ and the differences between the subzones.

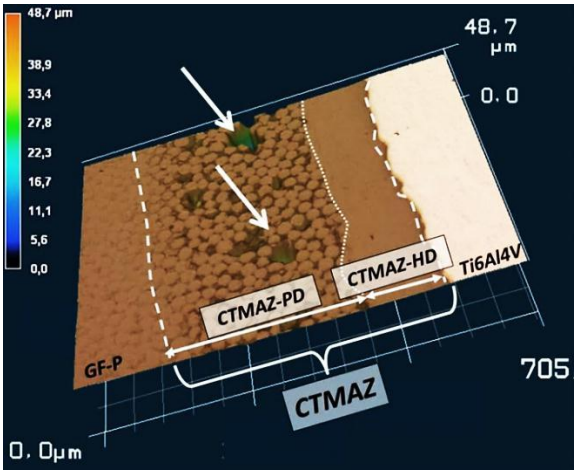

Figure 9. 17 Topography of the CTMAZ obtained by laser microscopy, showing the presence of volumetric flaws in the CTMAZ-PD.

In Regions 1-3 (Figure 9.16-d, -g and -j), a third subzone showing neither pores nor reoriented fibers can be observed. This subzone were not heated up to high temperatures or mechanically deformed. According to Borba *et al.* [16] and Altmeyer *et al.* [46], and based on the statements proposed by Amancio-Filho in [139], a composite heat affected zone (CHAZ) may be formed in friction riveted joints, which can be described as the volume around the rivet whose temperature during joining did not reach the polymer degradation temperature;

the physical integrity of the fiber network is kept unchanged, displaying similar visual microstructure as the base material. Moreover Amancio-Filho *et al.* [41], showed that for amorphous thermoplastics such as polyetherimide, an increase in hardness in this region may be expected since, considering the temperature under T_g, phenomena such physical aging (or structure relaxation) can take place [141]. Nevertheless, nanohardness investigation performed in the polyester matrix indicated no differences compared to the polyester-base material (see Section 10.1). The presence and extension of a CHAZ could not be identified by microscopy and nanohardness. Therefore, the third zone was classified as composite base material.

The model proposed in this work to describe the microstructural zones in glass fiber reinforced thermosets in hybrid friction-riveted joints is illustrated in Figure 9.18. This approach is valid for all the joint conditions investigated. The extension of each zone varied through the increase of energy input from C1 to C3. However, the inconstancy of each zone thickness does not allow their correct and precise measurement; this may be accomplished by advanced analytical techniques, such as atomic force microscopy, Raman spectroscopy and X-ray- computer microtomography (µ-CT).

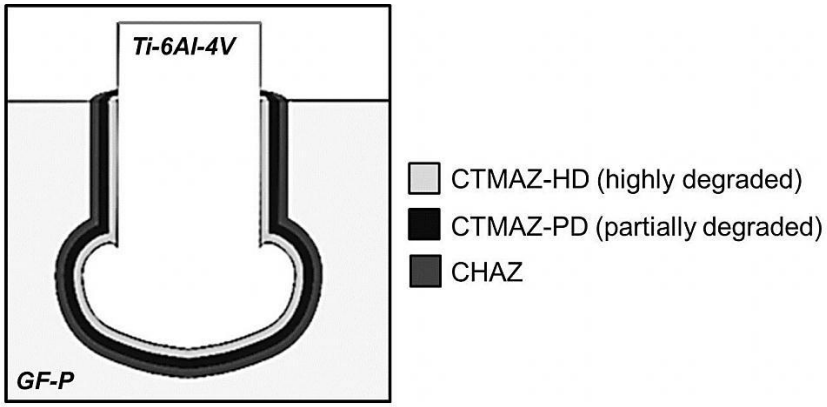

Figure 9. 18 Schematic representation of microstructural zones for a typical friction-riveted joint of glass fiber reinforced thermoset in this work.

9.5 Physicochemical Changes of Glass Fiber Reinforced Thermoset Polyester

The thermo-mechanical decomposition of GF-P in FricRiveting was observed for all specimens produced with the studied joining conditions. Consequently, the severity of the decomposition was investigated by DCS and TG analyses since the main decomposition mechanism of the matrix is through random chain scission (see Section 3.3.2). Samples from flash expelled during the rivet penetration were analyzed according to the procedure described in Section 5.11. Since process temperatures were above the onset degradation temperature of the polyester resin, it was expected that even the flash material from condition C1 - exposed to the lowest temperature, around 460°C - would suffer advanced decomposition steps. Thus, only the flash from condition C1 was tested and the results are presented in Figure 9.19-a and -b. The base material data (Figure 7.3 and 7.4) was included for comparison.

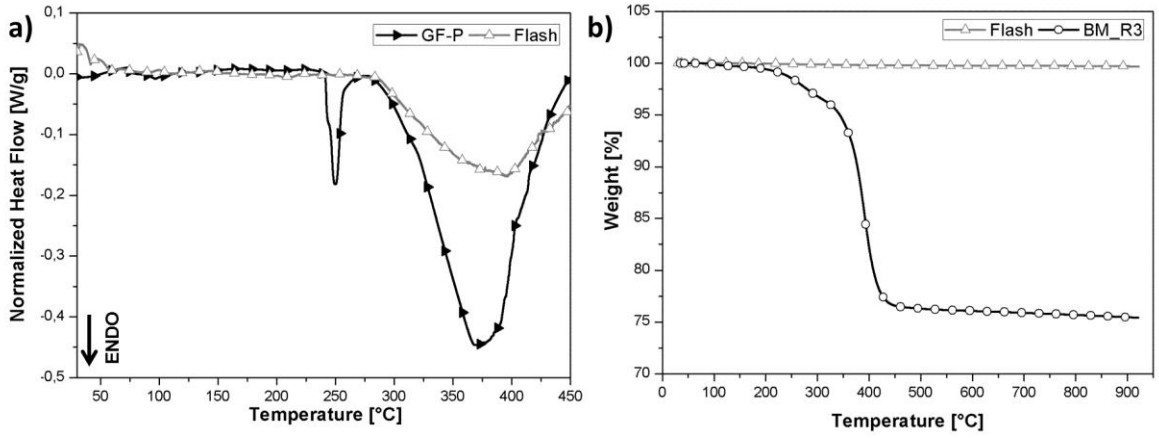

Figure 9. 19 a) DSC and b) TG curves of GF-P base material and the flash material expelled during the joining process (C1 joint: RS = 9000 rpm, FT = 1.0 s and FOT =1.2 s).

When compared to the GF-P base material, the DSC curve of the expelled flash (Figure 9. 19-a) showed a less intense endothermic peak at 300-450°C, relative to chain scission of polyester, and no additional endothermic peak corresponding to the flame retardant decomposition at 250°C. This is an

indication that polyester was partially decomposed and the flame retardant was completely consumed during the process. The TGA curve of the expelled flash (Figure 9. 19-b) shows no significant variation in mass loss compared to the base material which confirms the severe decomposition of polyester matrix and the formation of flash composed mostly by char material and broken glass fibers. Due to the presence of broken glass fiber in the flash, this material has high thermal stability at the temperature range evaluated, explaining the TGA behavior.

Complementary analysis through FT-IR was performed in order to confirm the degradation severity pointed out by the TGA and DSC methods. Figure 9.20 shows the characteristic absorption bands for GF-P base material and expelled flash. An example of the peak deconvolution procedure of IR spectrum is given in Appendix E. The IR-spectrogram includes the typical bands centered at 1728 cm^{-1} and at range of 1250-1100 cm^{-1} relative to stretching vibrations of carbonyl (C=O) and ester (C-O-C) groups, respectively [142]. According to Anderson and Freeman [86] and reported in Section 3.3.2, one possible thermal degradation mechanism of GF-P leads to the formation of either carbon dioxide and propylene or carboxylic acid, which should increases the absorbance of the carbonyl band and reduces the intensity of the stretching vibration band of the ester functional group. Nevertheless, no characteristic peaks could be observed in the flash spectrum (Figure 9.20), thus revealing complete degradation of the polyester matrix in the surroundings of the rivet. This is in accordance with the large amount of volumetric flaws in the CTMAZ.

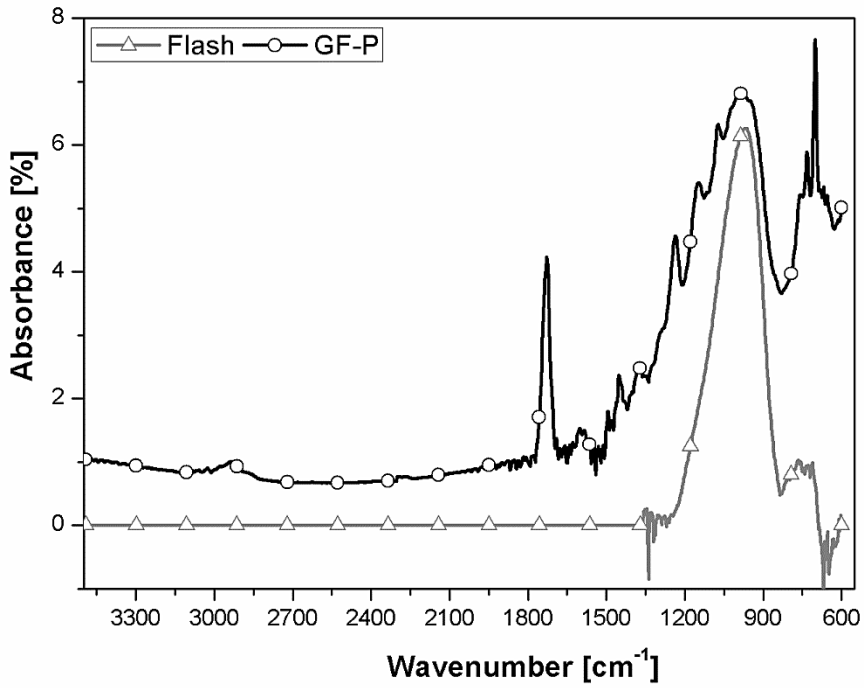

Figure 9. 20 Spectra comparison between the GF-P base material and the flash material (C1 joint: RS = 9000 rpm, FT = 1.0 s and FOT = 1.2 s).

As previously discussed, these effects owing to the intense thermomechanical regime cannot be completely eliminated but may be reduced by means of further process optimization.

10 JOINT QUASI-STATIC MECHANICAL PROPERTIES

10.1 Joint Local Mechanical Performance

The microhardness was used to evaluate local mechanical properties of friction-riveted joints. It has been shown in previous work [116] that microhardness distribution in friction-riveted joints is influenced by the process-related microstructural changes in the metal and composite, detailed in Section 9. The results for the metallic rivet were obtained in the form of Vickers hardness maps from one half of the rivet (due to symmetry), while for the composite part nanohardness was punctually measured in specific regions following the procedures described in Section 5.8. Figure 10.1 illustrates a typical microhardness mapping of the Ti-6Al-4V rivet in a friction-riveted joint. The regions identified by microscopy in Figure 9.2 could be seen in Figure 10.1 as well.

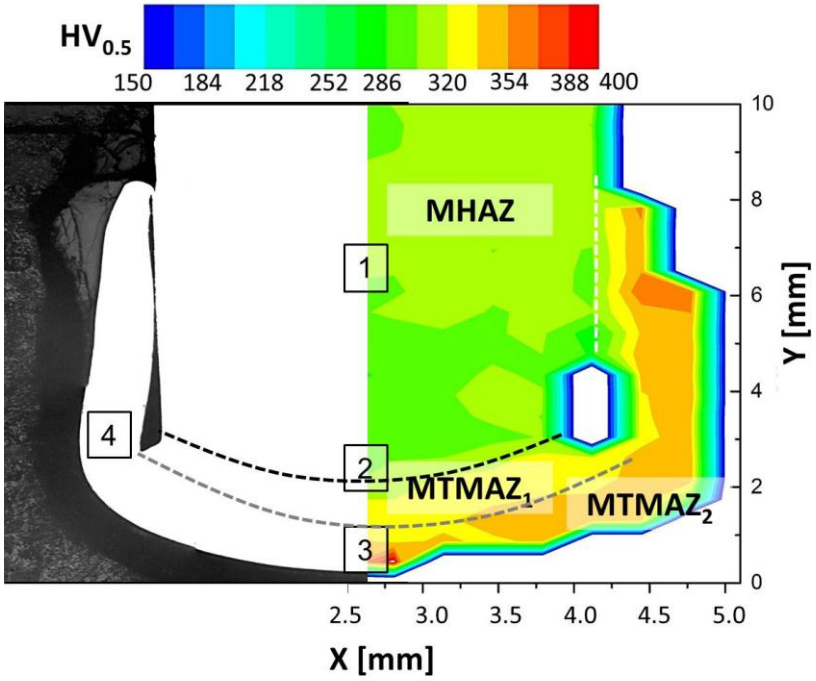

Figure 10. 1 Vickers microhardness distribution of the Ti-6Al-4V deformed rivet showing the microstructural zones in the rivet (joint produced under condition C2: RS = 9000 rpm, FT = 1.2 s and FOT = 1.2 s; $T_{p,C2\text{-}2}$= 703°C).

In the heat affected zone (MHAZ) (Region 1) the grain coarsening of the equiaxed microstructure provided decrease of 5-10% (HV_{MHAZ}= 286-269 HV) in microhardness in comparison to the base material ($HV_{Ti6Al4V}$= 300-320 HV). The high ductility and formability provided by the equiaxed microstructure with coarse β-grains explain this change [56]. Additionally, this microhardness decrease can be associated with annealing phenomena associated with static recovering (*i.e.* dislocation annihilation by climbing and cross-slipping), owing to higher temperatures (but below β-*transus* temperature) that the rivet was submitted [143]. This phenomenon was already reported to take place in the MHAZ of the AA 2024-T351 rivet joined with a PEI plate by FricRiveting [40].

The greater increase in microhardness was observed at the deformed rivet tip (rivet anchoring zone). The $MTMAZ_1$ (yellow area in the rivet tip, Figure 10.1) is a transition zone where a increase in microhardness in the order of 15-25% (HV_{MTMAZ1}= 320-337 HV) could be observed in comparison to Region 1. This can be related to the partial modification from equiaxed to acicular grains observed from the imminent needles in Region 2 to Regions 3 and 4 (Widmanstätten and martensite, Figure 9.2, Regions 2, 3 and 4). Similar behavior was observed by Esmaily *et al.* [67] who reported a hardness increase in the stir zone- the most thermo-mechanically affected zone- of Ti-6Al-4V welds produced by FSW.

Adjacent to $MTMAZ_1$ in Regions 3 and 4 is $MTMAZ_2$, depicted in Figure 10.1 by orange shades. The average hardness slightly higher than $MTMAZ_1$ (approximately 10%) showed an increase from 12% to 24% of the base material (HV_{MTMAZ2}= 337-371 HV). The formation of fully acicular microstructure with more refined lamellae in Region 4 can explain this increase. According to Esmaily *et al.* [67], when the welding was conducted above the β-*transus* temperature, the local mechanical properties increased with the welding speed because the lamellar size decreased as the cooling rate increased. The effect of quenching in Ti-6Al-4V also showed the formation of α'-martensitic phase, which increases the hardness up to similar values obtained in this work for $MTMAZ_2$ [144]. The contributions of single microstructural changes determining

the extension of microstructural zones is very complex. This quantification requires a deeper investigation; however is out of the scope of this work.

Figure 10.2 displays a comparison between the microhardness maps of metallic rivets for joints produced under the conditions investigated in this work. By increasing the energy input from C1 to C3, a similar hardening trend was observed through the rivet. Nevertheless, in C3 (Figure 10.2-c), the hardness increased considerably in the MHAZ (Regions 1 from Figure 9.2-a) and MTMAZ (Regions 2 and 3 from Figure 9.2-a), owing to the morphological changes described previously in Section 9.2. Therefore, the extension of acicular transformation in MTMAZ, was apparently much more evident for higher energy input (C3). In this case, the hardening effect of the thin needles seems to dominate a large volume of the rivet inserted in the GF-P plate.

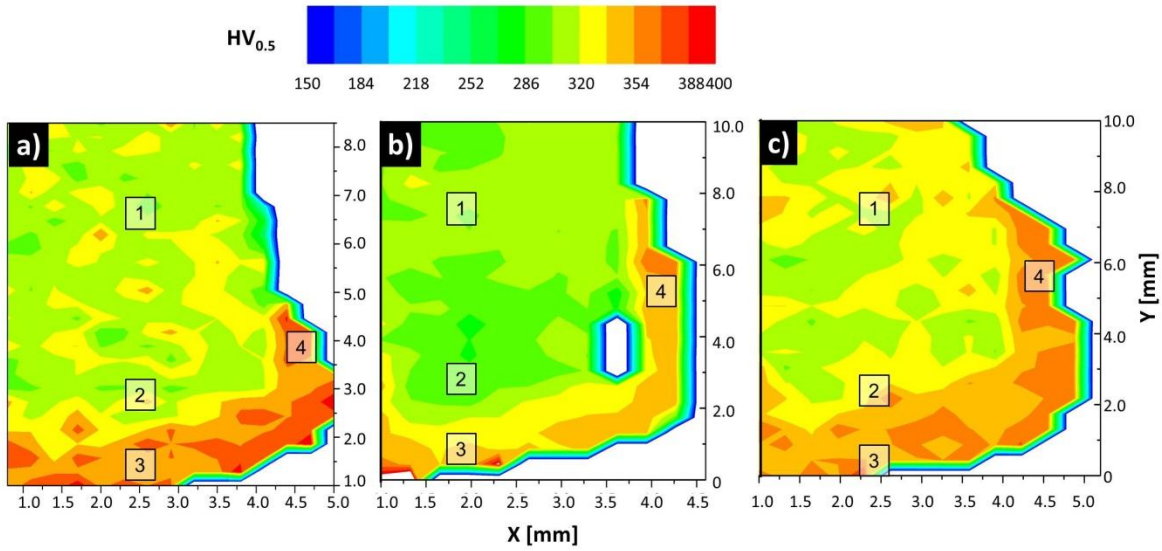

Figure 10. 2 Vickers microhardness maps of metallic rivet for the case-study joints. a) C1 (low energy input; RS = 9000 rpm, FT = 1.0 s; $T_{p,C1-1}$ = 320 °C); b) C2 (intermediate energy input; RS = 9000 rpm, FT = 1.2 s; $T_{p,C2-1}$ = 703 °C) and c) C3 (high energy input; RS = 10000 rpm, FT = 1.2s; $T_{p,C3-2}$ = 760 °C).

The effectiveness of the nanohardness measurement technique applied to investigate the local mechanical properties of the process-affected composite was assessed by analyzing the positioning of resultant indentations. Figure 10.3-a and -b shows smaller indentation sizes leading to a good safety distance between them (higher than height of the triangle mark established by standards

[100]). Since both glass interphase/glass fiber and thermoset polyester present brittle behavior [6] and indentation distance is large enough, one can expect that plastically deformed zones of indentations were not superimposed. None of the indentations presented additional cracks propagating from their edges which also indicates suitable load and holding time testing conditions [145].

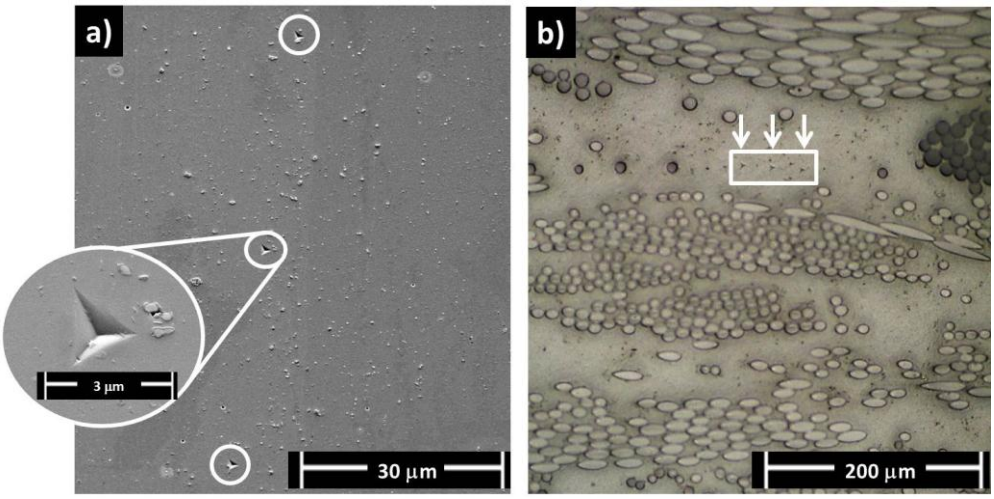

Figure 10. 3 Example of nanoindentations in the glass-interphase a) and GF-P composite, out-side the joining area b).

Figure 10.4-a shows the changes in the hardness through the visual composite thermo-mechanically affected zones (CTMAZ, Section 9.4) and in the polyester matrix of the GF-P base material. The analysis was performed for case-study (C1, C2, C3). The hardness of the composite material was measured by nanoindentations by following the procedure described in Section 5.8. This procedure was adopted to try avoiding or reducing the geometrical influence of the fiber in the indentation volume of interaction in the polyester matrix. The red dots in Figure 10.4-b illustrate the regions where hardness were measured.

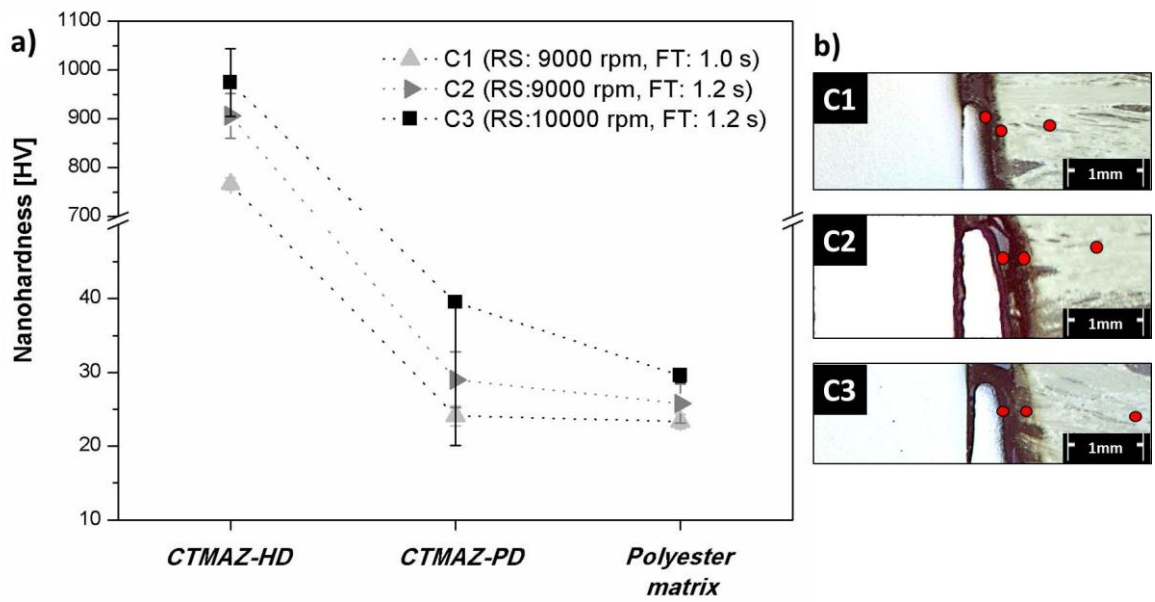

Figure 10. 4 a) Average nanohardness of GF-P from different zones in the joining area of comparative friction-riveted joints b) microstructure of the regions indented and identified by dots.

For all the joints, the glass layer formed in highly degraded composite thermo-mechaically affected zone (CTMAZ-HD, Section 9.4) led to high hardness values ($HV_{CTMAZ-HD}$ = 766-974 HV) followed by a drastically decrease in partially degraded composite thermo-mechanically affected zone (CTMAZ-PD, Section 9.4) ($HV_{CTMAZ-PD}$ = 24-39 HV) with average values laying slightly above the average local strength of the polyester matrix in the base material (HV_{BM} = 22-23 HV). The former observation was unexpected. The hardness values of CTMAZ-PD should be lower than the matrix base material, since it was highly degraded and the presence of a high amount of volumetric flaws- the source of augmented deviation in hardness in this region- was detected (Figure 9.17). A possible explanation would be fibers that were partially molten assuming the hard glass structure observed in the CTMAZ-HD. In general, no polymeric hardening phenomena, such as physical aging, are expected since process temperature overcame the glass transition temperature and onset degradation temperature of the polyester. The exact extension of the CHAZ could not identified by nanohardness analysis mainly due to two factors: the high concentration of volumetric flaws nearby the threshold between CTMAZ-

PD and CHAZ, which hinders the measurement of the local mechanical properties, and the sensitivity of the hardness measurement to the fiber presence in the indentation surroundings, which affects the precise distinction between the CHAZ and the composite matrix base material [145-146]. Comparing the effect of the energy input in the nanohardness changes of GF-P, the highest values for CTMAZ occurred for joints submitted to high energy input (condition C3) followed by the joints produced under C2 and C1 joining conditions. This may suggest lesser intensity of process-related changes weakening the glass formed (e.g. cracks formation).

10.2 Joint Global Mechanical Performance and Fracture Analysis

10.2.1 Quasi-static Loading Behavior of Friction–Riveted Joints

The lap shear testing, LSS (Section 5.9) was performed to evaluate the global mechanical performance of the joints produced under different energy inputs. The strong dissimilarity of the mechanical properties between the joining components in hybrid structure leads to the failure of the weakest part. Generally, the polymer/ polymeric composite in bolted [23] or friction-riveted [42] joints of thin parts fails catastrophically by net-tension, cleavage, pull-out or tear-out, which is not desired [25]. Owing to this limitation, joint geometry design is a powerful tool to predict the failure mode. For instance, by increasing the thickness of the composite plate, the area which bears the load is increased, the through-thickness effect becomes relevant and, therefore, the joint strength is optimized [147]. In this work, thick GF-P parts led to two combinations of failure modes: composite bearing followed by shear through of the metallic rivet with partial rivet pull-out (failure Mode 1) and composite bearing with full rivet pull-out (failure Mode 2). The bearing failure- a non-catastrophic failure type- is the initial failure mechanisms in both cases. In bearing failure of mechanically fastened composite joints [25], the rivet shaft interacts with the composite part creating a compression field which acts in the composite hole edge. This interaction can affect the brittle matrix and the fiber reinforcement through

delamination, formation of cracks in the matrix and kink bands decreasing the joint efficiency [25]. Figure 10.5 illustrates the typical behavior of metal-composite joints failing by Mode 1 during LSS test. Figure 10.5-a shows the force-displacement curve with location of details pictures (I-VI, Figure 10.5-b) corresponding to specific stage on the load-displacement curve.

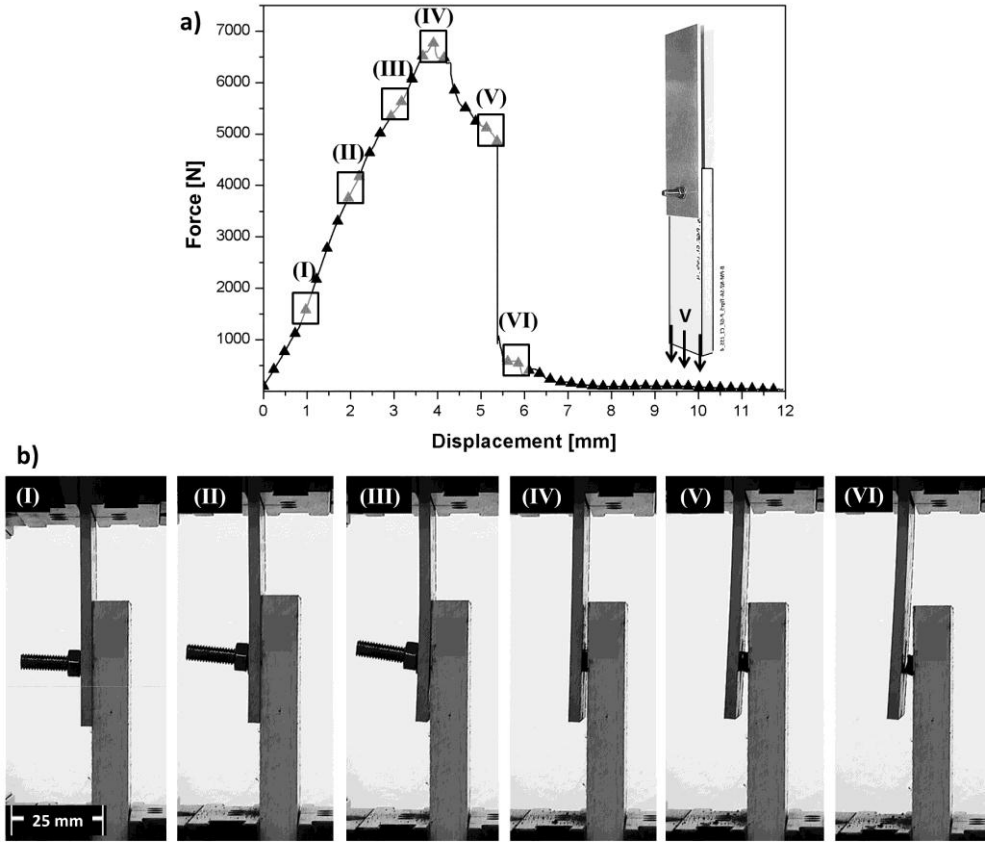

Figure 10. 5 Typical mechanical behavior of Ti-6Al-4V/GF-P friction-riveted joint under lap shear testing showing initial failure by bearing followed by through shear of the metallic rivet with partial rivet pull-out (Mode 1). a) Force-displacement curve with location of specific times on the curve represented by the sequence of pictures (Stages I to VI) in b).

Figure 10.5 shows initially Stage I, when the joint is elastically deformed and the force grows linearly with the displacement. As the deformation continues, the compressive field and frictional force acting in the hole edge in contact to the rivet lead to plastic deformation by bearing at the lower (GF-P plate) and upper (metallic gusset) plates. At this point, a non-linearity of the curve is observed (Stage II) [25]. In bolted pultruded thermoset composite, this

failure mode generally occurs when the ratio between the width (w) of the composite plate and the diameter (d_0) of the rivet is sufficiently high ($w/d_0 > 4$) [147]. The load is sustained for a certain period when the metallic plate (metallic gusset) begins detaching from the composite part due to secondary bending (Stage III). The secondary bending is a response of asymmetric stress distribution, which leads to out-of-plane bending of the joint [148]. Additionally, threads (for fixation of clamping nut) may increase the effect of stress concentration in the rivet shaft, acting as a notch and crack nucleation sites. When the local stresses increases above the strength of the rivet, the final failure propagates through shear of the rivet (Stage IV) and the force decreases abruptly. The fractured rivet portion remains partially anchored in the composite and inside of the through-hole of the gusset plate; it is progressively pulled-out from the composite plate in course of mechanical testing, while the gusset is further bended (Stage V). The load is transferred in this stage by friction from the interaction of the rivet with the walls of the gusset hole. The bending ends when the fractured rivet portion starts to slip and loses entirely the contact to the gusset plate (Stage VI).

Figure 10.6 displays the typical mechanical behavior for friction-riveted lap joints failing by Mode 2 (initial bearing followed by full rivet pull-out). Stages I to III exhibit the same behavior as Mode 1 failure, starting with elastic regime, followed by composite bearing damage and secondary bending of the gusset plate; secondary bending is partially responsible for the complete pull out of the rivet in Stage IV (Figure 10.6-b). Once the secondary bending partially removes the rivet, the clamping pressure decreases and the force is borne by friction between the rivet and the hole edges. At this point, bearing damages such as delamination and fiber kink bands may occur at the composite hole edge, strongly affecting the composite strength [149]. The local stresses eventually exceed the cohesive forces responsible for the joint integrity, occasionally widening the hole diameter (originally created by inserted rivet). Therefore, the rivet anchoring zone (deformed rivet tip) is removed. Rivet pull out starts to tear the composite surface, already damaged by the bearing effects (Stage V, Figure 10.6-b). Stage VI depicts the final test phase, when rivet is completed

removed from the composite part. As shown in Figure 10.6-a, joints failing by Mode 2 bear more plastic deformation (higher displacement at break) resulting in a non-catastrophic joint failure, which suggests that this failure mode is easier to predict than Mode 1. Further investigation is required to allow a better understanding and prediction of the failure modes identified in this work.

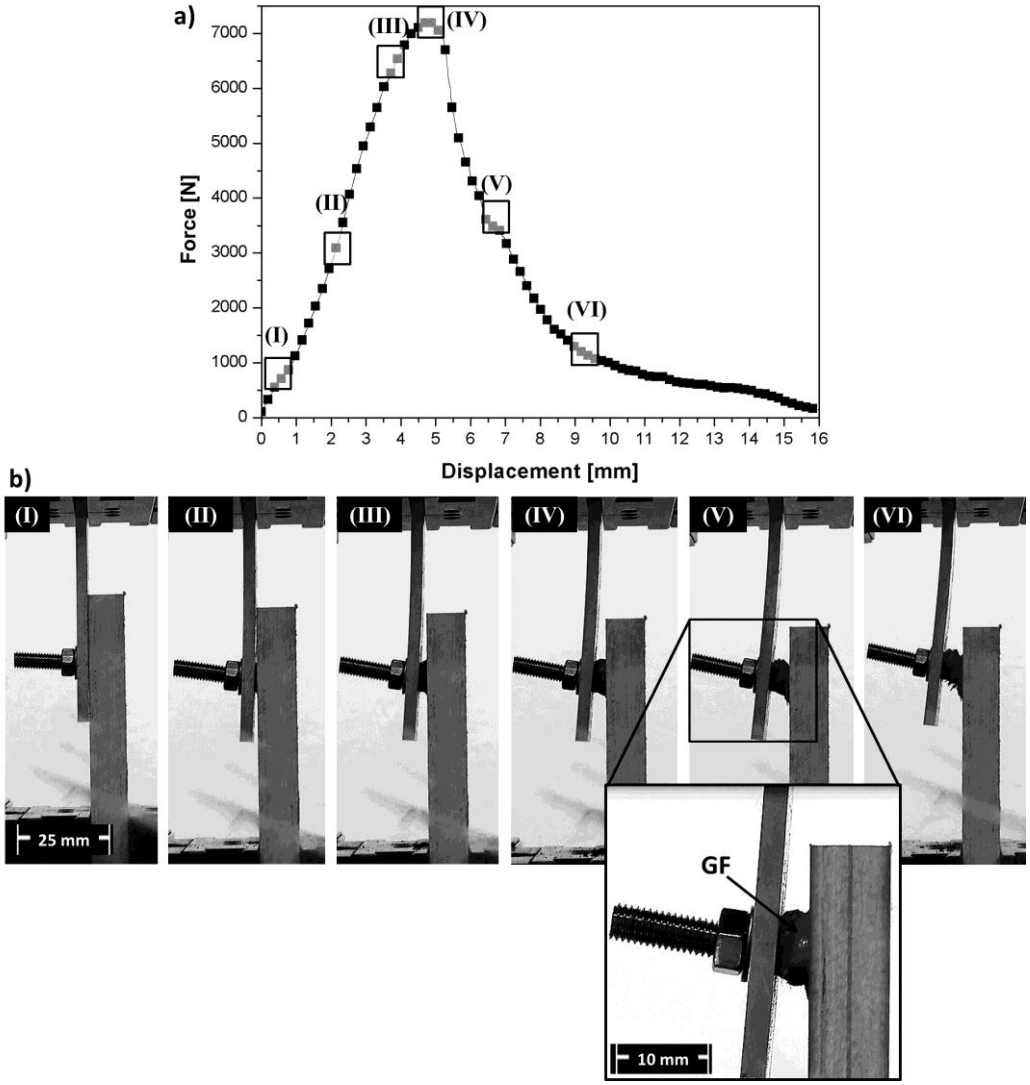

Figure 10. 6 Typical mechanical behavior of Ti-6Al-4V/GF-P friction-riveted joint under lap shear testing, showing initial failure by bearing followed by full rivet pull-out (Mode 2). a) Force-displacement curve with location of specific times on the curve represented by the sequence of pictures (Stages I to VI) in b).

The complexity of the failure types involved in friction-riveted lap joints of Ti-6Al-4V and pultruded thermoset composite makes the precise calculation of

the ultimate lap shear strength challenging. For the calculation of bearing strength, the initial failure mechanism observed in Modes 1 and 2, Amancio-Filho *et al*. [42], performed an attempt to estimate the strength of AA 2024/ PEI friction-riveted joints using the nominal strength concept, as addressed by ASTM D 5961 M-08 [105] for bolted joints and given by Equation 10.1. Altmeyer [48] used the same approach to determine joint strength in aircraft Ti gr.3/CF-PEEK joints failing by Mode 1. For this purpose, she considers that joint fails when bearing initiates, considering that through shear of the rivet failure is an end-stage failure mechanism; this is a typical approach used in aircraft design of riveted joints.

$$\sigma_{br} = \frac{F}{k.t.d} \quad (10.1)$$

σ_{br} is the simplified lap-shear strength which is a ratio between F, the ultimate lap shear force and the product of k, a force per hole force (1 for single riveted systems), t is the thickness of the plate, and d is the nominal diameter of the hole.

Blaga *et al*. [43] used an alternative approach to calculate ultimate lap shear strength in metal-glass fiber reinforced thermoplastic lap joints. The authors used an area A_d –the actual measured area of the hole created by the deformed rivet – to calculate ultimate lap shear strength. The authors compared the results with the nominal strength calculated by Equation 10.1, demonstrating a fairly good agreement between nominal strength and the actual bearing strength calculated with A_d. However, for the current specimens, the calculation of A_d is difficult considering the large amount of thermo-mechanically affected composite materials around the rivet. Considering that ultimate lap shear force (ULSF) for both failure modes in this study were laying within the range of bearing damage, Equation 10.1 was used to obtain the results of nominal ultimate bearing strength presented in Table 10.1. Typical force-displacement curves for the strongest and weakest joints of each joining condition are summarized in Appendix F.

Table 10. 1 Experimental data of replicated joints and nominal ultimate bearing strength of Ti-6Al-4V/GF-P friction-riveted joints.

	GF-P Base Material [38]	C1	C2	C3
ULSF (kN)		7.0	8.3	5.2
		7.15	8.0	5.5
		3.7	6.2	3.0
		5.1	4.0	3.6
		3.1	7.2	3.0
Average (kN)		5.2 ± 1.9	6.8 ± 1.7	4.0 ± 1.2
σ_{br} (MPa)	240	139	166	103
		143	161	110
		74	124	60
		101	80	72
		61	144	60
Average (MPa)		104 ± 37	135 ± 35	81 ± 24

All joints presented bearing strength between 30-70% of the base material bearing strength. This reduction was expected due to the inherent thermo-mechanical damage in the CTMAZ, as reported in Section 9.4. Joints produced under joining condition C2, with intermediate level of energy input, achieved higher average σ_{br} (135 ± 35 MPa) in comparison to C1 (104 ± 37 MPa) and C3 (81 ± 24 MPa). The reduced extent of the visual degradation in the joint area (as detailed in the Section 9.1) probably resulted in a slight better joint integrity for C2, leading to better bearing resistance. The anchoring efficiency attributed to the rivet penetration depth and the widening of the rivet tip appears to have lesser influence on the bearing joint strength than the effect of the degradation extent in the joint area (A), since all the conditions presented similar H and W (see Table 9.1 in Section 9.1). Differences in A, rivet tip plasticizing levels and hence, differences in geometries of the anchoring zone, may explain, in part, the high standard deviations of the strength data for joints produced under all case-study joining conditions (Table 10.1). Facing these high deviations, the two failure modes already described were identified for each case-study joint and plotted with their respective ultimate bearing strengths as presented in Figure 10.7.

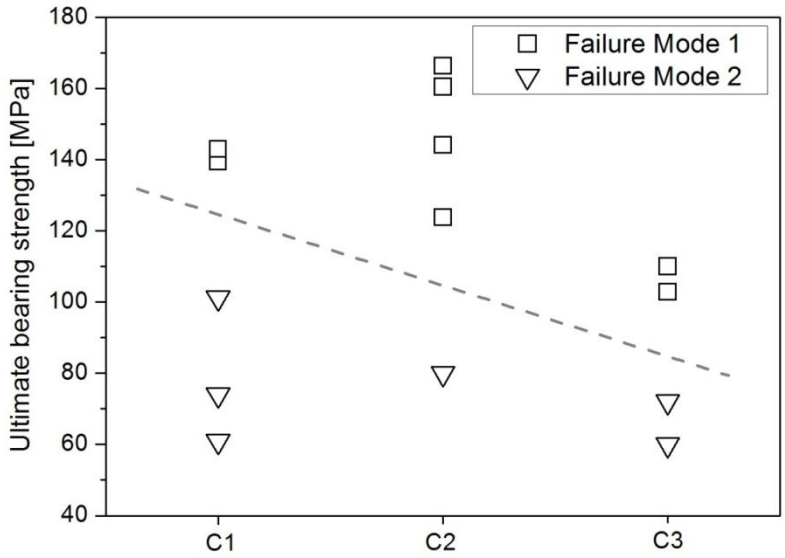

Figure 10. 7 Ultimate bearing strength and developed failure modes of case-study joints.

From the figure, the effect of the selected joining parameters (energy input) has apparently no correlation with failure type since both failure modes were identified for all case-study joints. This may be related to standard deviation of the visual thermal degraded area in the composite, considering that the geometry of rivet anchoring zones did not strongly varied within the studied joining conditions (Table 9.1, Section 9.1). However further studies of the correlation between these should be carried out through a deeper analysis, for instance by design of experiments and analysis of variance.

Additionally, a threshold bearing strength may be defined for each joining condition, above which failure changes from Mode 2 – composite bearing followed by rivet pull-out (weakest joints) – to Mode 1 failure - composite bearing and through shear of the rivet (strongest joints). This threshold point seems to decrease from C1 to C3 (trend shown by dashed line in Figure 10.7), indicating loss of load-carrying capacity of the strongest joints in the same manner. Although the energy input seems not to induce any preferential failure mode, this may influence indirectly the transition strength which dictates the occurrence of a given joint failure mode.

Therefore, the high standard deviations observed in the current study are considered to be mainly a result of the microstructural inhomogeneities of the

pultruded composite base material (Section 7), as fiber amount and distribution will change the dynamic coefficient of friction [83] influencing rivet insertion mechanisms. This will generate unstable heat regime and, hence, induce differential composite degradation extent (e.g. different CTMAZ extent) (Table 9.1) and rivet anchoring geometries (e.g. different rivet ‘leg’ geometries) (Figure 9.1) for replicates produced with a same joining condition. Thus, the mechanical anchoring and joint integrity will change increasing standard deviation of lap shear specimens.

Another possible issue, which may contribute to the higher standard deviation of mechanical performance is the applied torque. In this study a clamping torque recommended in the literature for thermoplastic composite-metal friction riveted joints was applied in the current specimens. No optimization of clamping torque was carried out in this work. This could have been done by following the procedure proposed by Altmeyer [48], who experimentally determined the undesired break-loose torque - the applied torque inducing the loosening of the rivet into the composite plate – to optimize clamping of lap joints. Bearing in mind the high level and inhomogeneity of thermal degradation at CTMAZ, the applied torque might have induced further damage to structure modifying joint strength. The development of reliable finite element model including failure criteria would be required to predict these damages and help to establish the proper level of clamping torque [23]. However this out of the scope of this master thesis.

10.2.2 Failure Analysis and Fracture Mechanisms of Friction-Riveted Lap Joints

Figure 10.8-a shows an example of a tested friction-riveted single-lap shear joints failing by Mode 1 and Figure 10.8-b by Mode 2. As described in Section 10.2.1, the critical stresses for both failure modes seem to be a radial bearing stresses induced by the compression at the contact between the rivet and the formed hole edges. The features highlighted by dashed lines in Figures 10.8-a and -b show evidences of a severe delamination in the composite

surface. Moreover, composite attached to the pulled-out rivet was depicted by black square in Figure 10.8-b, probably resultant from the composite surface tearing explained for Mode 2, in Section 10.2.1.

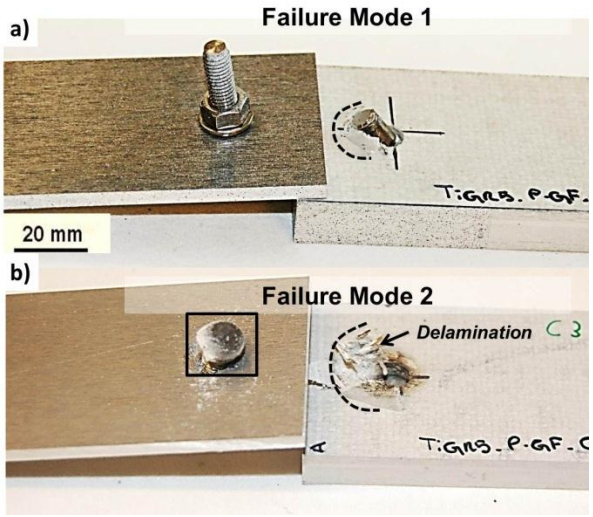

Figure 10. 8 Fractured friction-riveted joints showing the two main failure modes.

Figure 10.9-a illustrates the aspects of partial rivet removal (Stage IV, Figure 10.5-b) of a fractured joint failing by Mode 1 after the failure by through shear of the rivet (crack path indicated by a white arrow in Figure 10.9-a). The yellow dashed-lines squares mark the position of the magnified views provided in Figure 10.9-b and –c. Probably, the bottom of the metallic anchoring zone is initially detached from the hole edges by adhesive failure between the glassy interphase (CTMAZ-HD, Figure 9.17) and the damaged composite (CTMAZ-PD, Figure 9.17), where high amount of defects are located. Furthermore, it can be seen that hole edges of the composite part were damage by the rotation and slipping of the rivet undeformed shaft and anchoring zone. It is possible to observe composite surface delamination (yellow arrows in Figure 10.9-b), crushing of the matrix (yellow arrows in Figure 10.9-c), fiber bundles breakage and fiber buckling (yellow dashed arrows in Figure 10.9-c) related to high compressive forces experienced by the composite from the interaction with the rivet. These are the main Mode 1 damage types taking place in the composite during lap shear testing.

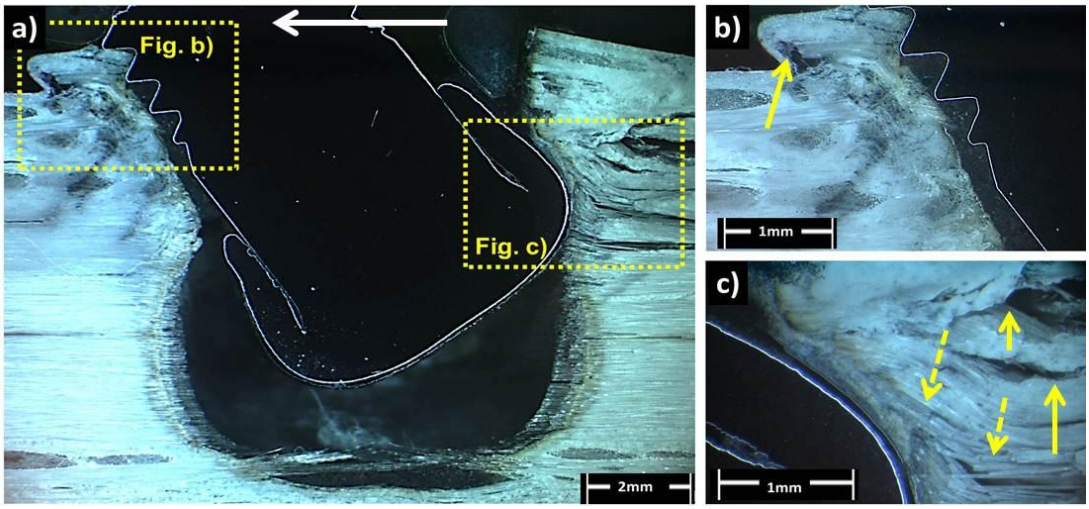

Figure 10. 9 A) Stereo micrograph of a typical Mode 1 fractured lap shear specimen in this work. Detailed views of damage at the upper surface of the composite part b) and c) damage of composite due to the rotation and slipping of the rivet anchoring zone.

The fracture surface of Mode 1 friction-riveted joint was analyzed in order to understand its micro-mechanisms of final failure. Figure 6.45 shows examples of fracture surface and details of the sheared rivet for the case-study joints. The final fracture took place at loading bearing rivet threads embedded into the composite plate. The reduction in diameter at the thread flight bottom concentrated stress nucleating a crack. Joints from condition C1 (Figures 10.10-a and –d) and C3 (Figures 10.10-c and –f) displayed cracks apparently propagating through a 0°- plane perpendicular to the rivet longitudinal axis. Moreover, these fracture surfaces shows the presence of intergranular fracture, indicating a brittle failure [150]. The texture arising from the extrusion process evidenced in the microstructure of the rivet base material (Figure 7.1) can explain this behavior [150]. The possible presence of undesired elements (*i.e* .hydrogen and oxygen) dissolved in the metal during Ti-6Al-4V rivet fabrication may embrittle Ti alloy, deteriorating its fracture resistance [151]. On the other hand for specimens produced under condition C2 (Figures 10.10-b and-e), where intermediate frictional energy was generated during the joining process, the failure was ductile with characteristic dimples in the metallic surface [152].

These dimples were elongated and oriented in the load direction. The stepwise-crack path followed a 45°- plane direction, approximately, over different flights of threaded components. The presence of dimples indicates high elastic and plastic deformations borne by the rivet under shearing; it could explains the high strength of joints produced under condition C2 (Figure 10.7) failing by Mode 1, in comparison to the ones produced under C1 and C3 joining conditions failing by the same mode.

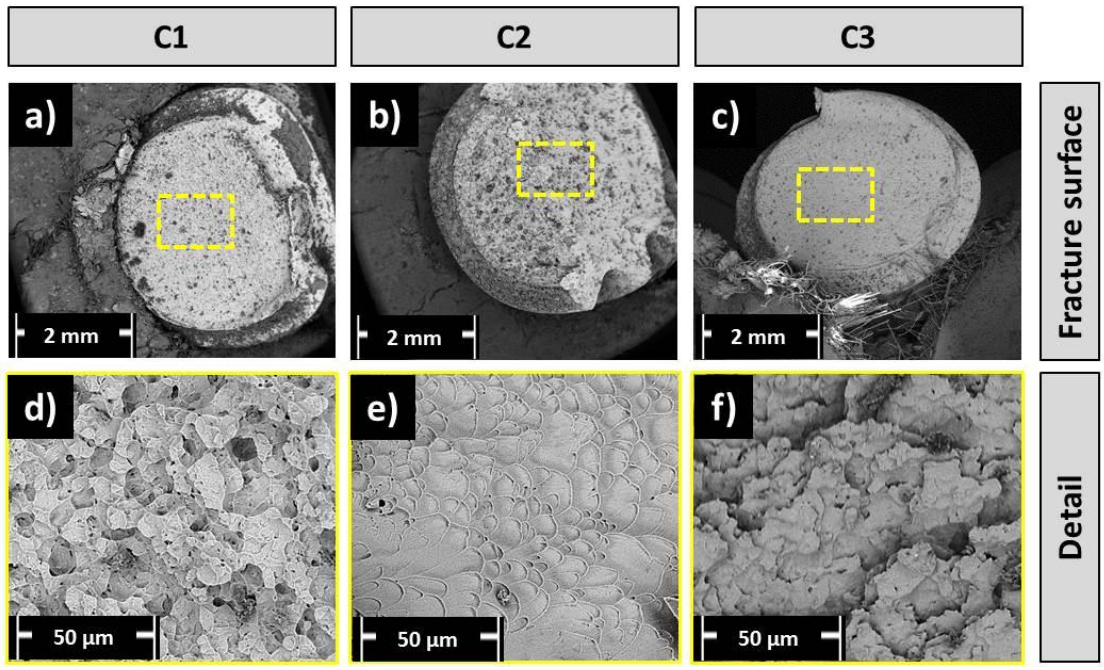

Figure 10. 10 SEM images of Mode 1 rivet fracture surfaces of Ti-6Al-4V/GF-P friction-riveted case-study joints. Figures a to c are the overview of the fracture surfaces while figures d to f are details of regions marked with yellow dashed squares.

From Figure 10.10, it is clear that further investigations should be performed to understand the differences among the samples and joining conditions to establish which micro-mechanisms of fracture control the rivet failure.

Figure 10.11 displays the bottom surfaces of rivets removed from the composite from specimens failing by Mode 2. The presence of a consolidated glass layer- the interphase composed by molten and softened glass fibers-

adhered to the metallic surface was evident for all case-study joints. As discussed in Section 9.3, this layer has a better adhesion with the metallic surface and weaker interaction with the composite affected volume. The interface between the glass layer and the composite has substantial presence of volumetric defects which are sites prone to crack nucleation leading to final fracture over this interface. This adhesion failure between glass interphase and damaged composite volume facilitates the removal of the rivet from the composite hole. In this way, the adhesive forces between glass interphase and composite appear to be an important mechanism for the development of failure Mode 2.

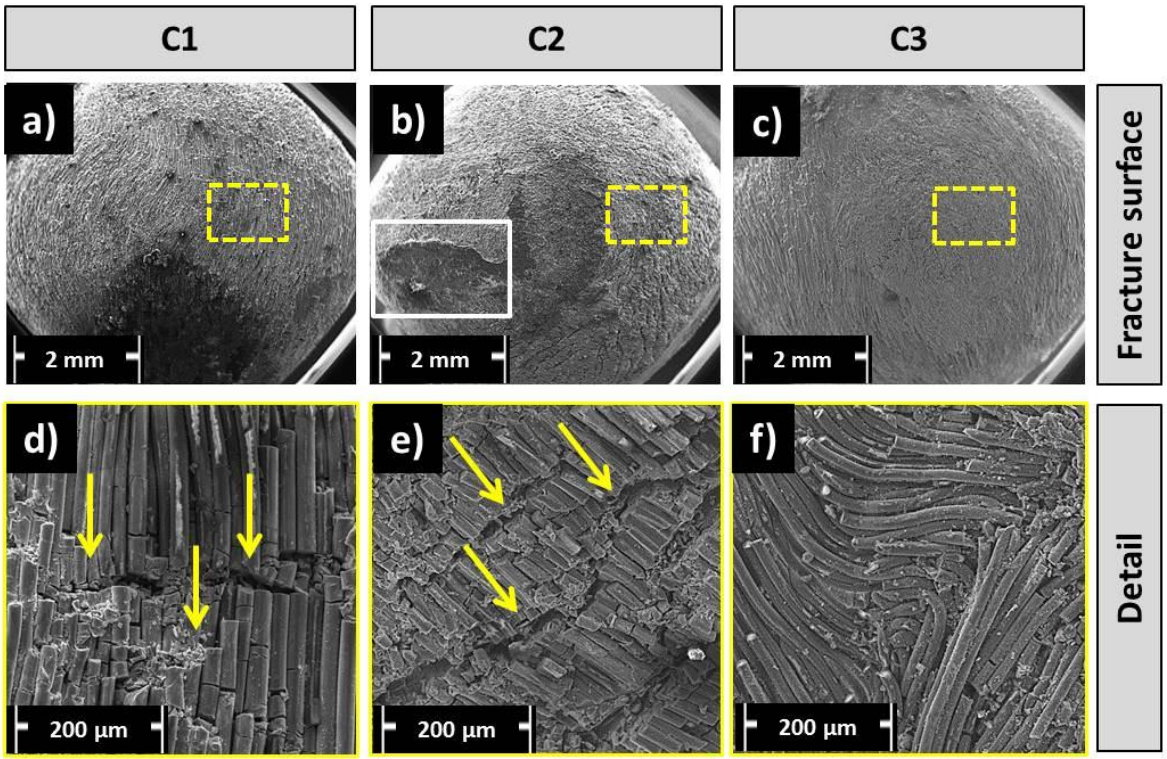

Figure 10. 11 SEM images of Mode 2 rivet fracture surfaces of Ti-6Al-4V/GF-P friction-riveted case-study joints. Figures a to c are the overview of the fracture surfaces while figures d to f are details of regions marked with yellow dashed squares.

By comparing the joints produced under different joining conditions, once the energy input raises (and consequently the process temperature, Figures 8.1 and 8.2) from C1 to C3, the fibers attached to the glass layers are visually

affected by the heat. For C3 joints (Figures 10.11-c and –f) undergoing the highest process temperature, the fibers were visually more softened and reoriented in the direction of material flow which followed the rivet rotation than C1 (Figures 10.11-a and –d) and C2 (Figures 10.11-b and –e) joints. Moreover, less broken fibers could be observed for C3 joints, as additional indication that the fiber bundles experienced higher softening temperatures than C1 and C2. For C1 and C2 joints, the smaller softening state of the fiber bundles (higher brittleness) probably made them more prone to the rivet shearing motion, rupturing during FricRiveting (see arrows in Figure 10.11-d and –e).

In some fracture specimens a partial breakage of the glass layer from the rivet surface can be seen, as it is highlighted by the white square in Figure 10.11 and observed into details in Figure 10.12. This suggests a combination of adhesive (glass layer- damaged composite interface) and cohesive (into the glass layer) failures. The mixture of adhesive and cohesive failure modes was described by Goushegir *et al*. [117] for lap-shear tested hybrid AA2024/CF-PPS joints produced by Friction Spot Joining. According to the authors, the region susceptible to cohesive failure and partial fiber breakage is where the intimate contact between the polymer matrix and the fibers with the plasticized metal occurs [117]. Amancio *et al.*[39] also evidenced this complex failure mode for hybrid friction-riveted joints of aluminum and unreinforced polyether imide under tensile loading. From the current understanding, the presence of process-related volumetric defects (Figure 9.12) and cracks (Figure 9.16-b) in the glass interphase probably led to the deterioration of the material and favored the partial crack nucleation and propagation through this region (cohesive failure). It is believed that the cracks deviate from the cohesive failure zone to the glass layer-composite interface where high amount of defects are located creating the identified pattern.

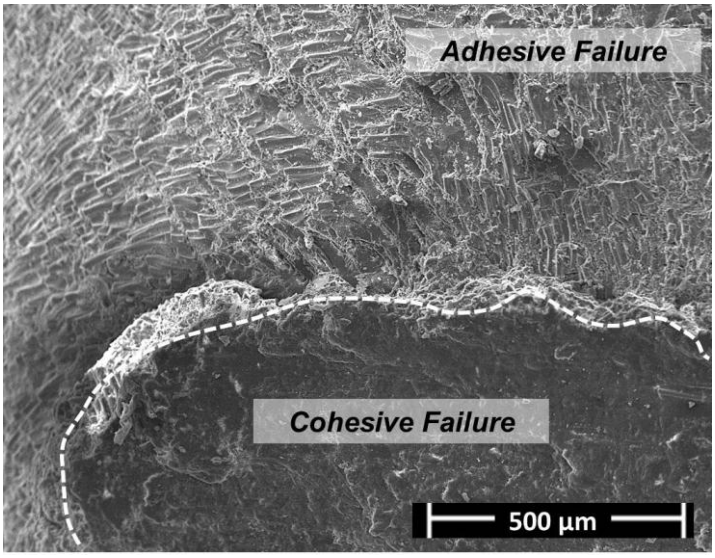

Figure 10. 12 SEM image of detailed region presented in Figure 10.11-b showing a combination of adhesive and cohesive failures.

In order to confirm the hypothesis of cohesive-adhesive failures mixture, the analysis of the key-hole from the Mode 2 fractured specimen from Figures 10.11-b and –e was carried out and the results presented in Figure 10.13. Figure 10.13-b is the A-A cross-section overview indicated in Figure 10.13-a and shows detailed areas through yellow dashed squares. These areas are depicted in Figures 10.13-c to-h.

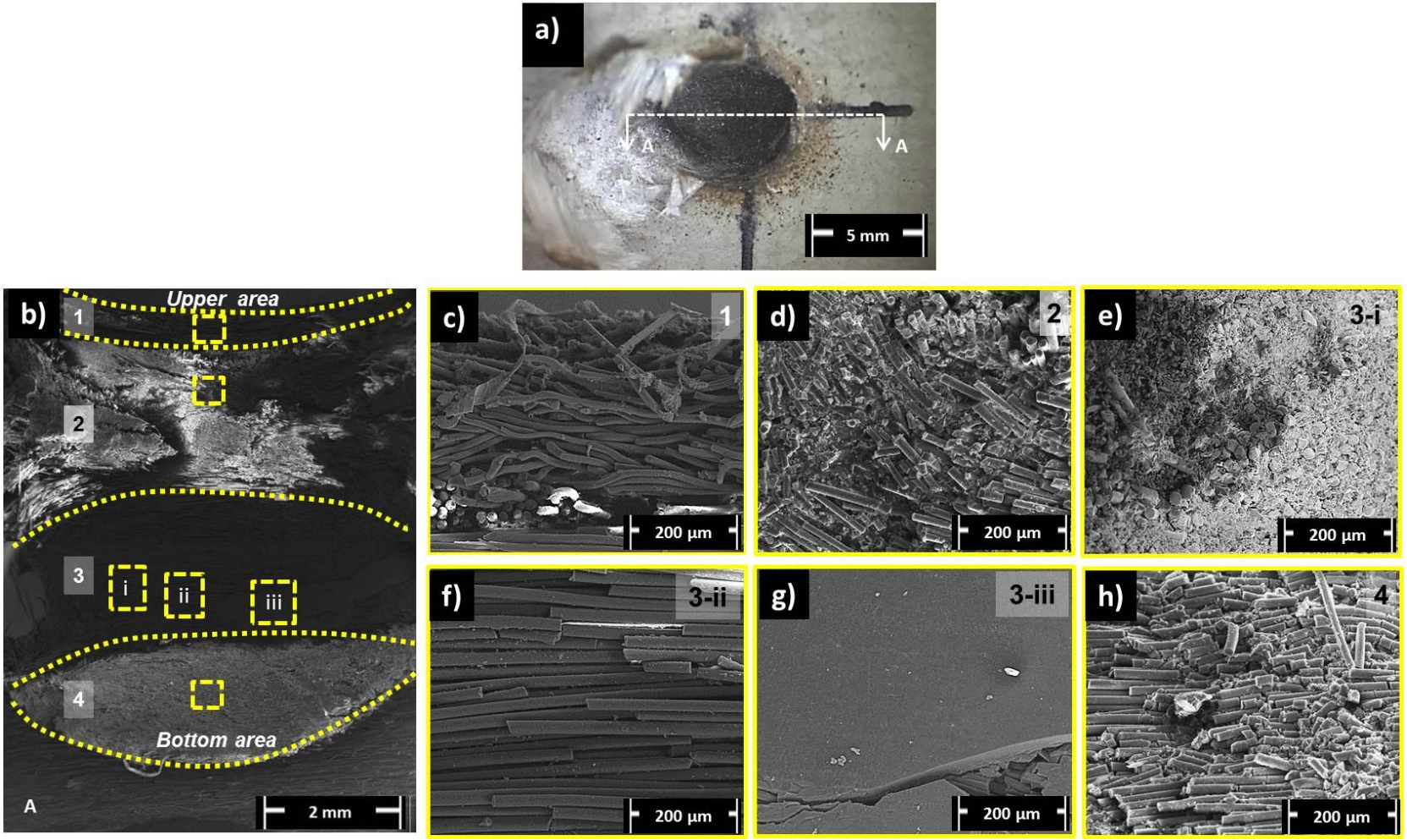

Figure 10. 13 a) Upper view of the key-hole from Mode 2 fractured specimen from Figure 10.11-b. b) Cross-section of the key-hole showing regions of interest which are detailed in figures c to h.

The magnified cross-sectional view (A-A Figure 10.13-a and-b) of the key-hole shows four distinct fractographic zones from the key-hole upper area (Region 1) to the key-hole bottom (Region 4), the region originally into contact with the rivet anchoring zone. In Region 1 (Figure 10.13-c), where fibers were oriented perpendicularly to the rivet insertion path in the upper layer of the composite, less fiber damage was observed, since probably the widening of the original formed hole (see Section 10.2.1) limited the intimate contact between the rivet and key-hole upper edge. In Region 2 (Figure 10.13-d), placed near to the key-hole upper area, the key-hole edge was highly damaged by the pull out motion of the rivet. The fibers were reoriented upwards in the direction of the rivet pull out. The brittle behavior of the glass fiber reinforcement led to high level of fiber breakage. Region 3 (Figures 10.13-e to -g) – the region where the larger diameter of the rivet anchoring zone was originally located - has different features, including a rough fracture surface area (Figure 10.13-e), unmodified fibers (Figure 10.13-f) and a smooth and discontinuous phase attached to the composite (Figure 10.13-g). Chemical composition analysis (see Appendix G) of this phase was obtained by EDS analysis. The main elements detected were silicon, calcium, aluminum and oxygen, typically found in glassy layer and in the glass fiber bundles (Section 9.3). From the EDS analysis and fracture surface aspects, a complex mixed cohesive-adhesive fracture mode took place between the rivet and glass interphase layer, and between the former and thermally affected composite volume. In this region, the rivet tip widening probably led to a compressive field creating an intimate and strong contact between the glass interphase and the composite at this spot hindering the complete detachment of the glass layer from the key-hole edges. Finally, Region 4 is the initiation crack zone (Stage IV, Figure 10.6) where rivet pull-out failure happens. In this region the fiber bundles were severely damaged by the high imposed shear rate and failure appears to have occurred at the interface composite-glass interphase (Figure 10.13-h).

In summary the micro-mechanisms of fracture in Mode 2 are very complex and dependent of the extension of fiber damage and formation of the glass interphase. From the current knowledge generated from this work, it is

possible to conclude that adhesive-cohesive failure at the CTMAZ and glass interphase seems to dictate crack nucleation and propagation in the rivet pull out process.

11 CASE STUDY: FRICTION-RIVETED GF-P EMERGENCY BRIDGE

Prior to the investigation of FricRiveting on the structural design of case-study GF-P emergency bridge, the mechanical performance of Ti-6Al-4V/GF-P friction-riveted coupon joints was compared with conventional bolted joints. Bolted lap-shear specimens were produced with the same geometry and materials used in friction-riveted joints and tested according to the same standard, as detailed o Section 5.9. A through-hole 5 mm in diameter was carefully produced in the GF-P plate to avoid delamination, 5 mm diameter Ti-6Al-4V bolts, with 60 mm in length with a similar threaded-plain geometry to the rivet (M5-threaded with 40 mm length and 10 mm plain length for the portion inserted in the composite region). Stainless steel M5 nuts and washers were also used to clamp the joint applying clamping torque of 5 Nm. Three replicates were tested. Figure 11.1 shows a bolted lap-shear specimen before (Figure 11.1-a) and after (Figure 11.1-b) lap shear testing.

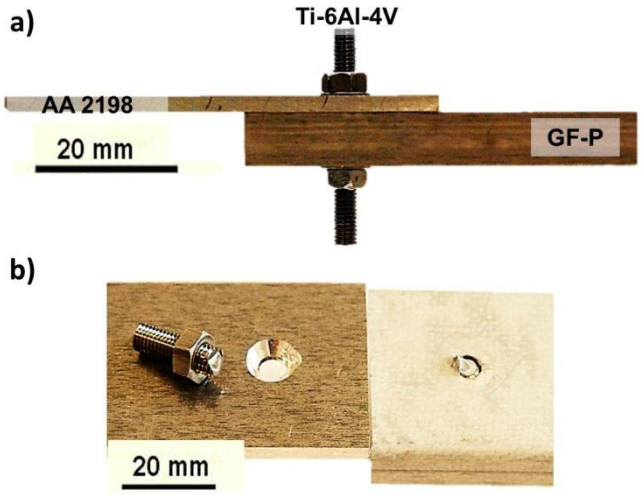

Figure 11. 1 a) Specimen configuration of single overlap bolted joint for Ti-6Al-4V/GF-P/AA 2198; b) overview of the fracture surface of a typical bolted joint.

Figure 11.2 compares the average mechanical strength of friction-riveted joining conditions with bolted joints. An average ultimate lap shear force (ULSF) of 8700 ± 500 N was achieved for the bolted connections, corresponding to ultimate lap shear strength (ULSS) of 174 ± 10 MPa. All bolted specimens failed through shear of the metallic rivet as shown in Figure 11.1-b. The friction-riveted

lap joints investigated in this work have decrease penalty of 20-50% in average strength in comparison to bolted lap joint strength. Joints produced under C1 joining condition presented average ultimate bearing strength of 104 ± 37 MPa, while C2 joints were the strongest joints bearing 135 ± 35 MPa, and C3 the weakest joints, with 81 ± 24 MPa.

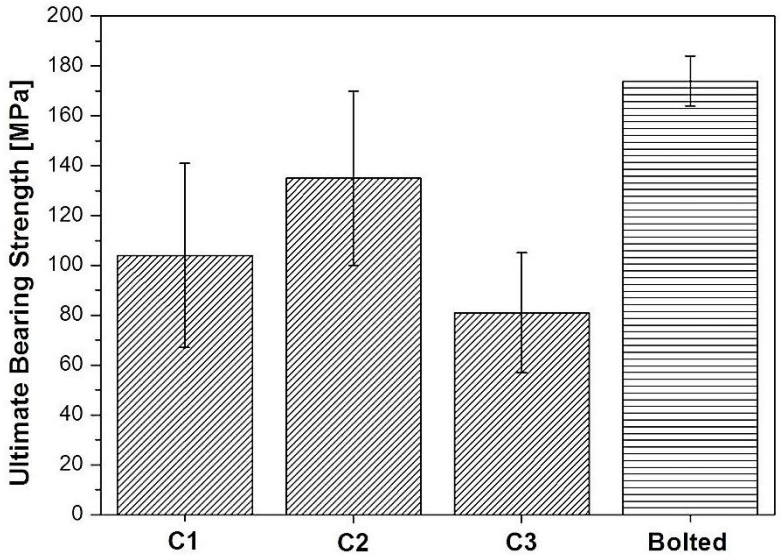

Figure 11. 2 Average lap-shear strength of comparative Ti-6Al-4V/GFP friction-riveted and bolted joints.

The strongest friction-riveted specimens produced under joining condition C2 achieved bearing strengths of 166 MPa (Table 10.1) which is within the standard deviation of bolted joints strengths (174 ± 10 MPa). This is a positive result in the engineering point of view. Blaga *et al.* [43] reported similar study comparing friction-riveted and bolted lap joints on thermoplastic glass fiber reinforced composite. They applied design of experiments to optimize FricRiveting joint lap shear strength, leading to values equal or better than the respective bolted joints.Therefore one may expect that the increasing maturity of FricRiveting for thermoset composites may improve joint mechanical performance making improvements on the competitiveness of the process in comparison to state-of-the-art techniques.

The development of the FricRiveting for joining thermosetting composite profiles is based on the widely application of these materials in structural applications, such as bridges [38]. Currently, bolted joints should be carefully designed due to the stress concentration issue at the surrounding of the hole (usually intrinsic to thermoset composites) and the weakness of the composite under out-of-plane loads [23]. Thus, FricRiveting was proposed as an alternative method to be used in civil infrastructures. Blaga *et al.* [43] firstly proposed civil engineering concepts and basic structural calculations for hybrid titanium grade 2 (Ti gr.2) and glass fiber reinforced polyether imide (GF-PEI) friction-riveted joints. The authors studied these FricRiveting-based joints to model the structural performance of nodes of GFRP truss emergency bridges. From their analysis they found a number of 162 5 mm diameter rivets necessary for nodes of 25 m-span Warren truss vehicular bridge (Figures 11.3-a and -b), assembled with U- and square composite profiles, which is comparable to classical riveted steel bridge nodes. The authors considered pre-friction-riveted profiles and perforated metallic gusset (Figure 11.3-b) to assemble the nodes. All details and the calculations can be found in [43].

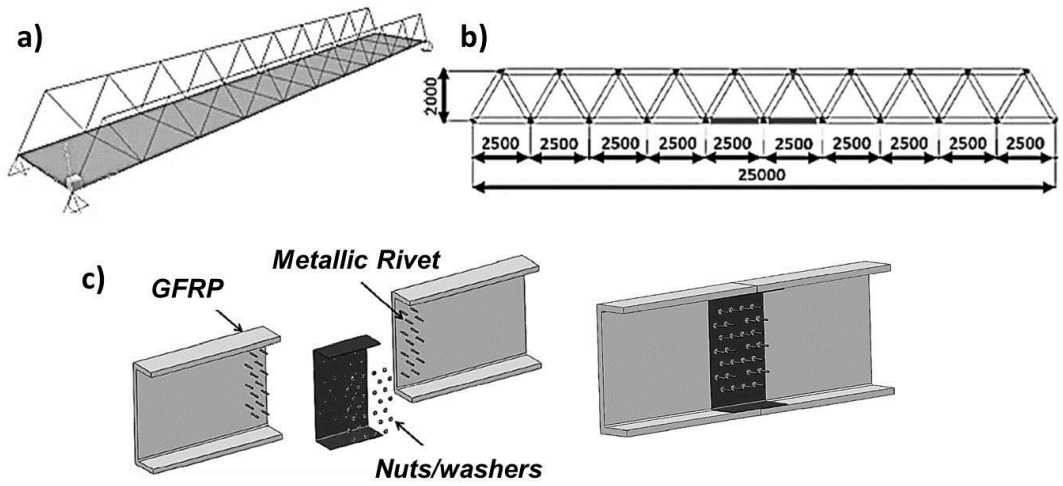

Figure 11. 3 a) Isometric view of the GF-PEI truss bridge proposed by Blaga *et al*; b) static model of the bridge; c) schematically view of the assembly on GFRP/metallic rivet/metallic gusset friction-riveted joints used in the structural truss bridge model (Adapted from [43]).

By following the same approach proposed by Blaga *et al.* [43], the number of rivets necessary for hypothetic Ti-6Al-4V/ GF-P hybrid structure assembled though the weakest and strongest friction-riveted joints produced under joining condition C2 was calculated using Equation 11.1, from Eurocode EN 1993-2; 2010 [153].

$$n \geq \frac{F}{\min\ (F_{V,Rd};F_{b,Rd})} \quad (11.1)$$

where n is the number of rivets, F is the force to be transmitted by the node (established in 760 kN for the bridge node modeled in [43]), $F_{V,Rd}$ is the shear resistance (in N) when rivets fail through shearing and $F_{b,\ Rd}$ is the bearing resistance (in N) when the major failure mode happened by bearing in the composite. The calculation was performed using the values of 4.0 kN and 8.3 (Table 10.1) from joining condition C2, the strongest case-study joining condition in the current investigation. Since all case-study joints failed initially through composite bearing, this value corresponds to the $F_{b,Rd}$ in Equation 11.1, the minimum value between the $F_{V,Rd}$ and $F_{b,Rd.}$ Numbers of 190 and 92 rivets (5 mm diameter) were necessary for a hypothetical Ti-6Al-4V/GF-P riveted assembly, which represents, in the best case, a reduction of 43% in comparison to the Ti gr.2/PEI structure in [43]. The stronger T-6Al-4V rivets (910 ± 1 MPa) (see Figure 7.1, Section 7.3) in comparison to Ti gr. 2 rivets (344 MPa) [150], the thicker GF-P plates (10 mm) in comparison to the GF-PEI plates (6.2 mm) and the less extended degraded area in the joining area probably led to better stress distribution through the composite thickness and consequently better node mechanical performance, reducing the required number of joints.

The results showed the promising application of the process in real structures, which are already made of the thermosetting composite investigated in this work. However, in both cases, the stress distribution over the rivet array is difficult to be estimated precisely by coupon testing, which suggests further analysis by up-scaling effect analysis, finite element modeling and joint design. These investigations are not within the scope of this work.

12 NEW INSIGHTS ON FRICRIVETING OF PULTRUDED FIBER REINFORCED THERMOSET COMPOSITE

FricRiveting of fiber reinforced thermoset, firstly presented in this work, has arisen new insights and issues previously not reported in the literature. As pointed out in Section 8.1, no viscous contribution attributed to the polymeric matrix is expected on the heat generation and joint formation since the thermoset does not melt. In opposition to metal-thermoplastic friction-riveted joints, the most important thermal property related to the thermosetting composite is the degradation behavior. As evidenced in this work, the degradation was intrinsic to the process (Section 6.2.3 and Section 6.2.4). However, at high extension, the effect was negative for the joint mechanical performance. Although the thermal degradation may also occur in a lesser extent for metal-thermoplastic friction-riveted joints [45], the transition temperatures such as T_g (for amorphous thermoplastic) and T_m (for semi-crystalline thermoplastic) play a more relevant role, since the lower viscosity of the polymer favors the metallic rivet insertion and deformation.

As already addressed by Blaga [12] and Altmeyer [46], the presence of continuous thermal resistant reinforcement, such as glass and carbon fiber woven, introduces another variable to the FricRiveting process. The fiber network works as a physical barrier to the rivet insertion. Thus, high levels of joining pressure (or joining force) and rotational speed are required to break the fibers and deform the rivet into the composite substrate. Furthermore, in the case of pultruded composites, the inhomogeneity of fiber content and orientation through the composite thickness (see Section 7.1) led to an unstable frictional regime. This behavior was evidenced by the torque monitoring (see Section 8.3). For thermoplastic, decrease in torque can be associated to decrease in polymeric viscosity, while for thermosetting composite it was explained as either regions with less fiber content or decrease in the molten viscosity of glass interphase (see Section 9.3). Process temperatures nearby the glass fiber soften/melting temperature (approximately 800°C) were achieved, which confirmed changes in the glass fiber rheology (see Section

8.2). Additionally, the unstable frictional regime during FricRiveting of thermoset GF-P represents non-uniform heat generation which can compromise the symmetry of the deformed rivet tip, the microstructure of the metal and the severity/extent of the composite degradation. Therefore, other uncontrolled variables must be considered in the physical description of metal/fiber reinforced thermosets friction-riveted joints, besides the influence of the joining parameters on the joint formation and mechanical performance. For instance, the fiber stacking sequence seems to be an influent additional variable to FricRiveting of pultruded thermoset composites since it destabilizes the heat generation and eventually leading to significant standard deviations on joint geometry (Section 9.1) and mechanical performance (Section 10.2).

Finally, the heat generation in FricRiveting of pultruded GF-P composites has apparently both contributions: solid friction between metal/composite/broken fibers – probably the major contribution – and viscous dissipation attributed to the shearing of the molten glass. A better understanding of the effect of each physical phase on the heat input and joint formation could be assessed by carefully analyzing the joining monitoring curves through stop-action method (abrupt stopping of the machine in different stages of the process to analyze different joint formation steps). By using such approach, it is possible to split the process in several steps during the frictional and forging phases and precisely investigate the joining parameters/variables (RS, JP and axial displacement) and, indirectly, the glass interphase formation and rivet deformation regime. Based on this considerations, the analytical model for heat input of FricRiveting for thermoplastics proposed by Amancio-Filho [39] should be adapted for thermosetting composites. The modification should consider the use of dynamic instead of kinematic coefficients of friction, and the glass interphase viscosity. These proposed analyses were not within the scope of this work but are essential for a better process understanding and should be carried out in future works to confirm the assumption discussed above.

13 SUMMARY OF RESULTS AND CONCLUSIONS

The feasibility of FricRiveting was, for the first time, thoroughly investigated for the challenging material combination of pultruded glass fiber reinforced thermoset polyester and Ti-6Al-4V alloy. The objectives addressed within the scope of this work were the fundamental understanding on Friction Riveting physics for metal- pultruded thermoset composite joints, establish the correlation between the process, microstructure and mechanical properties of Ti-6Al-4V/GF-P friction-riveted joints setting new insights on the process and compared FricRiveting with state-of-the-art techniques to determine basic Friction Riveting joining guidelines for future GFRP-emergency bridges. The results of the experimental work and analyses covered the purpose of the work and fulfill the requirements of a technological development thesis. The important findings of this work led to the following conclusions:

- Three joining conditions with different combinations of RS and FT where selected for this fundamental study. RS and FT vary directly and indirectly the frictional contribution in the heat generation.. By increasing the energy input, the process temperature increased up to 761 ± 2 °C, overcoming the onset degradation temperature of GF-P reaching values nearby soften/molten glass fiber temperature and transformation temperatures of Ti-6Al-4V alloy, such as β-*transus* temperature and dynamic recrystallization (Section 6.2.1).Thus, the degradation of the thermoset composite was intrinsic to the process. Different cooling rates was noticed which considerable affected the predominance of microstructural transformations mechanisms in Ti-6Al-4V alloy, such as diffusional and diffusionless. The process temperature evaluation preliminary indicated the development of complex process-related microstructures over both joint parts.
- The torque evolution showed an unstable frictional regime attributed to the glass fiber architecture of the GF-P plate through the rivet insertion path. FricRiveting of metal-thermosetting composite was understood as a combination of abrasive (which increase torque) and adhesive (which

decrease torque) wear mechanisms. By increasing the energy input and hence the process temperature, the maximum torque decreased attributed to the low viscosity of the molten glass interphase consolidated between the metal and the composite.

- The joints achieved good rivet penetration depth (H) and widening (W) of the rivet tip. By increasing the energy input no significant variations in H and W was observed. Additionally, the extension of the visual thermo-mechanically affected composite area was not dependent to the energy input. Moreover, for higher energy input which the process temperature ranged nearby the temperature to plastically deform Ti-6Al-4V, metal flowed upwards, forming a pronounced ‘leg’ shaping in the cross-section of the joints. This deformation pattern combined with the composite degraded extent strongly influenced the mechanical behavior of the joints. Pronounced ‘”legs” and lower degraded area led to stronger joints.
- The influence of the process on the titanium rivet and on the composite was investigated using joints produced through intermediate heat input. The microstructure of Ti-6Al-4V alloy changed through the cross section of the rivet, from the equiaxed morphology to acicular structures in the rivet tip. The development of different microstructure in the metal suggested differential heat distribution and mechanical loading over the joining process. Regions where equiaxed morphology, similar to the base material but with grain coarsening, was defined as a metal-heat affected zone (MHAZ). The rivet tip, where an increase in grain low angle boundaries- response of possible dynamic recrystallization- and a combination of Widmanstätten and α’ martensitic structures were observed, was characterized as metal-thermo-mechanically affected zone (MTMAZ). MTMAZ was divided into two subzones, $MTMAZ_1$ and $MTMAZ_2$ according to the severity of the phase transformation and recrystallization. In terms of composite, a novel microstructural zone scheme was proposed (Section 6.2.3), composed by composite-heat-affected zone (CHAZ), partially degraded composite-thermo-mechanically affected zone (CTMAZ-PD) and highly degraded

composite-thermo-mechanically affected zone (CTMAZ-HD). The extension of CHAZ was not identified either by microscopy or nanohardness. The CTMAZ-PD was identified as a region full of volumetric defects while CTMAZ-HD as a glass interphase consolidated in the metal surface. This glassy interphase was formed from soften/molten broken fibers which has higher nanohardness in comparison to the glass fiber suggesting the occurrence of partial glass crystallization during the consolidation of the joint.

- The microhardness map performed on the metallic rivet evidenced an increase in hardness across the length of the rivet, following the microstructural transformations. In the rivet tip where thin acicular structures from Widmanstätten and martensitic structures were observed, the increment in hardness overcame 20% in comparison to Ti-6Al-4V base material.
- By thermal analyses, the complete degradation of the GF-P matrix after the joining process was demonstrated. By FT-IR, no characteristic absorption bands were observed confirming the severity of the degradation.
- The ultimate lap shear force ranged between 3 kN and 8 kN. The joints failed mainly through two failure modes: composite bearing followed with final failure through shear of the rivet and partial rivet pull-out (Failure Mode 1) and composite bearing followed with full rivet pull-out (Failure Mode 2). The case-study did not fail though a predominant failure mode indicating the influence of additional factors, such as the inhomogeneity of fiber content and distribution through the pultruded GF-P plate inducing different dynamic coefficient of friction**,** heat generation and hence different composite degradation extent.
- In comparison to bolted joints, Ti-6Al-4V/GF-P friction-riveted joints presented high deviation of values and average ultimate lap shear strength achieving up to 80% of the bolted joint strength. This low reproducibility did not allow the optimization of the process parameters by statistical methods and the selected joining conditions were not

conclusive regarding the potential mechanical behavior of metal/thermosetting composite friction-riveted joints.

- The case study revealed the potential of FricRiveting for joining thermosetting composite profiles used in infrastructure such as emergency bridges. A maximum reduction of 43% of necessary rivets for nodes of truss bridge model in comparison to Ti gr.2/PEI structure showed that by increasing the maturity of FricRiveting for pultruded thermoset composite, it may expect improvement on joint mechanical performance and hence on the competitiveness of the process in comparison to state-of-the-art techniques.

14 RECOMMENDATIONS FOR FUTURE WORK

The recommendations for future work were divided into *Scientific* and *Engineering*:

Scientific:

- A complementary study of glass-metal (CTMAZ-HD/AZ), glass-composite (CTMAZ-HD/CTMAZ-PD) and composite-composite (CTMAZ-PD/CHAZ) interfaces would allow further understanding of the adhesion contribution for the joining mechanism as well as the micro-mechanisms of fracture developed in these interfaces. For this, specific analytical techniques would be meaningful, such as atomic force microscopy (through modulus map), Raman spectroscopy (through local molecules analysis) and X-ray- computer microtomography (by isolating the volume of defects).

Engineering:

- The feasibility study of Ti-6Al-4V/GF-P joints using a force control variant of FricRiveting process may lead to more reproducible joint formation and hence mechanical performance. Thus, the optimization of the joining process through statistical methods by understanding the influence of each joining parameter on the joint formation and mechanical performance would be possible, reducing the number of experiments and favoring the reliability of the joint mechanical properties.
- After the optimization, analysis of the influence of natural/accelerated aging on the friction riveted joint strength would provide further design information on joint durability which is essential for the real application in emergency bridges. Additionally, since the civil infrastructures require good mechanical performances under cyclic and static loading, fatigue testing must be done as well as creep and stress relaxation testing.

- Further development and improvement of joint mechanical performance would be assessed through optimization of the joint design by means of geometries of joining parts and applied clamping torque. The development of reliable finite element model including failure criteria would be required to predict damages in the joint area and help to establish the proper level of clamping torque.

15 REFERENCES

[1] TUAKTA, C. Use of fiber reiforced polymer composite in bridge structures, Master thesis, Massachusetts Institute of Technology, USA, 2005.

[2] SEDLACEK, G.; OPPE, M.; TRUMPF, H. Design and testing of an inventive GFRP-truss- bridge for 40 t trucks and 30 m span, in *Bridge Engineering with Polymer Composites*, Leusden, 2005.

[3] SEDLACEK, G.; TRUMPF, H. *Innovative developments for bridges using FRP composites*. Cambridge: Woodhead Publishing Ltd., 2007.

[4] BORGES, R.O.M.C. Durabilidade de perfis pultrudidos em compósito de poliéster insaturado e viniléster reforçado com fibras de vidro (GFRP), Master thesis, Universidade Técnica de Lisboa, Lisboa, 2014.

[5] WANG, Y.; MENG, J.; ZHAO, Q.; QI, S. Accelerated Ageing Tests for Evaluations of a Durability Performance of Glass-Fiber Reinforcement Polyester Composites, *Journal of Materials Science & Technology*, pp. 572–576, 2012.

[6] HARPER, C.A. *Handbook of plastics, elastomers, and composites*. McGrae-HILL, 2002.

[7] ROTHEISER, J. *Joining of Plastics*, 2nd ed. Munich: Hanser Publishers, 2004.

[8] AMANCIO-FILHO, S.T.; BEYER, M.; DOS SANTOS, J.F. US 7.575.149 B2: Method of Connecting a Metallic Bolt to a Plastic Workpiece, US patent, 2009.

[9] AMANCIO-FILHO, S.T.; BEYER, M.; DOS SANTOS, J.F. EP 1 790 462 B1: Verfahren zum Verbinden eines metallischen Bolzens mit einem Kunststoff-Werkstück, European patent office, 2007.

[10] RODRIGUES, C.F.; BLAGA, L.A.; DOS SANTOS, J.F.; CANTO, L.B.; HAGE JR., E.; AMANCIO-FILHO, S.T. FricRiveting of aluminum 2024-T351 and polycarbonate: Temperature evolution, microstructure and mechanical performance, *Journal of Materials Processing Technology*, vol. 214, pp. 2029-2039, 2014.

[11] AMANCIO-FILHO, S.T. Rebitagem por Fricção ('FricRiveting'). Desenvolvimento de uma Nova Técnica de União para Juntas Híbridas do

Tipo Polímero Metal. Parte II: Propriedades Térmicas e Mecânicas, *Soldag. Insp.*, São Paulo, vol. 16, pp. 396–404, 2011.

[12] BLAGA, L.; BANCILA, R.; DOS SANTOS, J.F.; AMANCIO-FILHO, S.T. Friction Riveting of glass-fibre-reinforced polyetherimide composite and titanium grade 2 hybrid joints, Materials and Design, pp. 825–829, 2013.

[13] ALTMEYER, J.; DOS SANTOS, J.F.; AMANCIO-FILHO, S.T. Effect of Friction Riveting Process Parameters on the Joint Formation and Performance of Ti alloy/ Short-fibre Reinforced Polyether Ether Ketone Joints, *Materials &Design*, vol. 60, pp. 164-176, 2014.

[14] PROENÇA, B.; BLAGA, L.A.; DOS SANTOS, J.F.; CANTO, L.B.; AMANCIO-FILHO, S.T. Force controlled Friction Riveting of glass fiber reinforced polyamide 6 and aluminum alloy 6056 hybrid joints, presented at the ANTEC, Orlando, USA, 2015.

[15] HUANG, Z.; SUGIYAMA, S.; YANAGIMOTO, J. Hybrid joining process for carbon fiber reinforced thermosetting plastic and metallic thin sheets by chemical bonding and plastic deformation, *Journal of Materials Processing Technology*, vol. 213, pp. 1864–1874, 2013.

[16] BORBA, N.Z.; BLAGA, L.A.; CANTO, L.C.; DOS SANTOS, J.F.; AMANCIO-FILHO, S.T. Friction Riveting of pultruded thermoset glass fiber reinforced polyester composite and Ti6Al4V hybrid joints, presented at the ANTEC, Las Vegas, Nevada, USA, 2014.

[17] VINSON, J.R. Mechanical fastening of polymer composites, pp. 19, 2004.

[18] AMANCIO-FILHO, S.T.; ABIBE, A.B.; DOS SANTOS, J.F.; NICOLAIS, L. Joining: Mechanical Fastening of Polymers, Composites, and Polymer–Metal Hybrid Structures, in *Wiley Encyclopedia of Composites*, John Wiley & Sons, Inc., 2011.

[19] STOKES, V.K. Joining methods for plastics and plastic composites: An overview, *Polym. Eng. Sci.*, vol. 29, no. 19, pp. 1310–1324, 1989.

[20] LEE, C.J.; LEE, J.M.; RYU, H.Y.; LEE, K.H.; KIM, M.B.; KO, D.C. Design of hole-clinching process for joining of dissimilar materials – Al6061-T4 alloy with DP780 steel, hot-pressed 22MnB5 steel, and carbon fiber reinforced plastic, *J. Mater. Process. Technol.*, vol. 214, no. 10, pp. 2169–2178, 2014.

[21] CAMANHO, F. Stress analysis and strength prediction of mechanically fastened joints in frp: A review, *Elsevier*, London, UK, pp. 529–547., 1996.

[22] MESSLER, R.W. Trends in key joining technologies for the twenty-first century, *Assembly Automation*, pp. 118–128, 2000.

[23] OLMEDO A.; SANTIUSTE, C. On the prediction of bolted single-lap composite joints. Department of Continuum Mechanics and Structural Analysis, University Carlos III of Madrid, 2012.

[24] ILIC, I.;MAKSIMOVIC, M.; STUPAR, S.; STAMENKOVIC, D. Computation Method in failure analysis of mechanically fastened joints at layered composites, *Journal of Mechanical Engineering*, pp. 553–559, 2012.

[25] XIAO, Y.; ISHIKAWA, T. Bearing strength and failure behavior of bolted composite joints (part I: Experimental investigation), *Compos. Sci. Technol.*, vol. 65, no. 7–8, pp. 1022–1031, 2005.

[26] PISANO, A.A.; FUSCHI, P. Mechanically fastened joints in composite laminates: Evaluation of load bearing capacity, *Compos. Part B Eng.*, vol. 42, no. 4, pp. 949–961, 2011.

[27] SEN, F.; PAKDIL, M.; SAYMAN, O.; BENLI, S. Experimental failure analysis of mechanically fastened joints with clearance in composite laminates under preload, *Mater. Des.*, vol. 29, no. 6, pp. 1159–1169, 2008.

[28] CHEN, W.H.; LEE, S.S.; YEH, J.T. Three-dimensional contact stress analysis of a composite laminate with bolted joint, *Compos. Struct.*, vol. 30, no. 3, pp. 287–297, 1995.

[29] RICCIO, A.; MARCIANO, L. Effects of Geometrical and Material Features on Damage Onset and Propagation in Single-lap Bolted Composite Joints under Tensile Load: Part I – Experimental Studies, *J. Compos. Mater.*, vol. 39, no. 23, pp. 2071–2090, 2005.

[30] THOPPUL, S.D.; FINEGAN, J.; GIBSON, R.F. Mechanics of mechanically fastened joints in polymer–matrix composite structures – A review, *Compos. Sci. Technol.*, vol. 69, no. 3–4, pp. 301–329, 2009.

[31] COOPER, C.; TURVEY, G.J. Effects of joint geometry and bolt torque on the structural performance of single bolt tension joints in pultruded GRP sheet material, *Compos. Struct.*, vol. 32, no. 1–4, pp. 217–226, 1995.

[32] CAMANHO, P.P.; LAMBert, M. A design methodology for mechanically fastened joints in laminated composite materials, *Compos. Sci. Technol.*, vol. 66, no. 15, pp. 3004–3020, 2006.

[33] KAPTI, S.; SAYMAN, O.; OZEN, M.; BENLI, S. Experimental and numerical failure analysis of carbon/epoxy laminated composite joints under different conditions, *Mater. Des.*, vol. 31, no. 10, pp. 4933–4942, 2010.

[34] THOMAS, F.; ZHAO, Y. Torque Limit for Composites Joined with Mechanical Fasteners, in *46th AIAA/ASME/ASCE/AHS/ASC Structures, Structural Dynamics and Materials Conference*, American Institute of Aeronautics and Astronautics, 2005.

[35] OLMEDO, A.; SANTIUSTE, C.; BARBERO, E. An analytical model for predicting the stiffness and strength of pinned-joint composite laminates, *Compos. Sci. Technol.*, vol. 90, pp. 67–73, 2014.

[36] FRIEDRICH, H.E. *Leichtbau in der Fahrzeugtechnik*. Springer Vieweg, 2013.

[37] NIU, M.C.Y. *Airframe Structural Design*. Technical book company, 1989.

[38] FIBERLINE COMPOSITES Structural profiles. Available: www.fiberline.com. Accessed: 26-Aug-2013.

[39] AMANCIO-FILHO, S.T. Friction riveting: Development and analysis of a new joining technique for polymer-metal multi-materials structures, Ph.D. Thesis, Technischen Universitäat Hamburg-Harburg, GKSS-Forschungszentrum Geesthacht, 2007.

[40] AMANCIO-FILHO, S.T.; DOS SANTOS, J.F. FricRiveting: A new technique for joining thermoplastics to lightweight alloys, presented at the ANTEC 2008, pp. 841–845, USA, 2008.

[41] AMANCIO-FILHO, S.T. Rebitagem por Fricção (‘FricRiveting’). Desenvolvimento de uma Nova Técnica de União para Juntas Híbridas do Tipo Polímero-Metal. Parte I: Processo e Microestrutura, *Soldag. Insp.*, São Paulo, vol. 16, pp. 387–394, 2011.

[42] AMANCIO-FILHO, S.T. FRICTION RIVETING: development and analysis of a new joining technique for polymer-metal multi-material structures, *Weld. World*, pp. 13–24, 2011.

[43] BLAGA, L.; DOS SANTOS, J.F.; BANCILA, R.; AMANCIO-FILHO, S.T. Friction Riveting (FricRiveting) as a new joining technique in GFRP lightweight bridge construction, *Constr. Build. Mater.*, vol. 80, no. 0, pp. 167–179, 2015.

[44] AMANCIO-FILHO, S.T.; DOS SANTOS, J.F. Development of FricRiveting as a new joining technique for polymer and lightweight alloys, *Materialwissenschaft und Werkstofftechnik*, Germany, pp. 799–805, 2008.

[45] AMANCIO-FILHO, S.T.; ROEDER, J.; NUNES, S.P.; DOS SANTOS, J.F.; BECKMANN, F. Thermal degradation of polyetherimide joined by friction riveting (FricRiveting). Part I: Influence of rotation speed, *Polym. Degrad. Stab.*, vol. 93, no. 8, pp. 1529–1538, 2008.

[46] ALTMEYER, J.; SUHUDDIN, U.F.H.; DOS SANTOS, J.F.; AMANCIO-FILHO, S.T. Microstructure and mechanical performance of metal-composite hybrid joints produced by FricRiveting, *Compos. Part B Eng.*, vol. 81, pp. 130–140, 2015.

[47] BLAGA, L.B. Innovating material in bridge construction. Contribution to construction with composite fiber-reinforced materials, Ph.D. Thesis, Polytechnic University of Timisoara, Timissoara,Romania, 2012.

[48] ALTMEYER, J. Fundamental characteristics of friction riveted multi-material joints, Ph.D. Thesis, Technischen Universität Hamburg-Harburg, Hamburg, Germany, 2014.

[49] BORGES, M.F. Desenvolvimento de nova geometria de rebite para uso em estruturas híbridas compósito-metal obtidas através do processo de rebitagem por fricção, Master Thesis, Universidade Federal do Rio Grande do Sul, Porto Alegre, 2013.

[50] KITAMURA, K.; FUJII, H.; IWATA, Y.; SUN, Y.S.; MORISADA, Y. Flexible control of the microstructure and mechanical properties of friction stir welded Ti–6Al–4V joints, *Mater. Des.*, vol. 46, no. 0, pp. 348–354, 2013.

[51] BOYER, R.R. An overview on the use of titanium in the aerospace industry, *Int. Symp. Metall. Technol. Titan. Alloys*, vol. 213, no. 1–2, pp. 103–114, 1996.

[52] WANG, S.; WEI, M.; TSAY, L. Tensile properties of LBW welds in Ti–6Al–4V alloy at evaluated temperatures below 450 °C, *Mater. Lett.*, vol. 57, no. 12, pp. 1815–1823, 2003.

[53] LIMA, M.S.F. Laser beam welding of titanium nitrid coated titanium using pulse-shaping, *Materials Research*, pp. 323–328, 2005.

[54] LEYENS, C.; PETERS, M. *Titanium and Titanium Alloys: Fundamentals and Applications*. Weinheim: Wiley-VCH, 2003.

[55] FONDA, R.W.; KNIPLING, K.E. Texture development in friction stir welds, *Science and Technology of Welding and Joining*, pp. 288–294, 2011.

[56] MATTHEW, J.; DONACHIE, J. *Titanium: A technical guide*. 2000.

[57] BOYER, R.; WELSCH, G.; COLLINGS, E.W. *Materials Properties Handbook: Titanium Alloys*. ASM International, 1994.

[58] TANG, X.; AHMED, T.; RACK, H.J. Phase transformations in Ti-Nb-Ta and Ti-Nb-Ta-Zr alloys, *Journal of Material Science*, pp. 1805–1811, 2000.

[59] MOFFAT, D.L.; LARBALESTIER, D.C. The competition between martensite and omega in quenched Ti-Nb alloys, *Metallurgical transactions A*, pp. 1677–1988, 1988.

[60] *ASM Handbook- Properties and Selection: Nonferrous Alloys and Special-Purpose Materials*, vol. 2. ASM International.

[61] BELADI, H.; CHAO, Q.; ROHRER, G.S. Variant selection and intervariant crystallographic planes distribution in martensite in a Ti–6Al–4V alloy, *Acta Mater.*, vol. 80, pp. 478–489, 2014.

[62] VILA, P.B. Effect of heat treatments on the microstructure of deformed Ti-6Al-4V, Diplomarbeit, Institut für Werkstoffwissenschaft und Werkstofftechnologie, Technischen Universität Wien, Wien, 2010.

[63] LIAO, S.; DUFFY, J. Adiabatic shear bands in a TI-6Al-4V titanium alloy, *J. Mech. Phys. Solids*, vol. 46, no. 11, pp. 2201–2231, 1998.

[64] LEE, D.G.; LEE, Y.; LEE, S.; LEE, C.; HUR, S.M. Dynamic deformation behavior and ballistic impact properties of Ti-6Al-4V alloy having equiaxed

and bimodal microstructures, *Metall. Mater. Trans. A*, vol. 35, no. 10, pp. 3103–3112, 2004.

[65] ZHOU, Z.; LIU, H.J.; LIU, Q.W. Effect of rotation speed on microstructure and mechanical properties of Ti–6Al–4V friction stir welded joints, *Mater. Des.*, vol. 31, no. 5, pp. 2631–2636, 2010.

[66] BALASUBRAMANIAN, S.T.; BALAKRISHNAN, M.; BALASUBRAMANIAN, V.; MANICKAM, M.A.M. Influence of welding processes on microstructure, tensile and impact properties of Ti-6Al-4V alloy joints, *Trans. Nonferrous Met. Soc. China*, vol. 21, no. 6, pp. 1253–1262, 2011.

[67] ESMAILY, M.; NOOSHIN S.; MORTAZAVI; TODEHFALAH, P.; RASHIDI, M. Microstructural characterization and formation of α′ martensite phase in Ti–6Al–4V alloy butt joints produced by friction stir and gas tungsten arc welding processes, *Mater. Des.*, vol. 47, no. 0, pp. 143–150, 2013.

[68] DANIELSON, P.; WILSON, R.; ALMAN, D. Microstructure of Titanium Welds, *Advanced Materials & Processes*, pp. 1-7, USA, 2003.

[69] WANG, S.; WU, X. Investigation on the microstructure and mechanical properties of Ti–6Al–4V alloy joints with electron beam welding, *Sustain. Mater. Des. Appl.*, vol. 36, no. 0, pp. 663–670, 2012.

[70] AKMAN, E.; DEMIR, A.; CANEL, T.; SINMAZÇELIK, T. Laser welding of Ti6Al4V titanium alloys, *J. Mater. Process. Technol.*, vol. 209, no. 8, pp. 3705–3713, 2009.

[71] ZHU, Z.; LEE, K.Y.; WANG, X. Ultrasonic welding of dissimilar metals, AA6061 and Ti6Al4V, *Int. J. Adv. Manuf. Technol.*, vol. 59, no. 5–8, pp. 569–574, 2012.

[72] MIRONOV, S.; ZHANG, Y.; SATO, Y.S.; KOKAWA, H. Crystallography of transformed β microstructure in friction stir welded Ti–6Al–4V alloy, *Scr. Mater.*, vol. 59, no. 5, pp. 511–514, 2008.

[73] ZHANG, Y.; SATO, Y.S.; KOKAWA, H.; PARK, S.H.C.; HIRANO, S. Microstructural characteristics and mechanical properties of Ti–6Al–4V friction stir welds, *Mater. Sci. Eng. A*, vol. 485, no. 1–2, pp. 448–455, 2008.

[74] MIRONOV, S.; SATO, Y.S.; KOKAWA, H. Evaluation of texture developed in high-temperature beta phase during friction stir welding of Ti-6Al-4V, *Key Engineering Materials*, vol. 508, pp. 106–111, 2012.

[75] FONDA, R.W.; KNIPLING, K.E. Texture development in near-α Ti friction stir welds, *Acta Mater.*, vol. 58, no. 19, pp. 6452–6463, 2010.

[76] RAMANI, K.; TAGLE, J.; NAZRE, A.; SWARTS, D.; LIN, S. Thin-film thermoplastic-metal joining process for titanium to poly(etherketoneetherketoneketone), *Polym. Eng. Sci.*, vol. 35, no. 24, pp. 1972–1978, 1995.

[77] ASM Handbook, *Composites*, vol. Vol. 21. ASM International, 2001.

[78] Military Handbook, *MIL-HDBK-17-1F: Composite Materials Handbook. Vol. 1. Polymer-matrix Composites Guidelines for Characterization of Structural Materials*. .

[79] MESSLER, R.W. Joining composite materials and structures: Some thought-provoking possibilities, *Journal of Thermoplastic Composite Materials*, pp. 51–75, 2004.

[80] YANG, L.J. Microstructure formation in the cure of unsaturated polyester resins, *Polymer*, pp. 1793–1800, 1988.

[81] HILTZ, J.A. Pyrolysis—gas chromatography/mass spectrometry identification of styrene cross-linked polyester and vinyl ester resins, *J. Anal. Appl. Pyrolysis*, vol. 22, no. 1–2, pp. 113–128, 1991.

[82] RATNA, D. *Handbook of Thermoset Resins*. United Kingdom: iSmithers, 2009.

[83] BAHADUR, S.; ZHENG, Y. Mechanical and Tribological behavior of polyester reinforced with short glass fibers, *Wear*, pp. 251–266, 1990.

[84] LAOUBI, K.; HAMADI, Z.; BENYAHIA, A.A.; SERIER, A.; AZARI, Z. Thermal behavior of E-glass fiber-reinforced unsaturated polyester composites, *Composites: Part B*, pp. 520–526, 2014.

[85] RAVEY, M. Pyrolysis of unsaturated polyester resin. Quantitative aspects, *J. Polym. Sci. Polym. Chem. Ed.*, vol. 21, no. 1, pp. 1–15, 1983.

[86] ANDERSON, D.A.; FREEMAN, E.S. The kinetics of the thermal degradation of the synthetic styrenated polyester, *Applied Polymer Science*, pp. 192–199, 1959.

[87] LEARMONTH, G.S.; NESBIT, A. Flammability of polymers. V. Thermal volatilization analysis of polyester resin compositions, *Br Polym.J*, pp. 250–317, 1972.

[88] MESSLER, R.W. Trends in key joining technologies for the twenty-first century, *Assembly Automation*, pp. 118–128, 2000.

[89] ZHANG, Y.; KELLER, T. Progressive failure process of adhesively bonded joints composed of pultruded GFRP, *Composites Science and Technology*, pp. 461–470, 2008.

[90] KELLER, T.; VALLEE, T. Adhesively bonded lap joints from pultruded GFRP profiles. Part I: stress-strain analysis and failure modes, *Composites: Part B*, pp. 331–340, 2005.

[91] KELLER, T.; VALLÉE, T. Adhesively bonded lap joints from pultruded GFRP profiles. Part II: joint strength prediction, *Compos. Part B Eng.*, vol. 36, no. 4, pp. 341–350, 2005.

[92] KELLER, T.; TIRELLI, T. Fatigue behavior of adhesively connected pultruded GFRP profiles, *Composite Struct*, pp. 55–64, 2004.

[93] KIM, J.H; PARK, B.J.; HAN, Y.W. Evaluation of fatigue characteristics for adhesively-bonded composite stepped lap joint, *Compos. Struct.*, vol. 66, no. 1–4, pp. 69–75, 2004.

[94] GIRÃO COELHO, A.M.; MOTTRAM, J.T. A review of the behavior and analysis of bolted connections and joints in pultruded fibre reinforced polymers, *Mater. Des.*, vol. 74, pp. 86–107, 2015.

[95] POPOAEI, S.; TÃRANU, N.; CIOBANU, P.; OPRISAN, G. Structural response of various single lap joint connections for pultruded E-glass fiber reinforced isophtalic polymers composite plates. Buletinul Institutului Politehnic Din IASI, 2013.

[96] ABD-EL-NABY, S.F.M.; HOLLAWAY, L. The experimental behavior of bolted joints in pultruded glass/ polyester material. Part 1: Single-bolt joints, *Composites*, vol. 24, no. 7, pp. 531–538, 1993.

[97] MORTAIGNE, B.; BOURBIGOT, S.; LE BRAS, M.; CORDELLIER, G.; BAUDRY, A.; DUFAY, J. Fire behavior related to the thermal degradation of unsaturated polyesters, *Polym. Degrad. Stab.*, vol. 64, no. 3, pp. 443–448, 1999.

[98] ASTM INTERNATIONAL, ASTM D3171-99: Standard test methods for constituent content of composite materials. West Conshohocken, Pa, 1999.

[99] ASTM INTERNATIONAL, ASTM E8: Tension Testing of Metallic Materials. West Conshohocken, Pa.

[100] ASTM INTERNATIONAL, ASTM E.-10e1: Standard Test Method for Knoop and Vickers Hardness of Materials, *West Conshohocken*, Pa, 2010.

[101] ASTM INTERNATIONAL, ASTM E112-13: Standard test method for determining average grain size. West Conshohocken, Pa, 2013.

[102] AHMED, T.; RACK, H.J. Phase transformations during cooling in α+β titanium alloys, *Mater. Sci. Eng. A*, vol. 243, no. 1–2, pp. 206–211, 1998.

[103] *ASM Metals Handbook- Metalography and Microstructures*, 8th ed., vol. 9. 1998.

[104] Electron Backscattered Diffraction. Oxford Instruments Analytical, 2000.

[105] ASTM INTERNATIONAL, ASTM D 5961 M – 08: Standard test method for bearing response of polymer matrix composite laminates. West Conshohocken, Pa, 2010.

[106] ASTM INTERNATIONAL, ASTM D3248-73: Method of test for coefficient of static friction of corrugated and solid fiberboard. West Conshohocken, Pa, 1984.

[107] LEMPERT, G.D.; TSOUR, A. Reduction of static friction between surfaces of Ti-6Al-4V and between surfaces of Ti-6Al-4V and Al-7075, *Surf. Coat. Technol.*, vol. 52, no. 3, pp. 291–295, 1992.

[108] QU, J.; BLAU, P.J.; WATKINS, T.R.; CAVIN, O.B.; KULKARNI, N.S. Friction and wear of titanium alloys sliding against metal, polymer, and ceramic counterfaces, *Wear*, vol. 258, no. 9, pp. 1348–1356, 2005.

[109] BLAGA, L.A.; AMANCIO-FILHO, S.T.; DOS SANTOS, J.F.; BANCILA, R. FricRiveting of Civil Engineering Composite Laminates for Bridge Construction, presented at the ANTEC 2012, Orlando, USA, 2012.

[110] DIETER, G.E. *Metalurgia Mecânica*, 2ª ed. Guanabara Dois, 1981.

[111] HOMPORAVÁ, P.; POLETTI,C.; STOCKINGER, M.; WARCHOMICKA, F. Dynamic phase evolution in titanium alloy Ti-6Al-4V. Proceedings of the 12th World Conference on Titanium, vol.1, Austria, 2011.

[112] DODIUK, H.; GOODMAN, S.H. *Handbook of Thermoset Plastics*, 3rd ed. Elsevier, 2014.

[113] KANDARE, E.; KANDOLA, B.K.; PRICE, D.; NAZARÉ, S.; HORROCKS, R.A. Study of the thermal decomposition of flame-retarded unsaturated polyester resins by thermogravimetric analysis and Py-GC/MS, *Polym. Degrad. Stab.*, vol. 93, no. 11, pp. 1996–2006, 2008.

[114] NEUMANN, A. Reibschweissen von Metallen 1. Auflage. Verlag Technik GmbH, Berlin, 1991.

[115] ABIBE, A.B.; DOS SANTOS, J.F.; AMANCIO-FILHO, S.T. Friction Staking: A noval staking joining method for hybrid structures, presented at the ANTEC 2014, Las Vegas, Nevada, USA, 2014.

[116] AMANCIO-FILHO, S.T.; DOS SANTOS, J.F. Influence of processing parameters on microstructure and properties of a polyetherimide joined by FricRiveting: Investigation of rotational speed, presented at the ANTEC 2009, Chicago, USA, 2009.

[117] GOUSHEGIR, S.M.; DOS SANTOS, J.F.; AMANCIO-FILHO, S.T. Friction Spot Joining of aluminum AA2024/carbon-fiber reinforced poly(phenylene sulfide) composite single lap joints: Microstructure and mechanical performance, *Mater. Des.*, vol. 54, pp. 196–206, 2014.

[118] JUNIOR, W.S.; HANDGE, U.A.; DOS SANTOS, J.F.; ABETZ, V.; AMANCIO-FILHO, S.T. Feasibility study of friction spot welding of dissimilar single-lap joint between poly(methyl methacrylate) and poly(methyl methacrylate)-SiO2 nanocomposite, *Mater. Des.*, vol. 64, pp. 246–250, 2014.

[119] ZHAO, J.W.; DING, H.; ZHAO, W.J.; CAO, F.R.; HOU, H.L.; LI, Z.Q. Modeling of dynamic recrystallization of Ti6Al4V alloy using a cellular automaton approach, *Acta Metall. Sin. Engl. Lett.*, vol. 21, no. 4, pp. 260–268, 2008.

[120] KATZAROV, I.; MALINOV, S.; SHA, W. Finite element modeling of the morphology of β to α phase transformation in Ti-6Al-4V alloy, *Metall. Mater. Trans. A*, vol. 33, no. 4, pp. 1027–1040, 2002.

[121] MALINOV, S.; GUO, Z.; SHA, W. Modeling of beta to alpha phase transformation kinetics in Ti-6Al-4V alloy, presented at the Materials Congress 2000: Materials for the 21st Century, pp.92, United Kingdom, 2000.

[122] COLLINGS, E.W. *The physical metallurgy of titanium alloys*. American Society for Metals, 1984.

[123] FRIEDRICH, K. *Advances in composite tribology*, vol. 8. Elsevier, 1945.

[124] BAI, Y.; POST, N.L.; LESKO, J.J.; KELLER, T. Experimental investigations on temperature-dependent thermo-physical and mechanical properties of pultruded GFRP composites, *Thermochim. Acta*, vol. 469, no. 1–2, pp. 28–35, 2008.

[125] MA, Z.Y.; PILCHAK, A.L.; JUHAS, M.C.; WILLIAMS, J.C. Microstructural refinement and property enhancement of cast light alloys via friction stir processing, *Scr. Mater.*, vol. 58, no. 5, pp. 361–366, 2008.

[126] QIAN, L.; MEI, J.; LIANG, J.; WU, X. Influence of position and laser power on thermal history and microstructure of direct laser fabricated Ti-6Al-4V samples, *Materials Science and Technology*, vol. 21, pp. 597-605, 2005.

[127] BAUFELD, B.; VAN DER BIEST, O.; GAULT, R. Microstructure of Ti-6Al-4V specimens produced by shaped metal deposition, *Int. J. Mater. Res.*, vol. 100, no. 11, pp. 1536–1542, 2009.

[128] CALLISTER JR., W.D. *Materials Science and Engineering: An Introduction*, 7th ed. John Wiley & Sons, 2007.

[129] ELMER, J.W.; PALMER, T.A.; BABU, S.S.; SPECHT, E.D. In situ observations of lattice expansion and transformation rates of alpha and

beta phases in Ti-6Al-4V, *Materials Science and Engineering A*, pp. 104–113, 2005.

[130] PILCHAK, A.L.; WILLIAMS, J.C. Microstructure and Texture Evolution during Friction Stir Processing of Fully Lamellar Ti-6Al-4V, *Metall. Mater. Trans. A*, vol. 42, no. 3, pp. 773–794, 2010.

[131] PASCAULT, J.P.; SAUTEREAU, H.; VERDU, J.; WILLIAMS, R.J.J. *Thermosetting Polymers*. New York: Marcel Dekker, 2002.

[132] SUHUDDIN, U.; MIRONOV, S.; KROHN,H.; BEYER, M.; DOS SANTOS, J.F. Microstructural Evolution During Friction Surfacing of Dissimilar Aluminum Alloys, *Metall. Mater. Trans. A*, vol. 43, no. 13, pp. 5224–5231, 2012.

[133] WYATT, Z.W.; JOOST, W.J.; ZHU, D.; ANKEM, S. Deformation mechanisms and kinetics of time-dependent twinning in an α-titanium alloy, *Int. J. Plast.*, vol. 39, pp. 119–131, 2012.

[134] SAKAMOTO, H. Distinction between Thermal and Stress-Induced Martensitic Transformations and Inhomogeneity in Internal Stress, *Mater. Trans. - MATER TRANS*, vol. 43, no. 9, pp. 2249–2255, 2002.

[135] WALLENBERGER, F.T.; BINGHAM, P.A. *Fiberglass and Glass Technology. Energy-Friendly Compositions and Applications*. Springer, 2010.

[136] ZAWRAH, M.F.; HAMZAWY, E.M.A. Effect of cristobalite formation on sinterability, microstructure and properties of glass/ceramic composites, *Ceram. Int.*, vol. 28, no. 2, pp. 123–130, 2002.

[137] IMANAKA, Y.; AOKI, S.; KAMEHARA, N.; NIWA, K. Cristobalite Phase Formation in Glass/Ceramic Composites, *J. Am. Ceram. Soc.*, vol. 78, no. 5, pp. 1265–1271, 1995.

[138] YUAN, F.; HUANG, L. Brittle to Ductile Transition in Densified Silica Glass, *Sci. Rep.*, vol. 4, 2014.

[139] AMANCIO-FILHO, S.T.; DOS SANTOS, J.F. FricRiveting: A new joining technique for thermoplastics-lightweight alloy structures, presented at the Materials Science and Technology 2008, Joining of advanced and specialty materials, Pittsburgh, Pennsylvania, 2008.

[140] POCIUS, A.V. *Adhesion and Adhesives Technology-An Introduction*, 3 rd ed. Munich: Hanser, 2012.

[141] KREVELEN, D. *Properties of Polymers*, 4th ed. Elsevier, 2009.

[142] SILVERSTEIN, W. *Spectrometric Identification of Organic Compounds*, 7ed. ed., 2005.

[143] OROWAN, E. presented at the Symposium on internal stresses in metals and alloys, Institute of Metals, pp.451, London, 1948.

[144] MORITA, K.W.T Strengthening of Ti–6Al–4V Alloy by Short-Time Duplex Heat Treatment, *Mater. Trans. - MATER TRANS*, vol. 46, no. 7, pp. 1681–1686, 2005.

[145] CALLEJA, F.J.B.; FAKIROV, S. *Microhardness of polymers*. 2007.

[146] GIBSON, R.F. A review of recent research on nanoindentation of polymer composites and their constituents, *Compos. Sci. Technol.*, vol. 105, pp. 51–65, 2014.

[147] GIRÃO COELHO, A.M.; MOTTRAM, J.T. A review of the behavior and analysis of bolted connections and joints in pultruded fibre reinforced polymers, *Mater. Des.*, vol. 74, pp. 86–107, 2015.

[148] VIEILLE, B.; AUCHER, J.; TALEB, L. Woven ply thermoplastic laminates under severe conditions: Notched laminates and bolted joints, *Compos. Part B Eng.*, vol. 42, no. 3, pp. 341–349, 2011.

[149] VIEILLE, B.; ALBOUY, W.; TALEB, L. Influence of stamping on the compressive behavior and the damage mechanisms of C/PEEK laminates bolted joints under severe conditions, *Compos. Part B Eng.*, vol. 79, pp. 631–638, 2015.

[150] LÜTJERING, G.; WILLIAMS, J.C. *Titanium*, 2 nd ed. Springer, 2007.

[151] GU, J.; HARDIE, D. Effect of hydrogen on the tensile ductility of Ti6Al4V: Part II Fracture of pre-cracked tensile specimens, *J. Mater. Sci.*, vol. 32, no. 3, pp. 609–617, 1997.

[152] DERRO, R.J. Fractography Handbook of Spaceflight Metals, *NASA Reference Publication*, 1993.

[153] EUROCODE 3: EN 1993-2: Steel Bridges. Eurocode Committee for Standardization, 2010.

ANNEX A Chemical Composition of E-Glass Fiber

Table A. 1 Chemical composition of E-glass fiber used by Fiberline Composites in GF-P composite.

Weight (wt. %)	Al_2O_3	BaO	CaO	MgO	NaO_2	SiO_2
	15.2	8.0	17.2	4.7	0.6	54.3

APPENDIX A Axial Force Contribution on the Heat Input

Following the Equation 6.2 (see Section 6.2), the energy input can be simply described as a function of two main contributions: frictional contribution (described in Section 6.2) and axial contribution. The frictional energy (E_{fr}) calculation was detailed in Section 5.5 while the axial energy (E_{ax}) is expressed by Equation A.1.

$$\boldsymbol{E_{ax} = \int F \times \upsilon_0 \, dt \, [J]} \quad \text{(A.1)}$$

F [N] is the axial force applied in the rivet and υ_0 [m] is the burn-off rate. F can be assumed constant with the time during the forging phase, as presented in Figure 6.50. The burn-off rate is the quotient between the burn-off – axial displacement, i.e. course, in the joining diagram (see Figure 6.50, Section) - and the heating time – time from the begging of the joining process to rotational speed equals null. Thus, υ_0 is also constant with the time. Since the limits of integration are the same of the heating time, the E_{ax} is the product between the forging force and burn-off (BO). The averages of these variables are presented in Table A.2.

Table A. 2 Average of burn-off variable and forging force of comparative joining conditions for Ti-6Al-4V/GF-P joints.

	Burn-off, BO (m)	F (N)
C1	0.064 ± 0.007	3245 ± 16
C2	0.059 ± 0.015	3246 ± 30
C3	0.069 ± 0.007	3231 ± 28

Figure A.1 presents the frictional energy in comparison to the axial energy for each joining condition investigated in this work. The axial energy ranged between 11% and 13% of the frictional energy, showing that the most important contribution in heat generation in FricRiveting of thermosetting composites happens by friction. Therefore, the normal force contribution can be ignored to describe the heat input.

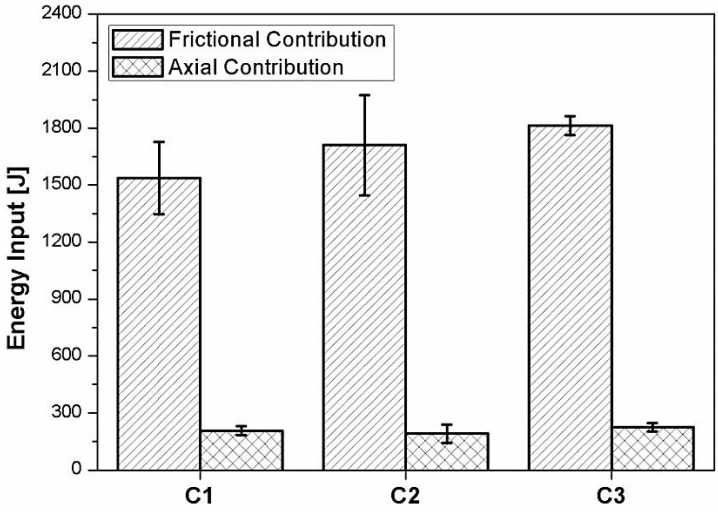

Figure A. 1 Energy input contributions for three joining condition.

APPENDIX B Energy Dispersive X-Ray Spectroscopy (EDS) of Ti-6Al-4V Base Material

The chemical compositions of α-Ti and β-Ti phases of Ti-6Al-4V base material were carried out using EDS analysis performed in transmission electron microscope. The results are presented in Figure B.1.

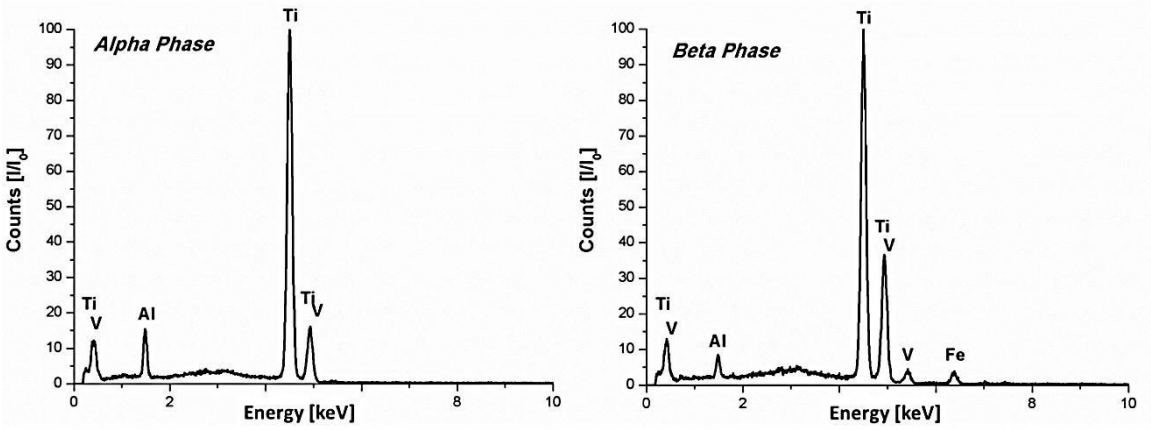

Figure B. 1 Spectra of semi-quantitative chemical composition of α-Ti and β-Ti phases presented in Ti-6Al-4V base material.

As expected, the β-Ti phase presented a considerable content of vanadium element which stabilizes the phase at room temperature while α-Ti phase presented an increase in aluminum content which stabilizes the phase. The iron element also stabilizes the β-Ti phase explaining the absence in α phase.

APPENDIX C X-Ray Diffraction (XRD) of FricRiveting Sample

Figure C.1 shows a typical diffractogram of samples extracted from plastically deformed rivet (Region 4, Figure 9.2, Section 9.2). XRD pattern of hexagonal close packed (hcp) α-Ti phase and weak peak of body-centered cubic (bcc) β-Ti phase at around 2θ= 40° were identified. The XRD data also provided a first impression about the absence of peaks for orthorhombic martensite (α''). These findings were observed also for material extracted from Region 3 (Figure 9.4-b, Section 9.2).

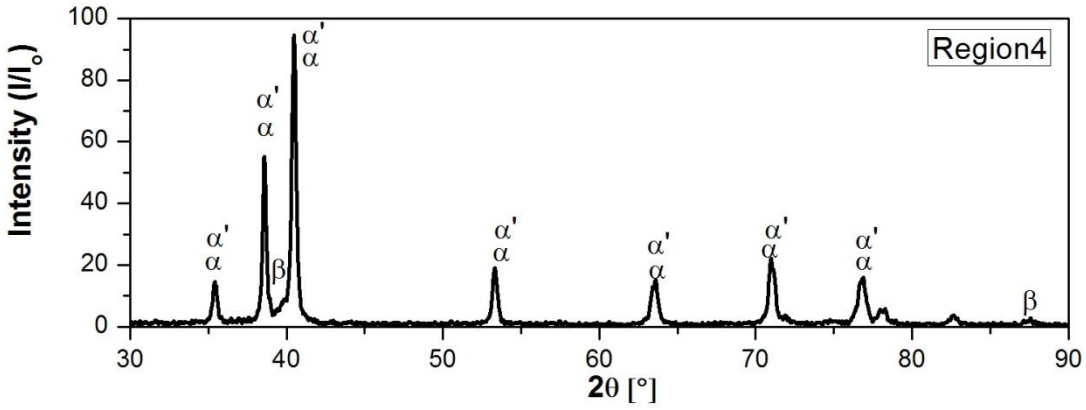

Figure C. 1 X-ray diffraction pattern of Ti-6Al-4V from the anchoring zone (Region3) of the Ti-6Al-4V/GF-P friction-riveted joint (joint from joining condition C2: 9000 rpm, 1.2 s and 1.2 s).

APPENDIX D Electron Backscattered Diffraction (EBSD) of Deformed Ti-6Al-4V Alloy

The phase content and grain boundary maps were obtained by EBSD analysis for the regions of interest through the Ti-6Al-4V rivet. Figure D.1 shows the maps for the respective regions detailed in the joint cross section.

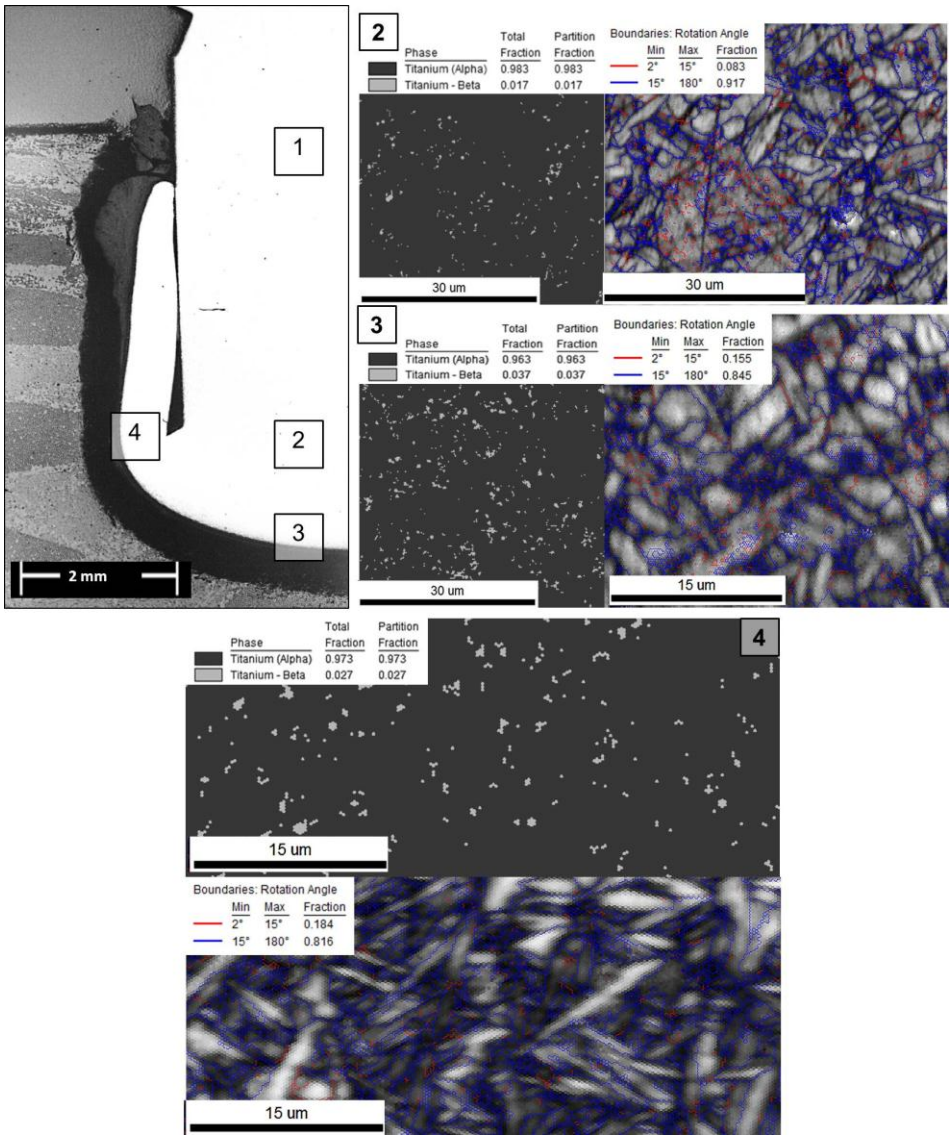

Figure D. 1 α-Ti and β-Ti phase contents map and grain boundary map for regions of interest in the metallic rivet through the joint cross-section.

APPENDIX E Fourier Transformed Infrared Spectroscopy

Figure E.1 shows a typical IR spectrum of polyester matrix from GF-P composite with deconvoluted peaks. The peak deconvolution was performed using Origin Pro.8 software. The signal processing analysis was selected followed by the base line definition and finally the deconvolution tool. All the characteristic absorption bands of the polyester and their respective wavenumbers are presented in Table E.1.

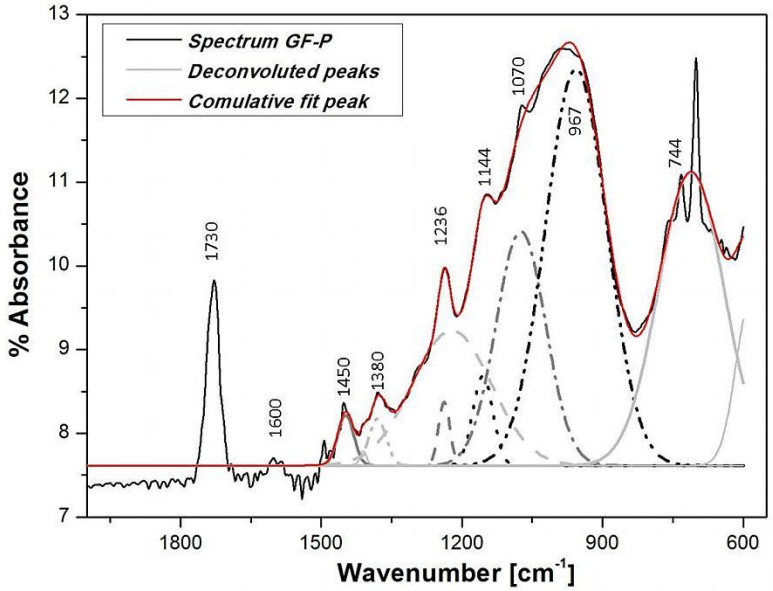

Figure E. 1 Infrared spectrum of GF-P base material with deconvoluted peaks.

Table E. 1 Characteristic absorption bands of polyester from GF-P composite with their respective wavenumbers.

	Carbonyl group	Phenyl group	(υ-C-O-) from ester group	Unsaturated aromatic, in-plane (δ-C=CH-)	Unsaturated aromatic, out-of-plane (γ-C=CH-)
Wavenumber (cm^{-1})	1730	1600 140	1380 1144	1070	744

APPENDIX F Typical force-displacement curves of Ti-6Al-4V/GF-P friction-riveted joints

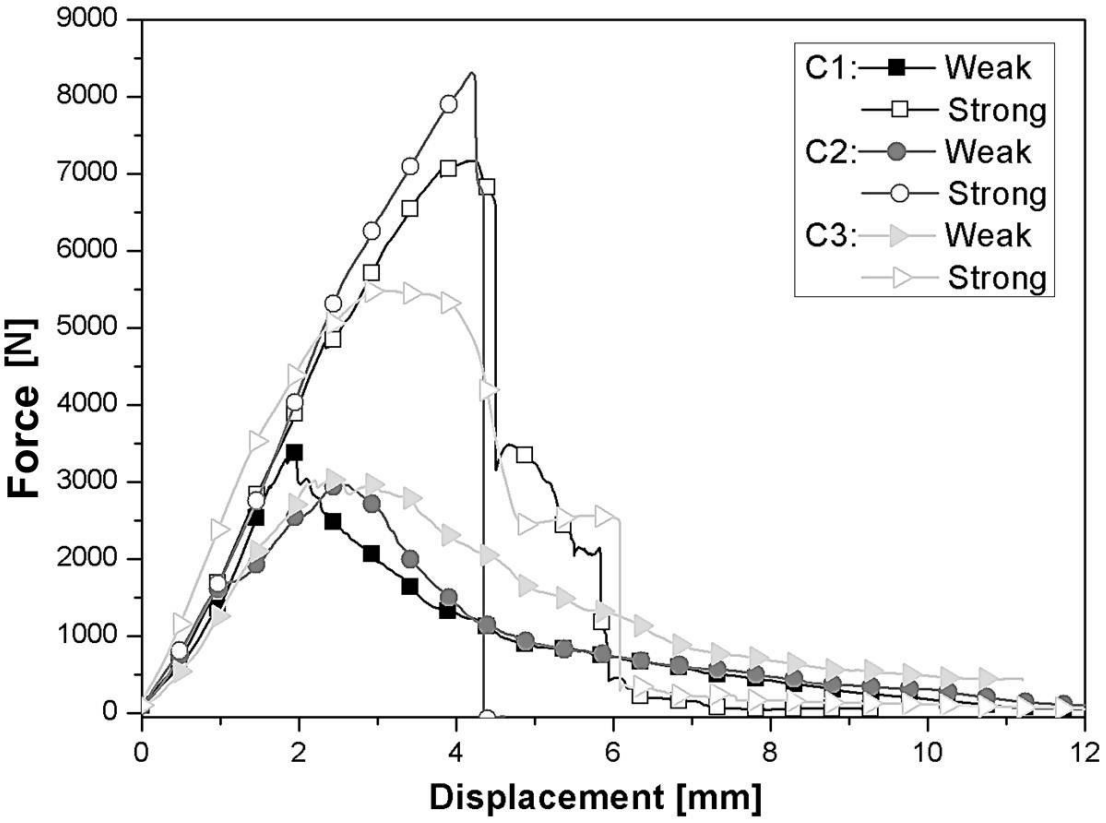

Figure F. 1 Mechanical performance of the Ti-6Al-4V alloy (in tensile testing) and of Ti-6Al-4V/GF-P friction-riveted joints (in lap shear testing), exhibiting the best and worst performance observed for this material combination for each joining condition.

APPENDIX G Semi-Qualitative Chemical Composition of GF-P from the Key Hole through Energy Dispersive Spectroscopy (EDS)

Figures F.G-a and -c show the microstructures of two different areas in Region 3 of the key-hole formed during FricRiveting process and remained from failure Mode 2 (Figures 10.13-f and -g, Section 10.2.2). Figures G.1-b and –d shows semi-quantitative chemical composition of areas of interest marked in Figures G.1-a and –c by yellow circles.

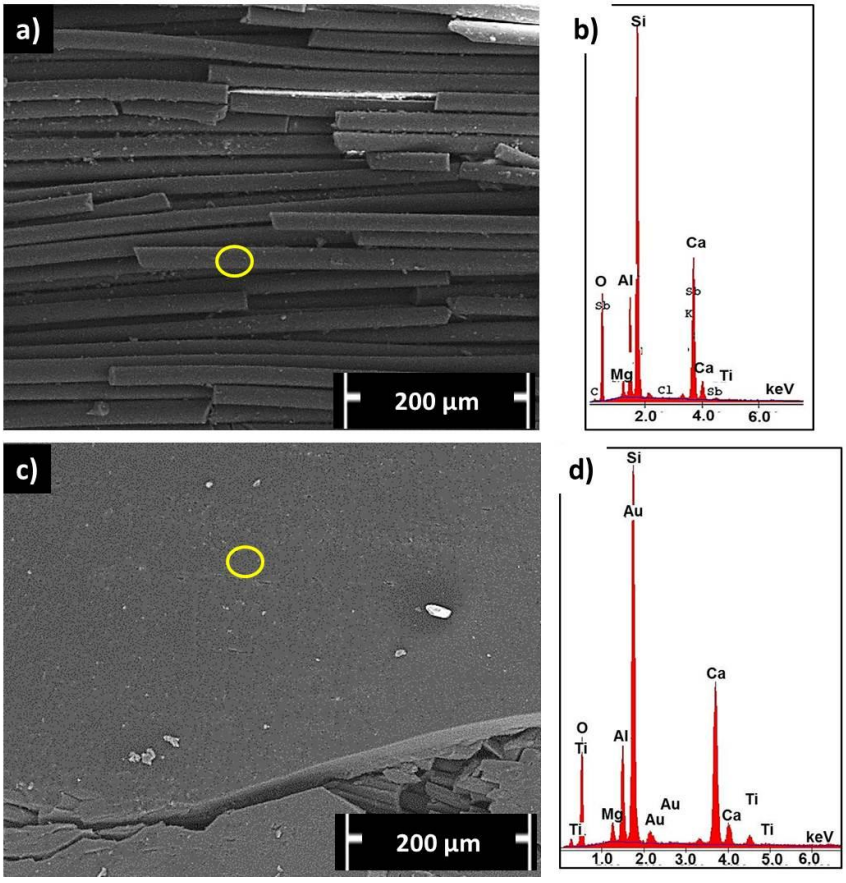

Figure G. 1 a) Microstructure of Region 3-ii (Figure 10.13-f); b) EDS spectrum of the selected area in figure a; c) microstructure of Region 3-iii (Figure 10.13-g); d) EDS spectrum of selected area in figure c.

APPENDIX H Summary of the properties of Ti-6Al-4V/GF-P case-study joints

Table H. 1 Summary of Ti-6Al-4V/GF-P joints investigated in this work.

Joining condition	Replicate	T_p (°C)	M_z (Nm)	E_{fr} (J)	E_{ax} (J)	H (mm)	W (mm)	A (mm^2)	σ_{br} (MPa)	Microstructure*	
										β-Ti phase (%)	**$LABs_{2\text{-}15°}$ (%)**
C1 (RS: 9000rpm, FT: 1.0 s, FOT: 1.2 s)	C1_1	320	2.2	1753	200	8.4	7.0	16.9			
	C1_2	600	1.7	1433	228	7.3	6.5	10.5			
	C1_3	351	1.3	810	226						
	C1_4	591	2.5	1423	226	8.9	6.9	14.7			
	C1_LSS1								139		
	C1_LSS2								143		
	C1_LSS3								74		
	C1_LSS4								101		
	C1_LSS5								61		
C2 (RS: 9000rpm, FT: 1.2 s, FOT: 1.2 s)	C2_1	703	1.3	1391	185	5.9	6.3	9.7		**R_1:1.7**	R_1: 9.2
	C2_2	814	1.6	2017	238	6.1	6.3	10.3		R_2: 3.7	R_2: 15.5
	C2_3	305	1.3	1788	216					R_3: 2.7	R_3: 18.4
	C2_4	343	1.6	743	208						
	C2_5	664	1.8	1641	98	6.7	6.9	8.3			
	C2_LSS1								166		
	C2_LSS2								161		
	C2_LSS3								124		
	C2_LSS4								80		
	C2_LSS5								144		
C3 (RS: 10000rpm, FT: 1.2 s, FOT: 1.2 s)	C3_1	763	1.4	1853	199	6.6	5.4	14.0			
	C3_2	759	1.4	1825	247	6.9	6.9	14.4			
	C3_3	295	1.3	1592	209						
	C3_4	719	2.1	1760	245	7.6	7.3	13.4			
	C3_LSS1								103		
	C3_LSS2								110		
	C3_LSS3								60		
	C3_LSS4								72		
	C3_LSS5								60		

* Microstructure was compared to Ti-6Al-4V base material which has β-Ti phase fraction of 8.7% and LABs of 7.2%

** R- regions in Figure 9.2